TU Delft

MARINE CONTRACTORS

PILING VIBRATIONS MCGF

A numerical assessment of the structural dynamics of a Motion-Compensated Gripper Frame during pile driving of XXL monopiles

E. Kweldam

MCGF vibrations

A numerical assessment of the structural dynamics of a Motion-Compensated Gripper Frame during pile driving of XXL monopiles

by

E. Kweldam

to obtain the degree of Master of Science in Offshore & Dredging Engineering
at the Delft University of Technology,
to be defended publicly on Wednesday November 29, 2023 at 1:00 PM.

Student number:	5184266	
Project duration:	November 21, 2022 – November 29, 2023	
Thesis committee:	Dr. P. C. Meijers,	TU Delft, supervisor
	Prof. dr. A. V. Metrikine,	TU Delft, committee chairman
	Ing. M. Kraan,	Heerema Marine Contractors, supervisor
	Ir. E. Steinebach,	Heerema Marine Contractors, supervisor

TU Delft

Preface

This thesis marks the end of my career as a student. After obtaining my HBO Bachelors degree in Mechanical Engineering, I never anticipated that the choice of pursuing my education at the TU Delft would be not only a challenge intellectually, but also at a socially. This journey has been anything but that easy. As former students told me: graduating is like a rollercoaster. From attending online lectures during the Covid pandemic to participating in the European University Waterpolo Championships and numerous other events, it has been a remarkably eventful period in my life. During this 53-week journey, a lot of support from the committee, as well as friends and family has helped me obtaining my Master of Science. In the end, it was more than worth it.

I would like to express my gratitude to my company supervisors from HMC, Edgar Steinebach and Marcel Kraan, for dedicating a significant amount of time to discussing results and guiding me in the right direction. I have learned a great deal from both of you, theoretically but also the practicality insight on the project.
Continuing with my acknowledgments, I extend my thanks to Prof. Dr. Andrei Metrikine, who served as the chairman within the thesis committee. While we did not engage in regular discussions, each interaction left me amazed by your expertise in structural dynamics and constructive feedback. In moments of being stuck, you identified in only seconds what needed to be done differently, turning my stagnation into progress.
Finally, speaking of moments of being stuck, I want to express my gratitude to Peter Meijers. Thank you so much for your assistance. Every time I visited your office with numerous questions, you patiently took the time to help me, ensuring that I left with the confidence to tackle the remaining challenges of the thesis with ease.

Over the months, I really enjoyed working on my thesis at HMC. The friendly atmosphere helped me to progress a lot during this my time there.

Edwin Kweldam
Delft, November 2023

Abstract

The increase of demand for offshore wind energy resulted in an increase of larger wind turbines. These turbines are often placed on top of a monopile (MP) substructure. The conventional method for installing these MPs uses a jack-up vessel. However, due to the local bathymetry and soil conditions. This method has its drawbacks, such as unavailability due to soil conditions, impracticality in excessively deep waters, or high costs. Heerema Marine Contractors (HMC) aims for the novelty of installing these MPs by using semi-submersible crane vessels (SSCV). Installing the MPs with a floating vessel is an attractive alternative due to its accessibility and speed. To counteract the extra motions of the floating vessel a Motion Compensated Gripper Frame (MCGF) is utilized. This gripper frame uses eight rollerboxes (RBs) equipped with polyurethane (PU) rollers to keep the MP in position, being able to install MPs from 7 up to 12.5 meters in diameter.

During pile driving, vibrations will propagate through the MP, inducing vibrations within the RB. Existing pile driving models fall short in accurately describing the behavior of large diameter MPs. In large diameter MPs the effect of the so called breathing of the MP is discarded as the radial coupling is neglected. In addition, the material properties of the PU rollers are undefined or uncertain.

This thesis investigates the coupling between the MP and RB vibrations by using a numerical model derived with the Finite Difference Method (FDM). Three models were proposed: (1) the MP model, (2) the RB model and (3) the coupled model. Where the latter is coupled by incorporating a spring-dashpot system to simulate the behavior of the linearized PU rollers. The MP is considered behave axisymmetrically, simplifying the 3D wave equations to a 2D system of equations. The resulting motions from these models are directly compared to the motions obtained from a Finite Element Method (FEM) simulation in Abaqus. The MP model, in particular, exhibits good agreement with the Abaqus model. The RB model and coupled model predict higher accelerations than their FEM counterparts, aligning with expectations as the FDM model is computed by the 1D Euler-Lagrange beam equation, directing all stresses and forces directly into bending of the beam.

Analysis of the dynamic stiffness in both the Monopile (MP) and Rollerboxes (RB) reveals that the RB is vulnerable to excessive vibration when the roller stiffness aligns in such a way that the eigenfrequency of the RB intersects with the ring frequency of the MP. This susceptibility is particularly notable in the case of small-diameter MPs (7-7.7m), where the roller stiffness that causes excessive vibrations, is close to the assumed base value of 200 kN/mm. In the category of large diameter MPs, a roller stiffness exceeding 1650 kN/mm could produce a similar effect. As the roller stiffness is a critical parameter for the response of the RB, it is important to know its value during the design phase. To prevent or mitigate excessive vibrations, it is essential to choose a roller stiffness that avoids eigenfrequency intersections between the RB and the MP. This proactive step is vital for optimizing the performance and stability of the MCGF during pile driving operations.

It is crucial to acknowledge that this thesis employs a simplified hammer input force for a 12.5m diameter MP, showcasing predominantly low frequencies. In reality, higher frequencies occur, which could result in more energy density, a significant consideration given that smaller diameter MPs result in higher ring frequencies. For future analyses, determining specific hammer forces corresponding to different diameters is therefore recommended.

Furthermore, the comparison between the industry practice for calculating resulting stresses in the RB and those derived from the numerical model indicates higher stresses in the industry approach. However, it is noteworthy that the predominant contribution to maximum stresses originates from the prestress on the MP, constituting 93% of the total stress. As a consequence, the additional stresses attributed to accelerations are relatively negligible in comparison.

Contents

Nomenclature

List of abbreviations

Abbreviation	Description
1D/2D/3D	One-/Two-/Three-dimensional
BC	Boundary conditions
BDF	Backward difference formula
DM	Donnell-Mushtari
DMA	Dynamic mechanical analysis
EOM	Equations of motion
FDM	Finite difference method
FEM	Finite element method
FFT	Fast fourier transform
HMC	Heerema Marine Contractors
IC	Interface conditions
LHS	Left hand side
MP	Monopile
ODE	Ordinary differential equation
PDE	Partial differential equation
PU	Polyurethane
RB	Rollerbox
RHS	right-hand side
RK	Runge-Kutta
RKDP	Runge-Kutta Dormand-Prince method
RL	Rayleigh-Love
SSCV	Semi submersible crane vessel
WLF	William-Landel-Ferry

Symbols

Symbol	Description	Unit	Value
A_{RB}	Cross sectional area of rollerbox	m^2	
b_{RB}	Width of rollerbox	m	
C	Damping matrix	Ns/m	
c_{RB}	Outer fibre distance from neutral axis	m	
c_0	Unidirectional stress wave speed	ms^{-1}	5172.2
c_C	Damping value of hydraulic cylinder	Nsm^{-1}	
c_p	Longitudinal thin plate wave speed	$m\,s^{-1}$	5421.9
c_R	Damping value of roller	Nsm^{-1}	
D_{out}	Outer diameter monopile	m	
E	Young's modulus	MPa	2.10E+05
$E(t)$	Hammer energy	kgm^2s^{-2}	
f	Frequency	Hz	
F_{hc}	Resulting force in hydraulic cylinder	N	
F_G	Resulting force in gripper ring attachment point	N	
$F_H(t)$	Hammer input force	N	
F_p	Prestress on monopile	N	
f_r	Ring frequency of monopile	Hz	

Symbol	Description	Unit	Value
G	Shear Modulus	MPa	
G', G''	Storage and loss modulus	MPa	
h_{MP}	Monopile wall thickness	m	
h_{RB}	Height of rollerbox	m	
I_{RB}	Second moment of inertia of rollerbox	m^4	
I_p	Polar second moment of inertia	m^4	
K	Stiffness matrix	Nm^{-1}	
K_{dyn}	Dynamic stiffness matrix	Nm^{-1}	
k_C	Spring stiffness hydraulic cylinder	Nm^{-1}	
k_R	Spring stiffness roller	Nm^{-1}	
l_{hc}	Strok of hydraulic cylinder	m	
L_{MP}	length of monopile	m	
L_{RB}	Length of rollerbox	m	
L_{hc}	x-position of hydraulic cylinder	m	
M	Mass matrix	kg	
n	Circumferential mode	-	
$N_z, N_\theta, N_{z\theta}, N_{\theta z}$	Membrane stresses	N	
q_{acc}	Distributed load due to added acceleration	Nm^{-1}	
R	Radius of monopile	m	
T	Temperature	°C	
T_G	Glass temperature	°C	
t	time	s	
$t_{RB,side}, t_{RB,tb}$	RB wall thickness of sides, top and bottom	m	
u	Axial direction of monopile	m	
w	Radial direction of monopile	m	
w_{RB}	Transverse direction of rollerbox	m	
z_c	contact surface roller with monopile	m	
z_{RB}	Position of RB measured from top of the MP	m	
α	Rollerbox angle w.r.t. monopile	°	51-81
α_c	Hydraulic cylinder angle w.r.t rollerbox	°	58-80
β	Dimensionless thickness parameter	-	
γ	Axial wave number	m^{-1}	
$\gamma_{z\theta}$	Shear strain	-	
δ	Phase angle	°	
Δt	Time step	s	
Δt_F	Force time duration	s	
Δx	Mesh size rollerbox	m	7850
Δz	Mesh size monopile	m	
∇	Modified operator	-	
ϵ	Strain of material	m/m	
θ	Polar angle	°	
κ	Polar radius of gyration	m	
κ_{oil}	Oil bulk modulus	MPa	
ν	Poisson ratio	-	
ρ	Material density	kgm^{-3}	0.3
σ	Stress of material	MPa	
σ_b	Bending stress	MPa	
σ_z, σ_θ	Unidirectional stress	MPa	
$\tau_{\theta z}, \tau_{z\theta}$	Shear stresses	MPa	
ϕ	Rate of movement of a molecule	-	
Ψ	Helmoltz free energy	kgm^2s^{-2}	
ω	Frequency	rad s^{-1}	
ω_n	Eigenfrequency mode n	rad s^{-1}	

List of Figures

List of Tables

1

Introduction

1.1. Installation of monopiles

The demand of wind energy is increasing and therefore the demand for larger turbines. The larger the wind turbine, the higher the amount of generated energy due to the larger area of the blades being able to capture more of the available wind (Hutchinson and Zhao, 2023). Larger turbines require bigger and stronger sub-structures such as monopiles (MPs). These MPs are mostly installed by jack-up vessels. However, this method is highly depending on the bathymetry and soil conditions of the project site. Installing these substructures while floating is therefore an attractive alternative due to its accessibility and speed. This is where Heerema Marine Contractors (HMC) is able to step into the market being able to install these large MPs with the use of, for example their semi submersible crane vessel (SSCV) Thialf.

Installing MPs while floating results in the requirement to compensate for the vessel's motions since the MP needs to be kept stationary with regard to its position in the seabed. To counteract these motions, a Motion Compensated Gripper Frame (MCGF) is currently in development, as depicted in Figure 1.1. This gripper frame uses eight polyurethane (PU) rollers to keep the MP in position, being able to install MPs from 7 up to 12.5 meters in diameter. Each of these rollers are integral components of the rollerbox (RB), which employ hydraulic cylinders for individual pretensioning of the MP. Furthermore, the rollers possess the capability to independently exert pressure on the MP, ensuring that it remains within the required vertical misalignment tolerance. When the pile is within the alignment margins, a hydraulic hammer is then used to drive the pile into the soil. The method for installing MPs by means of a hydraulic hammer is called impact pile driving.

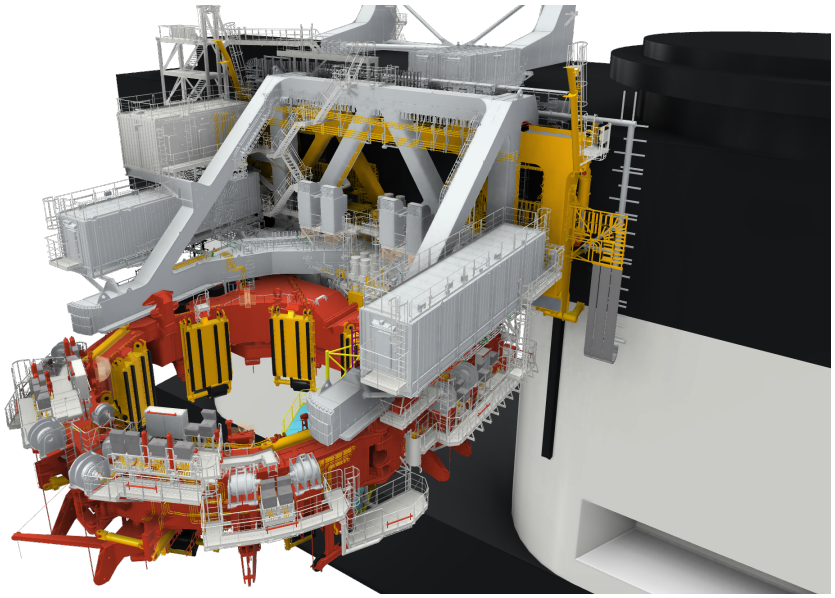

Figure 1.1: Overview Motion Compensated Gripper Frame and its components

1.2. Problem statement

Impact pile driving is currently the main method of installing MPs in the offshore industry. However, this method generates high-frequency stress waves that propagate through the MP, resulting in not only axial but also radial displacements. Given that the MCGF and its rollerboxes hold the MP in place, these deflections directly impact the forces applied to the rollers. Although the rollers mitigate the transfer of axial vibration, the combined effects of prestress and the material characteristics of the rollers may not be entirely negligible for transferring the axial vibrations into the MCGF. Consequently, the influence of vibrations on the rollers and, by extension, the gripper structure remains uncertain. HMC raised the question of whether these vibrations could potentially damage the MCGF structure.

Currently, common pile driving models are based on the one-dimensional (1D) wave equations (Smith, 1962), such as GRLWEAP (Rausche et al., 2004). However, with the trend of increasing diameter MPs, lower natural frequencies in radial direction (ring frequency) are expected. These frequencies may intersect with the range of the frequencies of the hammer impact. 1D models are insufficient to account for this phenomenon, making them unsuitable for addressing such complex scenarios. Therefore, it is imperative to identify an appropriate approach to address the stresses and accelerations in the RB.

1.3. Scope of research

The primary objective of this thesis is to build a model which assesses the stresses and accelerations of the rollerboxes. This is of importance to calculate the stresses in the rollerboxes as well as vibrations exciting the MCGF. Previous research, as documented by (Zwartveld, 2016), has demonstrated that accelerations of up to 300 m/s^2 can occur during pile driving. However, this model is based on a steel-on-steel contact surface which is not representative in case of the MCGF. The PU rollers on the other hand allow for a more smooth impact surface. It is expected that the rollers will transfer lower accelerations due to its relative damping with respect to steel surfaces.

Numerous initial assumptions will be introduced to streamline the modelling. The impacts of these assumptions will be examined in the subsequent chapter, where a comprehensive literature review will be conducted to investigate the influence of these parameters.

Firstly, in this study the MP is assumed to be a constant diameter and wall thickness along its entire length. In practice, the upper portion of the MP features a tapered shape or have a flange on top. Furthermore, the wall thickness is typically non-uniform due to varying loads, primarily bending, experienced at different heights.

Secondly, the rollers are constructed from polyurethane (PU), a material characterized as hyper-viscoelastic and nonlinear (Bergström, 2015). "Hyper-viscoelastic" indicates that the material's mechanical behavior combines elements of both elasticity and viscosity, thus its ability to return to its original shape after deformation and ability to deform continuously over time. This property implies that PU exhibits complex stress and strain responses, particularly when subjected to dynamic loads. The "nonlinear" part represents that the relationship between stress and strain (deformation) in PU is not linear, as it might be in simpler materials like metals or linearly elastic materials. Instead, as stress increases, the material's response becomes increasingly non-proportional, making it more challenging to predict and model compared to linear materials. Due to the complexity associated with this material, this study assumes that the rollers have a linearized behaviour. Further details about the effect of this nonlinear behaviour will be elaborated in the literature review.

Thirdly, it is assumed that the impact of the hammer is evenly distributed over the circumference of the MP, e.g. the non-verticality of the load is not taken into account. This assumption leads to the problem being transformed into an axisymmetric, two-dimensional (2D) scenario rather than a three-dimensional (3D) one.

Fourthly, despite the gripper being positioned above the waterline, it is worth noting that water and soil conditions can significantly influence the magnitude of the propagating wave. However, this study does not consider the effects of water and soil conditions. It assumes that the full energy introduced by the hammer is concentrated in the initial propagating wave of the impact and there is no damping involved by the characteristics of the water and soil. Furthermore, the primary objective of pile driving is to drive the pile into the soil, hence the emphasis on directing the energy into the ground rather than reflecting this energy towards

the upper part of the MP. Depending on the relative positioning of the MCGF with respect to the dimensions of the MP, the time span for simulation of interest should be adjusted accordingly.

The above mentioned assumptions are intended to form the basis of a model that serves as the foundational framework for further investigations into the vibrations affecting the MCGF and its components. Such research is essential to ensure structural integrity and stable positioning of sensors and associated electronic equipment.

1.4. Research question

In this document, the following question can be formulated as the main research question:

"What is the effect of the vibrations on a MCGF caused by driving XXL monopiles?"

To be able to provide an answer to this question, it can be subdivided into several key sub-questions:

1. *What theories can be used to set up a model for showcasing the vibrations in the MP and RB?*
2. *When solving the equation of motions of the system, which parameters have to be taken into account?*
3. *How can one verify the model using various methods such as FEM and/or comparison with measurement data?*
4. *Where should measurements take place in the system, and what could be measured to validate the models?*
5. *Which parameters have the most impact on the vibrations in the system and could these be adjusted such that the vibrations are mitigated?*

1.5. Research methodology

The objective of this thesis is to provide an answer to the research questions. Hence, a mathematical model is proposed that represents the MP and RB as depicted in Figure 1.2. Solving this system requires to set up the equations of motion (EOM) for both the MP and the RB.

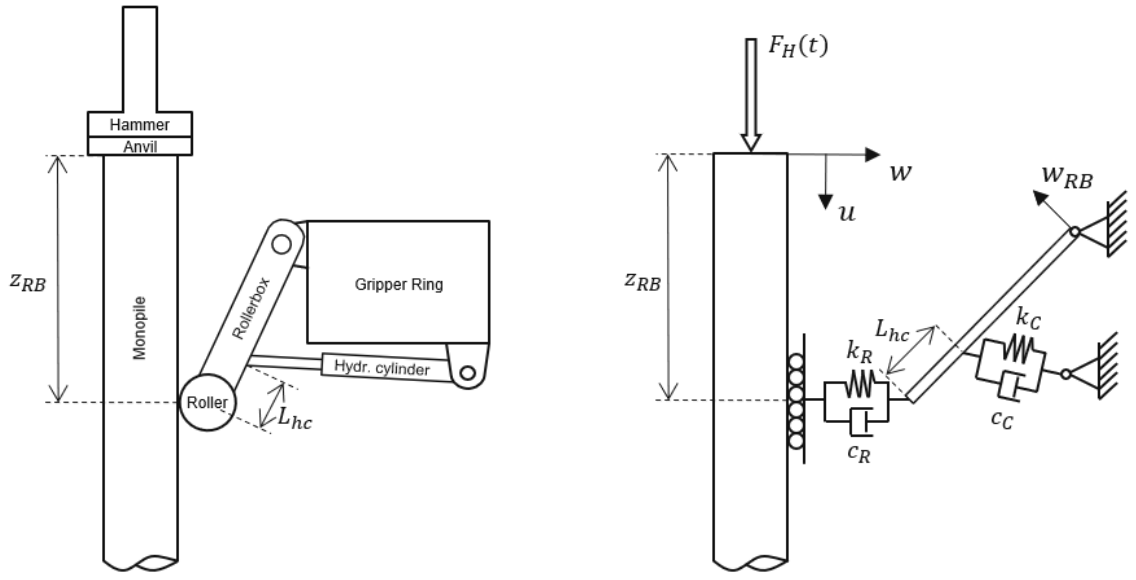

(a) Schematic overview

(b) Mathematical model

Figure 1.2: A cross-sectional depiction of the entire system alongside its mathematical representation

In chapter 2, solvable equations derived from a literature study will be presented. This study employs numerical methods to solve these equations. Furthermore, it explores the impact of roller properties and addresses how to incorporate them into the model, addressing uncertainties associated with these properties.

In chapter 3, the mathematical model is divided into the following sequential, progressively complex stages: (1) The MP model, where a simplified MP is subjected to impact by a hammer. This simulates the pile driving technique on a MP with axisymmetric properties.

(2) The RB model, where the rollerbox is individually modeled using the well-known beam equation to examine the effects of a forced input on a spring at the end of this beam.

(3) In this coupled model, the intention is to establish a correlation between the input (hammer force) and the displacements/accelerations in the RBs. This approach is employed to evaluate possible constraints or difficulties within each model in isolation and to gain insights into how these models mutually interact with one another.

The validity of the models will be confirmed through a Finite Element Method (FEM) simulation. HMC utilizes *Abaqus FEA* as their primary software package, which is therefore used to conduct this study.

Following the validation of the models, the subsequent step involves utilizing these models to conduct a parameter study on vibration mitigation in chapter 4. This study will focus on examining adjustable parameters. Although it may not be feasible to modify specific parameters in the current MCGF for upcoming projects, the findings could be valuable for future projects, offering insights into potential adjustments that could effectively mitigate vibrations. Additionally, the model will be employed to provide guidance on the optimal locations for sensor measurements on the MCGF or MP. This data could be used for validating the accuracy and reliability of the model.

Chapter 5 demonstrates how the current model is utilized for determining the stresses in the RB. The industry practices will be compared with these values to gain insight on the effect of the vibrations to the stresses in the system. In the final chapter, conclusions will be drawn from the entirety of the research. Well-defined recommendations will be provided, where the current assumptions and limitations of this thesis will be discussed. Additionally, advice will be offered for further research based on the findings of this study.

2

Theoretical background

Before the models can be developed to address the research questions at hand, it is essential to elaborate on the underlying theories to gain an understanding of how the model should be formulated, considering the scope discussed in the previous chapter.

Firstly, the equations of motion will be derived for the case of large-diameter MPs. Multiple theories will be examined, including the use of 1D versus 3D theories. It will become evident why, in practice, 1D theories are no longer sufficient due to the increasing dimensions of the MPs over time. With the derived EOMs, two types of solvers will be discussed, each with its advantages and disadvantages.

Following that, the influence of the offshore environment is discussed, where the MP is immersed in water and being driven into the soil. Theories and previous studies will be considered to provide an estimate of the energy losses due to these factors. This information will enable to determine the appropriate simulation time.

Lastly, the material properties of the PU polymer will be explored, including its distinct characteristic behaviors. The material's behavior will be split into its viscoelastic and hyperelastic aspects to better understand their combined effect. An overview of the impact of temperature and time on the material will also be provided, as the PU properties are highly dependent on these factors.

2.1. Pile driving theories

The installation of MPs represents a critical phase in the construction of offshore wind farms (OWF). The installation phase is a significant part of the total costs of the project, estimated at approximately 3.2% (BVG Associates, 2019). Therefore, it is essential to devote close attention to this phase, particularly regarding the pile drivability analysis. Unreliable or inaccurate results of the drivability could result in potential project risks, including time delays. It is important to counter these problems during the engineering phase, which evidently means that the analysis should be as accurate as possible.

2.1.1. Rod equation

To understand the mechanics of vibrations in a pile, it is essential to examine prior pile-driving methodologies. As a starting point, the classical rod equation can be explored. This theory describes the vibrations of the pile in longitudinal direction. To be able to set up the governing equation for this thin rod, basic propagation characteristics are considered. When assuming a rod under a dynamically varying stress, as illustrated in Figure 2.1b, the following equation of motion is applicable:

$$-\sigma A + A\left(\sigma + \frac{\partial \sigma}{\partial z}\,\Delta \mathrm{z}\right) + qA\,\Delta z = \rho A\,\Delta z \frac{\partial^2 u}{\partial t^2} \tag{2.1}$$

in which A is the cross sectional area of the rod, the material density ρ and q an arbitrary body force.

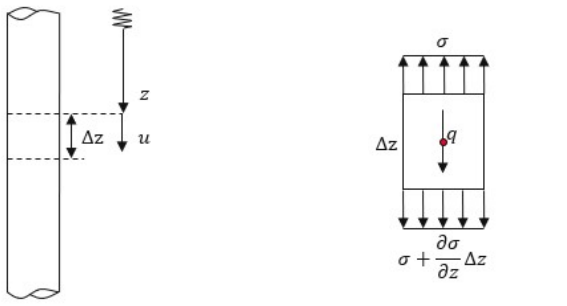

(a) Section of a rod **(b)** Differential element of a rod

Figure 2.1: Illustration of a rod and its differential element (Graff, 1975)

Assuming elastic material behavior allows us to use Hooke's law, stating that the unidirectional stress can be determined by using the strain (ε) of the material:

$$\sigma = E\varepsilon = E\frac{\partial u}{\partial z} \tag{2.2}$$

Simplifying Equation 2.1 and using Equation 2.2, results in the well-known rod equation:

$$\frac{1}{c_0^2}\frac{\partial^2 u}{\partial t^2} = \frac{\partial^2 u}{\partial z^2} \tag{2.3}$$

in which c_0, calculated by $c_0 = \sqrt{E/\rho}$, is the unidirectional stress wave speeds in the material ranging from 4850-5200 m/s, determined by the Youngs Modulus E and the material density ρ. u represents the displacement in longitudinal direction and z the position along the pile.

In this study a length of 110 m is assumed for the base case. Given the wave speeds, it is anticipated that a reflected wave is expected within the time frame of 42.3-45.4 milliseconds at the top of the MP. As mentioned in section 1.3, the absence of soil and water in the model leads to an overestimation of vibrations, as these environmental factors typically provide damping effects. In addition, it is assumed in this study that the bottom of the MP is clamped, resulting in the complete reflection of the propagating wave at this boundary. It is essential to recognize that this assumption also leads to an overestimation of the real-world scenario.

This leads us to a crucial aspect of this study: the simulation time. The duration of the simulation has significant implications for computational efficiency. Considering the previously mentioned factors related to the overestimation of vibrations, it can be argued that, in principle, only the initial wave is relevant to this research. Although these initial vibrations contain the majority of the energy, this study incorporates a parameter study to investigate how different parameters affect the behavior and magnitude of vibrations. Now, with the estimated time of the reflected wave it is can be said that without reflected waves, the simulation time should be larger than 4 ms and smaller than 40 ms when examining the data at the height of 20m where the MCGF is positioned. However, given the research objective to examine the effects of the MCGF on vibrations, a longer simulation time is warranted. To adequately capture these effects, it is assumed that a simulation time of 100 ms (or 0.1 s) is sufficient, having two reflections in the results.

2.1.2. Other 1D methodologies

The rod equation is the simplest form of characterizing the behavior of the vibrations. Smith (1962) developed a pile driving method based on lumped masses and springs allowing to solve the discretized 1D wave equation for different layers of soil and their resistance to the hammer input. This numerical model incorporates nonlinear springs and dashpots to the system representing the soil behavior, which makes this model suitable for pile-driving applications. This model has gained extensive use due to its simplicity which results in shorter simulation times. It serves as the foundational framework for the GRLWEAP model, which continues to be employed in practical applications (Rausche et al., 2004).

The aforementioned pile driving methods neglect the lateral vibrations. In the Rayleigh-Love (RL) rod theory the lateral strains are taken into account based on Hooke's law (Graff, 1975). The longitudinal strains are in

reality also affected by the lateral strains by the Poisson's ratio (v) . In case of steel, a value of $\nu \approx 0.3$ can be assumed. In contrast with the unidirectional Hooke's law, it can now be described as:

$$\sigma = E\frac{\partial u}{\partial z} + \rho\nu^2\kappa^2\frac{\partial^3 u}{\partial z \partial t^2} \tag{2.4}$$

in which the second term represents the lateral inertia where κ is the polar radius of gyration of the cross section of the rod about its axis, calculated by $\kappa = \sqrt{I_p / A}$. I_p represents the polar second moment of area of the cross section. Substituting this equation in Equation 2.1 results in the EOM for the RL:

$$\frac{\partial^2 u}{\partial t^2} = c_0^2\frac{\partial^2 u}{\partial z^2} + \nu^2\kappa^2\frac{\partial^2}{\partial t^2}\left(\frac{\partial^2 u}{\partial z^2}\right) \tag{2.5}$$

Previous research has shown that the lateral 1D wave equation does not suffice to describe the behaviour in radial direction (Zwartveld, 2016). The interaction between the axial and radial vibrations should be taken into account.

2.1.3. Cylindrical shell theory

In order to capture the effect of lateral and longitudinal vibrations, the governing equations of a shell will be determined in this section. A similar methodology as for the rod equation can be applied to derive the EOMs for the cylindrical shell.

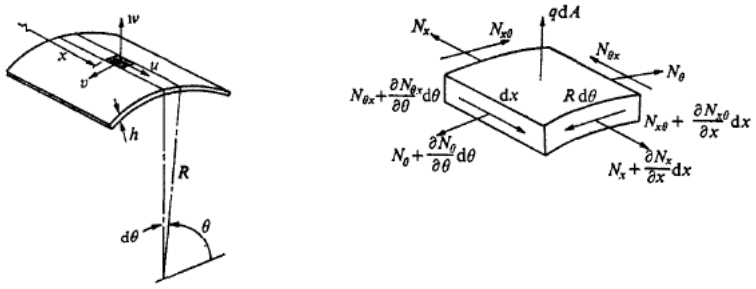

(a) Section of a cylindrical membrane shell

(b) Differential element of a cylindrical shell

Figure 2.2: Illustration of a cylindrical shell and its differential element (Graff, 1975)

Note that the displacement components in axial (u), tangential (v) and radial (w) are described in terms of the cylindrical geometry with z again being in longitudinal direction along the shell and θ being the polar angle. In the figure above, the z direction is denoted as x as the coordinate system is defined differently in the book of Graff (1975). In this case, no bending moments are present, nor are the transverse shear forces, as only membrane actions are considered for the differential element. The EOM in the axial, tangential and radial direction are, respectively:

$$\rho h\frac{\partial^2 u}{\partial t^2} = \frac{\partial N_z}{\partial z} + \frac{1}{R}\frac{\partial N_{\theta z}}{\partial \theta} \tag{2.6a}$$

$$\rho h\frac{\partial^2 v}{\partial t^2} = \frac{1}{R}\frac{\partial N_\theta}{\partial \theta} + \frac{\partial N_{z\theta}}{\partial z} \tag{2.6b}$$

$$\rho h\frac{\partial^2 w}{\partial t^2} = -\frac{1}{R}N_\theta \tag{2.6c}$$

in which R is the radius of the pile and $N_z, N_\theta, N_{z\theta}, N_{\theta z}$ are the membrane stresses. These stresses can be obtained by taking the integral of the usual stresses across the shell thickness (h), which is formulated by:

$$N_z, N_\theta, N_{z\theta}, N_{\theta z} = \int_{-h/2}^{h/2} (\sigma_z, \sigma_z, \tau_{z\theta}, \tau_{\theta z})\, dz \tag{2.7}$$

Now, using Hooke's law again the following expressions can be formulated for the stresses and shear:

$$\sigma_z = \frac{E}{1-\nu^2}\left(\varepsilon_z + \nu\varepsilon_\theta\right) \tag{2.8a}$$

$$\sigma_\theta = \frac{E}{1-\nu^2}\left(\varepsilon_\theta + \nu\varepsilon_z\right) \tag{2.8b}$$

$$\tau_{z\theta} = \tau_{\theta z} = \gamma_{z\theta} G \tag{2.8c}$$

in which $\gamma_{z\theta}$ and G are the shear strain and shear modulus respectively. The integrals from Equation 2.7 result in the following expressions for the membrane stresses:

$$N_z = \frac{Eh}{1-\nu^2}\left(\frac{\partial u}{\partial z} + \frac{\nu}{R}\left(w + \frac{\partial v}{\partial \theta}\right)\right) \tag{2.9a}$$

$$N_\theta = \frac{Eh}{1-\nu^2}\left(\frac{w}{R} + \frac{1}{R}\frac{\partial v}{\partial \theta} + \nu\frac{\partial u}{\partial z}\right) \tag{2.9b}$$

$$N_{z\theta} = N_{\theta z} = \frac{Eh}{2\left(1+\nu\right)}\left(\frac{\partial v}{\partial z} + \frac{1}{R}\frac{\partial u}{\partial \theta}\right) \tag{2.9c}$$

Substituting the membrane stresses into the EOM in their generic form as described in Equation 2.6 reads:

$$\frac{1}{c_p^2}\frac{\partial^2 u}{\partial t^2} = \frac{\partial^2 u}{\partial z^2} + \frac{\nu}{R}\frac{\partial w}{\partial z} + \frac{\partial^2 v}{\partial z \partial \theta} + \frac{(1-\nu)}{2R}\frac{\partial^2 v}{\partial z \partial \theta} + \frac{(1-\nu)}{2R^2}\frac{\partial^2 u}{\partial \theta^2} \tag{2.10a}$$

$$\frac{1}{c_p^2}\frac{\partial^2 v}{\partial t^2} = \frac{1}{R^2}\frac{\partial w}{\partial \theta} + \frac{1}{R^2}\frac{\partial^2 v}{\partial \theta^2} + \frac{1}{R}\frac{\partial^2 u}{\partial z \partial \theta} + \frac{(1-\nu)}{2}\frac{\partial^2 v}{\partial z^2} + \frac{(1-\nu)}{2R}\frac{\partial^2 u}{\partial z \partial \theta} \tag{2.10b}$$

$$\frac{1}{c_p^2}\frac{\partial^2 w}{\partial t^2} = -\frac{1}{R}\frac{w}{R} - \frac{1}{R^2}\frac{\partial v}{\partial \theta} - \frac{\nu}{R}\frac{\partial u}{\partial z} \tag{2.10c}$$

here, c_p denotes the longitudinal thin plate wave speed in the material, which is calculated by $c_p = \sqrt{\frac{E}{\rho(1-\nu^2)}}$. It is worth mentioning that this is similar to the wave speed in the rod equation, albeit the wave speed in axial direction for a cylindrical shell is 4.8% ($\approx 1/(1-\nu^2)$) higher for steel.

The EOMs can also be written in operator form, presented by Leissa (1973):

$$\left[\mathscr{L}_{DM} + \beta\mathscr{L}_{mod}\right]\begin{bmatrix} u \\ v \\ w \end{bmatrix} = 0 \tag{2.11}$$

where $\beta = h^2/(12R^2)$ is a dimensionless thickness parameter. Large diameter MPs can consist of wall thicknesses ranging from 40-150 mm or even higher. This would results in a range of β = 3.4e-06 to 1.5e-04, suggesting that the impact of this so-called modified operator can be effectively disregarded. However, the Donnell-Mushtari (DM) shell theory implies that ∇^4 should be added in the EOM for the radial direction (w) in Equation 2.10c. Flügge (1960) states that this term is to account for the effect of the rather rapidly change of shear in radial and axial direction. The modified operator reads:

$$\nabla^4 = R^4\frac{\partial^4}{\partial z^4} + R^2\frac{\partial^4}{\partial z^2 \partial \theta^2} + \frac{\partial^4}{\partial \theta^4} \tag{2.12}$$

Now, the complete system in matrix form can be defined as:

$$\frac{1}{c_p^2}\frac{\partial^2}{\partial t^2}\begin{bmatrix} u \\ v \\ w \end{bmatrix} = \begin{bmatrix} \frac{\partial^2}{\partial z^2} + \frac{(1-\nu)}{2R^2}\frac{\partial^2}{\partial \theta^2} & \frac{\partial^2}{\partial z \partial \theta} + \frac{(1-\nu)}{2R}\frac{\partial^2}{\partial z \partial \theta} & \frac{\nu}{R}\frac{\partial}{\partial z} \\ \frac{1}{R}\frac{\partial^2 u}{\partial z \partial \theta} + + \frac{(1-\nu)}{2R}\frac{\partial^2}{\partial z \partial \theta} & \frac{1}{R^2}\frac{\partial^2}{\partial \theta^2} + \frac{(1-\nu)}{2}\frac{\partial^2}{\partial z^2} & \frac{1}{R^2}\frac{\partial}{\partial \theta} \\ -\frac{\nu}{R}\frac{\partial}{\partial z} & -\frac{1}{R^2}\frac{\partial}{\partial \theta} & -\frac{1}{R^2} - \frac{h^2}{12}\frac{\partial^4 w}{\partial z^4} - \frac{h^2}{12R^2}\frac{\partial^4 w}{\partial z^2 \partial \theta^2} - \frac{h^2}{12R^4}\frac{\partial^4 w}{\partial \theta^4} \end{bmatrix}\begin{bmatrix} u \\ v \\ w \end{bmatrix} \tag{2.13}$$

This matrix summarizes the vibrations in 3D. In the current state of the EOMs it is assumed that distinct vibrations can be anticipated in the tangential direction. However, based on the assumptions outlined in section 1.3, which relate to the neglected non-verticality of the hammer impact and the symmetry of the MP, it can be considered that the entire system can be treated as an axisymmetric system. This implies that $\frac{\partial}{\partial\theta} = 0$, which significantly simplifies the EOMs containing the following terms:

$$\frac{1}{c_p^2}\frac{\partial^2}{\partial t^2}\begin{bmatrix} u \\ v \\ w \end{bmatrix} = \begin{bmatrix} \frac{\partial^2}{\partial z^2} & 0 & \frac{\nu}{R}\frac{\partial}{\partial z} \\ 0 & \frac{(1-\nu)}{2}\frac{\partial^2}{\partial z^2} & 0 \\ -\frac{\nu}{R}\frac{\partial}{\partial z} & 0 & -\frac{1}{R^2} - \frac{h^2}{12}\frac{\partial^4 w}{\partial z^4} \end{bmatrix}\begin{bmatrix} u \\ v \\ w \end{bmatrix} \tag{2.14}$$

Note that the tangential EOM is now entirely independent and not linked to the axial and radial components. This results in the final equations which are to be solved in this thesis for the MP:

$$\frac{\partial^2 u}{\partial t^2} = c_p^2\frac{\partial^2 u}{\partial z^2} + \frac{\nu c_p^2}{R}\frac{\partial w}{\partial z} \tag{2.15a}$$

$$\frac{\partial^2 w}{\partial t^2} = -\frac{c_p^2}{R^2}w - \frac{\nu c_p^2}{R}\frac{\partial u}{\partial z} - \frac{h_{MP}^2 c_p^2}{12}\frac{\partial^4 w}{\partial z^4} \tag{2.15b}$$

2.1.4. Wave dispersion characteristics

The propagation of harmonic waves in axisymmetric conditions are now described by means of the DM theory. In order to study the wave propagation in thin-walled cylinders, the following generic solution could be assumed:

$$u = A\cos(n\theta)e^{i\omega t - i\gamma z} \tag{2.16a}$$

$$w = B\cos(n\theta)e^{i\omega t - i\gamma z} \tag{2.16b}$$

in which n is the circumferential mode, γ is the axial wave number and A, B are constants. In order to get a better understanding of the wave dispersion, it is necessary to get the dispersion equation. To get this equation, the generic solution is to be substituted in the EOM given in Equation 2.15 to eliminate the partial derivatives. To explain the wave dispersion, it is assumed that the circumferential mode $n = 0$, simplifying the equation to:

$$-\omega^2 A = -c_p^2\gamma^2 A - \frac{\nu c_p^2}{R} i\gamma\, B \tag{2.17a}$$

$$-\omega^2 B = -\frac{c_p^2}{R^2}B + \frac{\nu c_p^2}{R} i\gamma A - \frac{h_{MP}^2 c_p^2}{12}\gamma^4 B \tag{2.17b}$$

Note that both equations contain an imaginary part. For the wave dispersion, imaginary parts can be set to zero. Combining and rewriting these equation results in the wave dispersion equation:

$$\frac{h_{MP}^2 c_p^4}{12}\gamma^6 - \frac{h_{MP}^2 c_p^2}{12}\omega^2\gamma^4 + \left(c_p^4 - c_p^2\omega^2\right)\gamma^2 + \left(\omega^4 - \frac{c_p^2}{R^2}\omega^2\right) = 0 \tag{2.18}$$

In Figure 2.3 the wave dispersion is shown of the cylindrical shell for different values of the dimensionless thickness parameter β. It can be seen from this graph that waves at approximately the ring frequency do not have the ability to propagate in the material. In the studies by Meijers (2021) and Tsetas (2023) the wave dispersion is derived similarly, where additional conclusions can be made:

- ➢ In the vicinity of the ring frequency, the phase wave asymptotically approaches the thin plate theory for high frequencies (ω) and high wave numbers (λ). The radial motion is the dominating factor.

- ➢ The effect of the added bending term can be seen in the figures below. When the value of β increases, the influence of this term increases. In the study by Meijers (2021) it is showed that when the bending term is discarded in the EOM in Equation 2.15b, which then becomes the membrane theory, exhibits behavior that resembles the RL rod theory given in Equation 2.5.
- ➢ The cylindrical shell equations may be considered as an excellent theory to describe the axisymmetric wave propagation for thin walled cylinders.

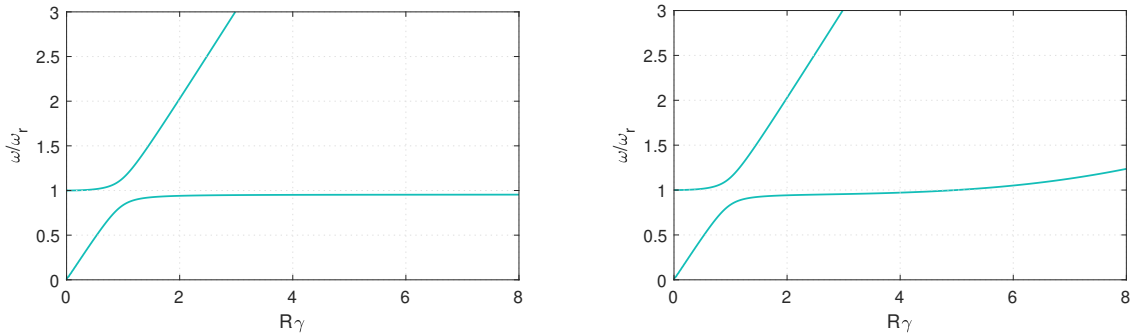

(a) β = 2.13e-07 **(b)** β = 1.51e-04

Figure 2.3: Normalized wave dispersion effect for an axisymmetric cylindrical shell at different values of beta

2.2. Solving the axisymmetric equations

In this section multiple solvers will be discussed to solve the EOM given in Equation 2.14. Solving these equations by means of an analytical solution is rather complicated due to its time (2^{nd} order) and space (4^{th} order) dependency. Therefore, a numerical approach will be taken in this research.

For this study, MATLAB is employed, which includes its own integrated numerical ordinary differential equation (ODE) solvers (Shampine et al., 1997). However, the current EOMs, as depicted in Equation 2.15, are partial differential equations (PDE). In order to use the solvers in MATLAB, it is necessary to transform the PDEs into ODE form. This transformation can be achieved by discretizing the EOMs using the finite difference method (FDM).

In general, two types of solvers can be distinguished: (1) implicit and (2) explicit solvers. In short, the implicit numerical methods are approximation methods where future values of a function are calculated based on an implicit relationship between current and future values. Implicit methods can, in some cases, be stable for larger time steps compared to explicit methods at the cost of an increased computation time. Whereas implicit calculates future values, explicit numerical methods are based on calculating the current values and their derivatives. These methods are generally easier to implement, but may be limited in terms of stability and accuracy, especially when solving stiff differential equations.

The stiffness of a system is more of a phenomenon than a mathematically definable property. Stiff systems have the characteristic where if too large time steps are used, numerical instability starts to play a role, which results in inaccurate data. A defining feature of stiff equations is that explicit methods are insufficient for solving these systems (Hairer and Wanner, 1996). In the book of Vuik et al. (2023) it is stated that a system can be considered stiff when at least one of the following criteria is satisfied:

- ➢ In the set of eigenvalues, some exhibit highly negative real parts, while others have real parts very close to zero;
- ➢ The particular solution experiences significantly slower variations compared to the homogeneous solution.

A requirement for these criteria is that the systems are in the form $\mathbf{y}' = \mathbf{A}\mathbf{y} + \mathbf{f}$, where the solution is the sum of the particular and homogeneous solution.

Considering the computational time and the potential restricted capabilities of explicit methods, this research will evaluate two different solvers: the Backward difference approximation (BDF) and the Runge-Kutta (RK) method, respectively referred to as the stiff "ode15s" solver and the non-stiff "ode45" solver in MATLAB.

2.2.1. Runge-Kutta (ode45)

As mentioned, the RK method is considered in this study. MATLAB's most commonly used ODE solver, ode45, is in most cases a suitable method. The 45 represents that the solver uses a combination of the 4^{th} and 5^{th} of the RK family and is also known as the Dormand-Prince method (RKDP). This RK method takes the weighted average of 6 increments using an adaptive time step, hence being an explicit method. The future value and its truncation error can be determined by:

$$y(x+h) = y(x) + \sum_{K=1}^{6} CH(K) \cdot k_K \tag{2.19}$$

$$\epsilon_0(x+h) = \sum_{K=1}^{6} (CH(K) - CT(K)) \cdot k_K \tag{2.20}$$

in which h is the step size and the constant values of $CH(K), CT(K)$ are given in Table 2.1 (Shampine, 1986). The values of k_K are determined based on the following equations:

$$\begin{aligned}
k_1 &= hf(x + A(1)\cdot\ h,\ y)\\
k_2 &= hf(x + A(2)\cdot\ h,\ y + B(2,1)\cdot\ k_1)\\
k_3 &= hf(x + A(3)\cdot\ h,\ y + B(3,1)\cdot\ k_1 + B(3,2)\cdot\ k_2)\\
k_4 &= hf(x + A(4)\cdot\ h,\ y + B(4,1)\cdot\ k_1 + B(4,2)\cdot\ k_2 + B(4,3)\cdot\ k_3)\\
k_5 &= hf(x + A(5)\cdot\ h,\ y + B(5,1)\cdot\ k_1 + B(5,2)\cdot\ k_2 + B(5,3)\cdot\ k_3 + B(5,4)\cdot\ k_4)\\
k_6 &= hf(x + A(6)\cdot\ h,\ y + B(6,1)\cdot\ k_1 + B(6,2)\cdot\ k_2 + B(6,3)\cdot\ k_3 + B(6,4)\cdot\ k_4 + B(6,5)\cdot\ k_5)
\end{aligned} \tag{2.21}$$

These formulations represents the six iteration points that determine the value of the next node of the system. The truncation error of this fifth order method is therefore of order $\mathcal{O}(h^5)$. During each integration, the step size is adjusted when the truncation error is larger than the user-specified allowed error ($\epsilon < \epsilon_0$). In contrast, when $\epsilon \geq \epsilon_0$ the step size is increased in order to reduce the computational time.

K	A(K)	C(K)	CH(K)	CT(K)	B(K,L)				
					L=1	L=2	L=3	L=4	L=5
1	0	25/216	16/135	-1/360					
2	1/4	0	0	0	1/4				
3	3/8	1408/2565	6656/12825	128/4275	3/32	9/32			
4	12/13	2197/4104	28561/56430	2197/75240	1932/2197	-7200/2197	7296/2197		
5	1	-1/5	-9/50	-1/50	439/216	-8	3680/513	-845/4104	
6	1/2		2/55	-2/55	-8/27	2	-3544/2565	1859/4104	-11/40

Table 2.1: RK45 coefficients by Hairer and Wanner (2000)

2.2.2. Backward difference formula (ode15s)

The BDF methods is a family of implicit solvers that is able to solve stiff problems due to its unconditionally stability property. Within this family, higher-order methods deliver increased accuracy. However, in this study, only the second-order method will be employed, primarily due to its stability characteristics. The first order BDF method is also known as Backward Euler method. Now, determining the value for the future value by means of the BDF2 method can be described by:

$$3y(x+2h) - 4y(x+h) + y(x) = 2h \cdot f(t+2h, y+2h) \tag{2.22}$$

In Figure 2.4 the stability regions of both methods are depicted. The white regions in these graphs represent where the system remains stable for the given eigenvalues of the system. It is evident that the stability region of the explicit RKDP method is limited, while on the other hand, the implicit BDF2 method, demonstrates full stability for all negative real values, regardless of the imaginary part (Süli and Mayers, 2003). This type of stability where the left hand side (LHS) is fully stable, is called an A-stable method. In terms of BDF methods, only the first and second order of the family exhibit A-stable conditions. When the BDF2 system turns out to be unstable, the time step Δt should be increased as $\lambda \Delta t$ will fail to reach stable conditions (Vuik et al., 2023). The truncation error for this method is of order $\mathcal{O}(h^2)$.

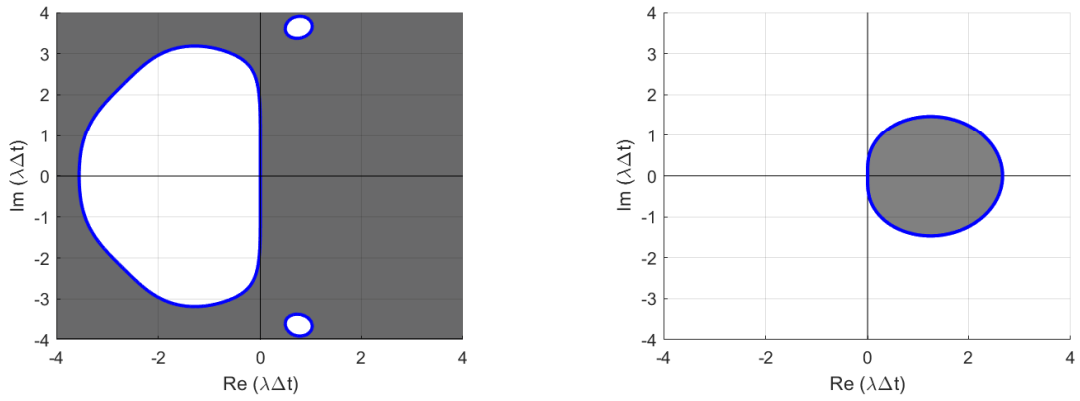

(a) Stability regions RKDP

(b) BDF2

Figure 2.4: Stability regions of the numerical methods with the white areas representing a stable conditions of the system

In the study performed by Celaya et al. (2014), it is demonstrated that an adaptive version of the BDF2 method yields more precise results for solving stiff equations. However, this is more complex to implement and, albeit faster than the regular BDF2 method, is not recommended for use in this study.

2.3. Influence soil and water environment

It is commonly know that impact pile driving comes with loud sounds due to the extreme vibrations. These vibrations can reach up to the range of order 220 dB re 1 µPa (underwater dB) that they significantly impact marine life, cause permanent damage or even cause fatal situations (Reyff, 2012). In practice, various mitigation techniques are employed, such as the use of bubble curtains or modified hammers designed to produce a lower-impact frequency spectrum. The details of the hammer impact will be explored further in this thesis. The model described in this thesis does not include environmental conditions, e.g. influences of soil and water to the vibrations. In this section, a general understanding of the influences will be given regarding the resulting phenomena.

2.3.1. Closed or open ended piles

In the paper of Marsick et al. (2021) an infinitely long cylinder is described which is being submerged horizontally in the water. In this paper, the Donnell-Mushtari shell theory is employed, where the right-hand side (RHS) of the equation is modified by incorporating the water pressure (p) to the radial EOM:

$$\frac{\partial^2 w}{\partial t^2} + \frac{c_p^2}{R^2} w + \frac{\nu c_p^2}{R} \frac{\partial u}{\partial z} + \frac{h_{MP}^2 c_p^2}{12} \frac{\partial^4 w}{\partial z^4} = p_{int}(z) - p_{ext}(z) \tag{2.23}$$

While this method is primarily based on the behavior of a horizontally submerged cylinder, it can be inferred that similar effects may occur for a vertically submerged cylinder. Specifically, the external hydrostatic water pressure could increase the hoop membrane stress, potentially resulting in a reduction of the structural response frequency. However, it should be noted that when a pile is lowered into the water, the pile fills up with water, thereby eliminating any pressure difference between the exterior and interior of the pile. Consequently, this effect can be disregarded when dealing with open piles or piles where air is able to escape when being lowered in general.

2.3.2. Sound radiation

The influence of the soil can be divided into two nonlinear mechanisms: (1) frictional force along the pile shaft and (2) the pile tip resistance. Both of these mechanisms must be overcome to ensure that the pile is effectively driven into the ground and to prevent a phenomenon known as "pile refusal", where the pile does not penetrate the ground and the energy is fully reflected towards the top of the pile.

In Tsouvalas and Metrikine (2014), a 3D vibroacoustic model, as depicted in Figure 2.5, is developed to predict underwater noise generated during pile driving. This model is also based on the equations for thin circular

cylindrical shells. However, to account for the effects of shear deformation and rotational inertia, modifications are made to the shell equations. This modified inertia matrix is detailed in the book of Kaplunov et al. (1998).

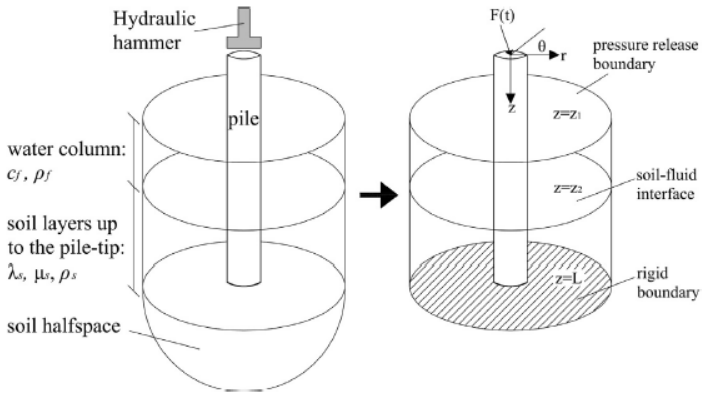

Figure 2.5: Overview of geometry pile in soil and water conditions (Tsouvalas and Metrikine, 2014)

In this model, the springs and dashpots, representing the soil dynamic stiffness can be described by the operator $\mathbf{K}_s$. The soil is assumed to be uncoupled in all directions, resulting in the following operator:

$$\mathbf{K}_s = \begin{bmatrix} k_z + c_z \frac{\partial}{\partial t} & 0 & 0 \\ 0 & k_\theta + c_\theta \frac{\partial}{\partial t} & 0 \\ 0 & 0 & k_r + c_r \frac{\partial}{\partial t} \end{bmatrix} \tag{2.24}$$

in which k_z, k_θ, k_r and c_z, c_θ, c_r are the soil stiffness and damping values, respectively.

In this study, a relatively small diameter with respect to this thesis is used of ($R = 0.46$). However, this study concludes that 80-90% of the input energy percent of the initial energy irradiates into the soil region in the form of shear, compressional and Scholte waves. 1-2% of the input energy is transformed in the form of water pressure waves.

Additionally, in a study done by Tsetas (2023), the influence of the pile radius and the embedment depth to the displacement of the pile tip is considered. The latter is of small influence whereas the pile radius shows a larger influence. However, this study only considers the axial displacement, disregarding the soil reaction in radial direction.

2.4. Polyurethane rollers

PU is a versatile, rubber-like, class of polymer and is widely used in various applications due to its unique combination of properties. It is commonly used in applications where vibrations and structural stability are present. This includes the use of polyurethane rollers in the MCGF to keep the MP in position or to provide as shock absorbers for the vibrations in the system. PU is normally graded by means of their hardness. The higher the grade, the harder the material, meaning that the material has a higher resistance to higher localized deformation. Some of these unique properties are:

Excellent Wear Resistance: PU can withstand wear and abrasion effectively, ensuring longevity in applications that involve frequent friction;

Highly Resilient: Even in harder grades, PU retains a remarkable degree of resilience, making it suitable for shock-absorbing and damping applications;

Resistance to Environmental Factors: PU shows resistance against a range of environmental factors, including mineral oils, fuels, greases, and various solvents, adding to its durability and reliability in diverse conditions.

These unique properties make PU a viable option in engineering and industrial applications where robustness, vibration control, and resistance to extreme environmental conditions are essential.

2.4.1. Linear viscoelasticity

As the description of the material states the PU is a nonlinear hyper-viscoelastic material. In order to describe the effect of such material, a deeper understanding is necessary. In this section the linear viscoelastic property will be discussed. A material can be considered viscoelastic for small deformations. The hardness of the rollers of the MCGF are of class Shore 93 A. This indicates that the Young's Modulus (E) of the material is approximately 20-23 MPa (Gent and Scott, 2012). In the polymer industry, the shear modulus (G) is often used instead of the Young's Modulus. Due to the property of polymers, having a Poisson's ratio of $\nu \approx 0.5$ (Brinson and Brinson, 2015), the shear modulus can be denoted as:

$$G = \frac{E}{2(1+\nu)} \approx \frac{E}{3} \tag{2.25}$$

First, the viscoelastic property of the material indicates that the material is not fully elastic. Linear elastic solids can be defined by using Hooke's law, thus the strain is proportional to the strain. For viscous liquids, Newton's law is valid where the stress is proportional to the rate of change of the strain in time. These laws can be described by, respectively:

$$F = kx \tag{2.26a}$$

$$F = c\frac{\partial x}{\partial t} \tag{2.26b}$$

It is to be noted that these equations represent a simple spring and dashpot force equilibrium and are used in Equation 2.24 in the previous section when adding the linear soil mechanics to the model.

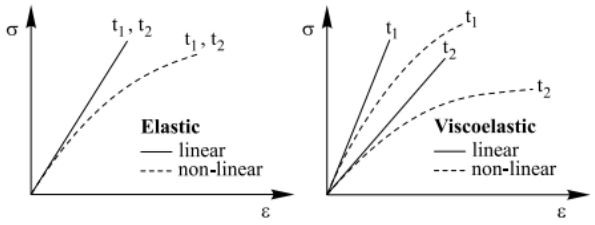

Figure 2.6: An example of an elastic and viscoelastic material, both linear and nonlinear for different values in time (Brinson and Brinson, 2015)

A straightforward way of describing the linear viscoelastic behavior is by using Maxwell and Voight elements where a spring and dashpot are in series and in parallel, respectively. An example of these elements is given in the figure below. When dealing with a nonlinear element a combination of the Maxwell and Voight model, such as the four parameter model, is often used.

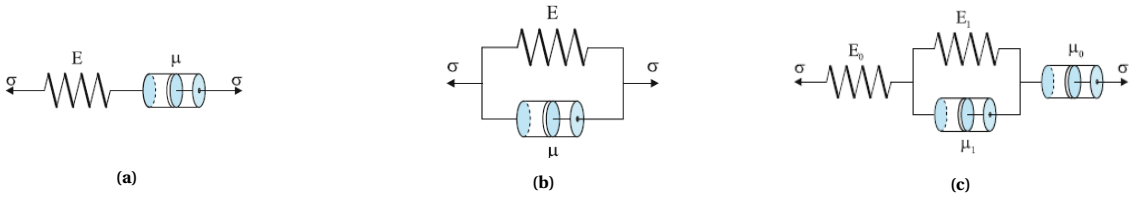

Figure 2.7: A representation of the (a) Maxwell, (b) Voight and (c) a four parameter model

Two common phenomena associated with viscoelasticity are creep and stress relaxation. Creep is the gradual deformation that occurs when a constant force is applied over time, while stress relaxation is the gradual decrease in stress when a constant deformation is maintained over time.

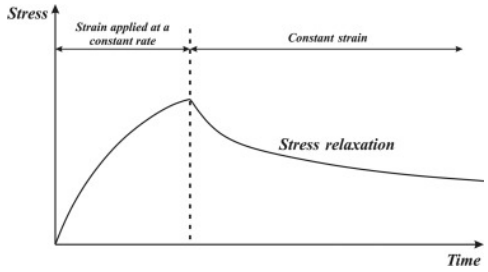

Figure 2.8: Example of relaxation and creep of material (Hajikarimi and Nejad, 2021)

In order to describe the time-temperature-dependency it is necessary to explain the origin of the complex shear modulus ($G^*(i\omega)$) and phase angle ($\tan(\delta(\omega))$). Both are calculated by using the storage and loss modulus of the material, denoted by G' and G'' respectively. The latter measures the dissipated energy as heat and is caused by the viscous part of the total energy and is 90° out of phase with the applied strain. The storage modulus measures the stored energy and represents the elastic portion of the energy, which is in phase with the applied strain. To determine these modulus the following integrals should be used (Hajikarimi and Nejad, 2021):

$$G'(\omega) = \int_0^\infty \omega G(\eta) \sin(\omega\eta)\, d\eta \tag{2.27a}$$

$$G''(\omega) = \int_0^\infty \omega G(\eta) \cos(\omega\eta)\, d\eta \tag{2.27b}$$

in which ∞ is the time required for the viscoelastic material to reach steady-state conditions. Now, with the storage and loss modulus we can define the complex shear modulus and phase angle as:

$$\left|G^*(i\omega)\right| = \sqrt{(G'(\omega))^2 + (G''(\omega))^2} \tag{2.28a}$$

$$\tan(\delta(\omega)) = \frac{G''(\omega)}{G'(\omega)} \tag{2.28b}$$

Determining the viscoelastic material properties

In order to experimentally retrieve the complex shear modulus and phase angle of the material, Dynamic Mechanical Analysis (DMA) should be applied to a test sample (Groenewoud, 2001). The test sample of specified geometry is subjected to a sinusoidal deformation. The geometry of the test specimen should be in accordance with the ISO standards (ISO 7743:2011, E). The amplitude of deformation is related to the stiffness. The DMA measures amplitude and the phase difference between the in- and output. Using the knowledge to calculate the phase angle ($\tan(\delta)$) and complex shear modulus (G^*), reversed calculations can be performed to determine the storage and loss Moduli, respectively G' and G''.

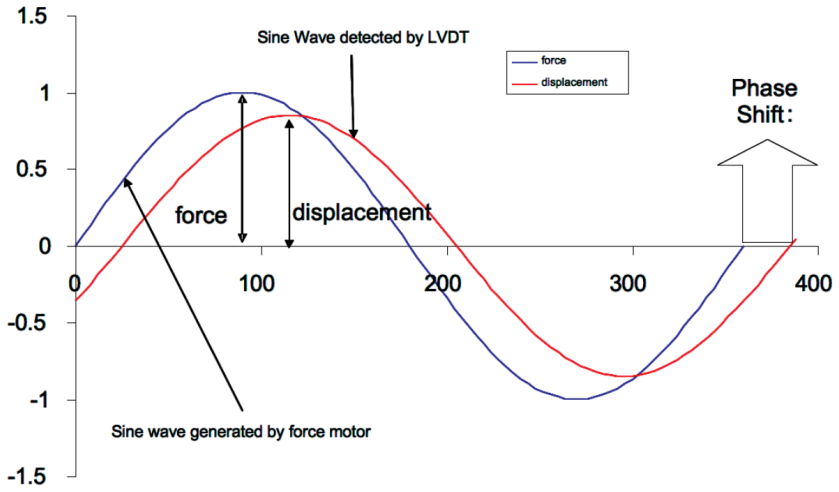

Figure 2.9: Measuring the phase shift and sinusoidal stress to strain using DMA (PerkinElmer Inc, 2013)

2.4.2. Temperature and frequency dependency

In the books of Gent and Scott (2012) and Bergström (2015) the temperature and frequency dependency of polymers is thoroughly illustrated. The temperature strongly affects the internal viscosity between molecular chains which is the main cause of delayed elastic response. In Gent and Scott (2012) it has been given that the dependence of the temperature can be given by the characteristic law:

$$\ln\left[\frac{\varphi(T)}{\varphi(T_g)}\right] = \frac{A(T-T_g)}{B+T-T_g} \tag{2.29}$$

in which A and B are constant values of for most elastomers 40 and 50°C, respectively, φ is the rate at which small segments of a molecule move and T, T_g are temperatures. The latter of the temperatures denotes the reference temperature which is, in turn, the most important parameter determining the dynamic behavior of an elastomer. It is the temperature at which the molecular segments do not move at all after 10 seconds and behave like a rigid glass. When plotting the relationship between the frequency and the complex shear modulus or phase angle, a lateral shift ($\ln a_T$) could be used when taking the effect of the temperature into account. This shift is based on the William-Landel-Ferry (WLF) equation. The lateral shift is determined by (Gent and Scott, 2012):

$$\ln a_T = \frac{\ln\left[\frac{\varphi(T_2)}{\varphi(T_1)}\right] \cdot A \cdot C\,(T_2 - T_1)}{(52 + T_2 - T_g)(52 + T_1 - T_g)} \tag{2.30}$$

in which T_1, T_2 denote the temperatures of two distinct moments in time and C denotes a material constant which is 32.6 in case of a polyurethane polymer. This allows to use create a so called "master curve" which is the dynamic modulus plotted versus the frequency, as depicted below.

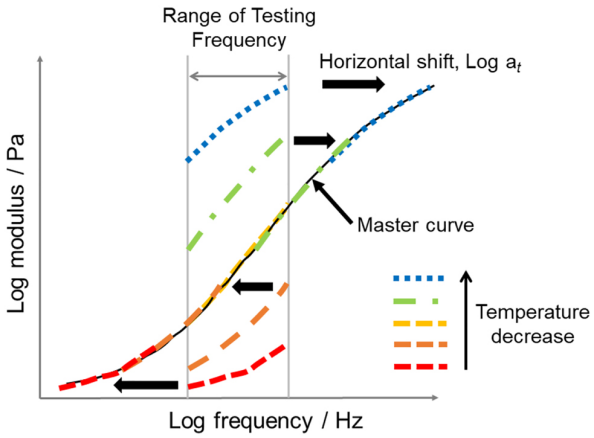

Figure 2.10: Example of influence of time-temperature relation master curve (Ramli et al., 2022)

As can be seen from this graph, the higher the frequency, the stiffer the material becomes. This behavior is expected as the material does not have the time to adjust to the load. The opposite is also valid where the lower the frequency, the softer the material behaves where it has enough time to allow creep. When increasing the temperature, the material becomes softer which is also to be expected as the temperature goes further away from the glass temperature.

2.4.3. Hyperelasticity

In the previous sections, the linear viscoelastic property of the polymer material is discussed. However, PU is a hyperelastic material, meaning that it this property is valid to predict large strains situations, introducing nonlinear effects. This section will briefly explain the effect of the nonlinearities and show how the material properties can be tested in order to describe the nonlinear stress-strain behavior.

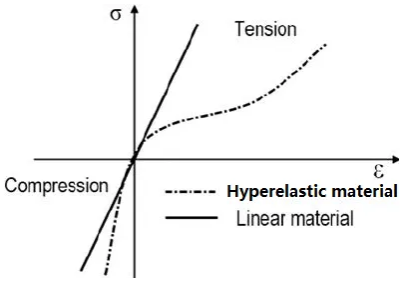

Figure 2.11: Typical nonlinear stress-strain behavior of a hyperelastic material

Hyperelasticity has the characteristic where the material can withstand large deformations up to 700% or more, while being able to deform elastically back to its original shape. In addition, another characteristic of hyperelasticity is that the material is (almost) incompressible, meaning that the volume is constant when being compressed or tensioned.
Different hyperelastic models can be used in order to employ this effect into practice. The four most commonly known are:

- Neo-Hookean
- Mooney-Rivlin
- Ogden
- Arruda-Boyce

These models are based on the Helmholtz free energy per unit reference volume which only consist of the material constants to predict the nonlinear thermodynamic behavior. A difference in the Helmholtz free energy during a process is equal to the maximum amount of work that the system can perform in a thermodynamic process in which temperature is held constant. At constant temperature, the Helmholtz free energy is minimized at equilibrium. In the book of Bergström (2015) it is shown that the Helmholtz free energy can be determined by:

$$\Psi = e_0 - \theta_0 \, \eta_0 \tag{2.31}$$

where e_0 represents the internal energy per unit reference volume, θ_0 the reference temperature and η_0 the entropy per unit reference volume of the material. As an example for determining the stress-strain behavior, in this section the Neo-Hookean model is described, which is presumably the easiest to apply in practice. The Neo-Hookean model is based on just two parameters: the shear modulus μ and the bulk modulus κ. The latter represents the resistance to the compression and is often referred to as the incompressibility of the material. To describe the stress-strain behavior of the Neo-Hookean model in terms of the Helmholz free energy principle, the following expression can be used:

$$\Psi(I_1, J) = \frac{\mu}{2}(I_1 - 3) + \frac{\kappa}{2}(J-1)^2 \tag{2.32}$$

in which I_1, J represents the invariants of the Helmholtz free energy principle which is determined by the principle stretches $\lambda_1, \lambda_2, \lambda_3$. Rewriting this equation based on the Cauchy stress gives:

$$\sigma(J) = \frac{\mu}{J}[\boldsymbol{b}^*] + \kappa(J-1)\,\boldsymbol{I} \tag{2.33}$$

$\boldsymbol{b}^*$ represents the Left Cauchy-Green tensor which in turn represents the local change in distance due to deformation (Bergström, 2015). When assuming that the material is fully incompressible, the value $J = 1$, the second term becomes equal to zero. This equation is now able to reproduce the nonlinear behavior of the stress-strain as illustrated in Figure 2.11.

Determining nonlinear material parameters
Each of the different theories to describe the nonlinear hyperelastic behavior of the material need different amounts of material properties. In Bergström (2015) it is shown that the theories acquire 2 to 8 material parameters. The higher the amount of known linear parameters, often results in higher accuracy when using the Schapery procedure (Brinson and Brinson, 2015). In order to get these values, experiments are to be performed. The amount of required tests depend on the combination and amount of parameters.

For the less complex methods such as the Neo-Hookean, only 2 parameters, which in turn are both dependent on one single variable (I_1). In case of more complex models, such as the Ogden model, two experiments should be performed to acquire the value for the I_2 dependency. An example could be to perform a uniaxial or biaxial tension test.

2.4.4. Hyper-viscoelasticity

With the properties of viscoelasticity and hyperelasticity a better understanding of the combined behavior can be given. Previous study shows that shows a hyper-viscoelastic constitutive model is proposed based on modifications of the hyperelastic Mooney-Rivlin and Ogden models (Somarathna et al., 2020; Ucar and Basdogan, 2018). The stress-strain behavior of this model shows a good agreement with experimental data. In Figure 2.12 a representation of the combined material properties of PU material is given.
In a study performed by Wang et al. (2017) the dynamic damping characteristics of a similar hyper-viscoelastic model is given where it is concluded that the rise of the temperature due to compression leads to a reduced relaxation modulus, ultimately lowering the overall Young's Modulus of the material. The stiffness as well as the damping coefficient decreased when the temperature increased.

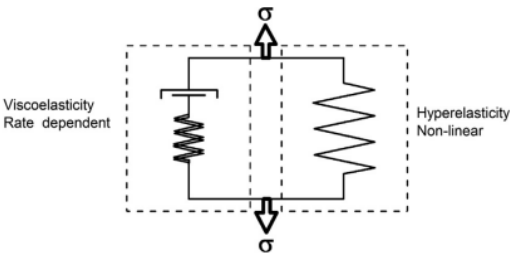

Figure 2.12: Representation of a hyper-viscoelastic model (Qi and Boyce, 2005)

In the MCGF system, compression due to the prestress is expected to not be an instantaneous load, hence no reduction of the material stiffness by increased temperature. However, assuming that the rollers exhibit no friction and rotate purely, it could be argued that the axial displacement during pile driving causes a rotating movement of the rollers, supplying new, uncompressed PU. The diameter of the roller is 1.07 m of which the outer layer consist of a 65 mm thick layer PU (h_{PU}). In current internal preliminary calculations by HMC the maximum indentation of the material is assumed to be 13 mm. The indentation results in a contact surface length of $z_c \approx 332$ mm with the MP.

The axial displacement and thereby rotation of the roller is highly dependent on the soil conditions. The deeper the pile is embedded in the soil, the higher the shaft resistance becomes and deeper layers often consist of harder material to penetrate. In the pile driving the amount of blows are often given in terms of blows/0.25m. Research has indicated that approximately 20-60 blows/0.25m are typical values for pile driving (Argyroulis, 2022; Parola, 1970). This translates to displacements that range from 4.2-12.5 mm per blow. The ratio of 'new' material to the already compressed layer is low (<4%). The blow rate is in the range of approximately 25 blows/min at maximum hammer energy which results in a fully new supplied piece of material after at least 66 s. This low ratio could suggests that the prestress does not significantly impact the increase in temperature, and consequently, the stiffness of the material remains relatively stable. However, the effect of rising temperature due to the compression is not quantitatively describable with the current knowledge.

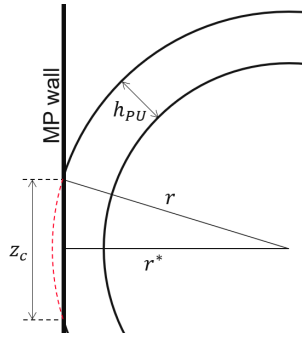

Figure 2.13: Section view of roller at RB height showcasing indentation of roller

In this report, the influence of the roller material is linearized. The material properties are not experimentally determined and are therefore approximated. Preliminary calculations at HMC have indicated that a spring stiffness of 200 kN/mm can be assumed for the rollers. This value will be used as the base case in chapter 3. In chapter 4, the effect of the damping and stiffness values of the rollers on the expected vibrations will be studied, showing what values are required to dampen the vibrations properly. Modeling the nonlinear properties of the rollers would require more complex theories to solve the system, and could unpredictably amplify or dampen the actual vibrations. When compressing the PU layer, the stiffness increases as the polymer chains within the PU start to reorganize under pressure. Simultaneously, the friction resulting from the movement of these chains leads to an increase in temperature, consequently reducing the stiffness. The complexity and conservative nature of predictions are reasons to opt for a linearized roller model.

3

Axisymmetric model

To visualize the vibrations, three different models are proposed, each building in complexity to gain a better understanding of the combined phenomena that could occur when modeling the total system. Firstly, the MP model is separated from the RB, which is only loaded under the influence of the hammer impact. The effect of a fixed spring-dashpot system is added to see a direct correlation between the ballpark stiffness value and the axial and radial behavior of the MP. Next, the RB is also modeled separately, simplifying the model to that of a beam. Using the radial displacement of the MP model as input for this model provides an expected behavior of the RB. Both of these models will be validated through mesh convergence studies for both the ode45 and BDF2 solvers. Combining these models ultimately results in the coupled model where the interaction of the rollers is visualized. The main difference between the coupled model and its predecessors is an active roller interaction between the MP and the RB. All models will be implemented in the FEM package Abaqus to check whether the assumptions within the numerical solvers in Matlab correspond to those in this program.

In this chapter, a base case is assumed where the maximum possible diameter for the MCGF is used. The dimensions of the MP regarding the length and wall thickness are based on internal data related to upcoming projects for HMC. However, the choice of diameter is made such that the impact of wave dispersion can be more distinctly observed and analyzed. In chapter 4 the parameters are subject to change to observe its individual influence.

Parameter	Symbol	Value	Unit
Monopile dimensions			
Outer diameter	D_{out}	12.5	m
Wall thickness	h_{MP}	0.1	m
Length	L_{MP}	110	m
RB height (measured from top)	z_{RB}	20	m
Steel parameters			
Density	ρ	7850	kgm^{-3}
Youngs Modulus	E	210	GPa
Poissons ratio	ν	0.3	-

Table 3.1: Dimensions of MP and steel properties used for the base case

3.1. Monopile model

In the previous chapter it has been shown how the EOMs of a cylindrical shell are derived and what type of solvers can be used to solve the equations. Here, a representation of the EOM will be given where it is made possible. In order to use the MATLAB solvers, the equation are to be rewritten using the central difference form. In the book of Vuik et al. (2023) it is shown that central differences show a smaller truncation error than their counterpart backward and forward differences. The output of the ODE solver in MATLAB determines the predicted displacements and velocities. However, for the purposes of this study, the primary focus is on accelerations, which can be derived by taking the gradient of the output velocities.

3.1.1. Setting up the model

In Appendix A the discretized form of the EOM from Equation 2.15 is shown which are repeated down below. This discretized form is required in order to solve this system of ODEs with MATLAB.

$$\sum_{n=1}^{N}\left\{\frac{\partial^2 u_n}{\partial t^2}+\frac{c_p^2}{\Delta z^2}\left(-u_{n-1}+2u_n-u_{n+1}\right)+\frac{c_p^2\nu}{2\Delta z\,R}\left(w_{n-1}-w_{n+1}\right)\right\}=0 \tag{3.1a}$$

$$\sum_{n=1}^{N}\left\{\frac{\partial^2 w_n}{\partial t^2}+\frac{c_p^2}{R^2}w_n+\frac{\nu c_p^2}{2\Delta z\,R}\left(-u_{n-1}+u_{n+1}\right)+\frac{c_p^2\,h_{MP}^2}{12\Delta z^4}\left(w_{n-2}-4w_{n-1}+6w_n-4w_{n+1}+w_{n+2}\right)\right\}=0 \tag{3.1b}$$

The last term containing the fourth order derivative with respect to space represents the added bending term which is discussed in the previous chapter. This term distinguishes itself from the membrane theory, becoming the cylindrical shell theory. These equations are the base of the model represented in this thesis. In Figure 3.1 a general overview of the MP model is given. As can be seen from this figure, the bottom is assumed to be in fixed. It is expected that all energy of the propagating wave reflects from this boundary as there is no ability for the energy to be reduced. The fixed conditions assumed that the displacement and angle of the MP at the bottom should be zero:

$$u_1|_{z=L}=w_1|_{z=L}=\left.\frac{\partial w_1}{\partial z}\right|_{z=L}=0 \tag{3.2}$$

The top part of the MP is assumed to be a free end where only the force acts in axial direction. The current shell theory is based on axisymmetric conditions, assuming that the non-verticallity in the impact is negligible for the current analysis. The BCs at the top part of the MP can be given as:

$$\left.\frac{\partial^3 w_1}{\partial z^3}\right|_{z=0}=\left.\frac{\partial^4 w_1}{\partial z^4}\right|_{z=0}=0 \tag{3.3a}$$

$$\left.\frac{\partial u_1}{\partial z}\right|_{z=0}=\frac{F(t)}{EA} \tag{3.3b}$$

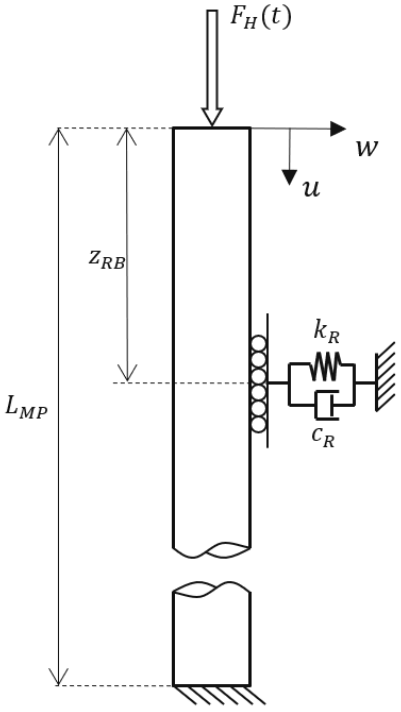

Figure 3.1: Overview of the MP model

Next, an important aspect of this model is how the input force is defined. The force is often given in terms of an $F(t)$-diagram. For reference material, internal data for the $F(t)$-diagram is used which is given in Figure 3.2a. However, for future considerations within this thesis, specifically in the parameter study where we will explore the impact of the force, the input force will be fitted to a Weibull curve for analytical purposes.

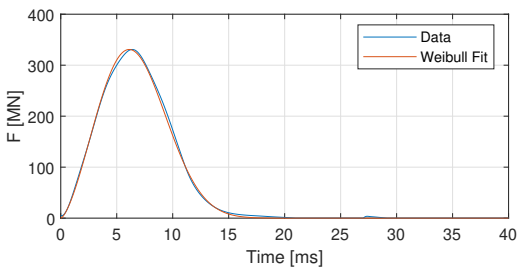

(a) Force time diagram ($F(t)$)

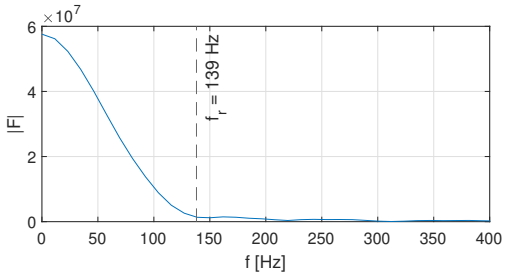

(b) Frequency spectrum

Figure 3.2: $F(t)$ curvefitted with a Weibull diagram for a large diameter MP together with its frequency spectrum

Considering that wave dispersion is a significant factor in this model, it is essential to understand the frequencies present in the input signal. By employing a Fast Fourier Transform (FFT), the frequency spectrum can be generated and visualized. In this graph it can be seen that the expected ring frequency (f_r) is clearly within range of the spectrum, thus it is expected that wave in the vicinity of this frequency do not propagate.

3.1.2. Configurations monopile model

First a mesh convergence test should be performed to ensure accurate results while reducing the computational time as much as possible. From this graph it can be concluded that a mesh size of $\Delta z = 1$ m is sufficient as this deviates 0.1% of the maximum value with a mesh size of $\Delta z = 0.01$ m for both methods. In addition, it is worth noting that the simulation time for the ode45 solver in case of $\Delta z = 0.01$ is 20.5 minutes[1], which is much higher than the 4 seconds needed for the BDF2 solver.

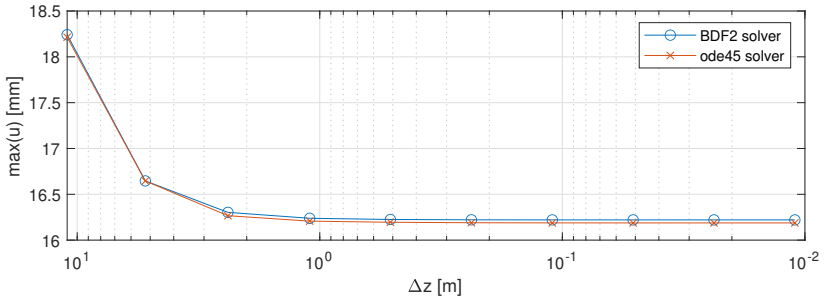

Figure 3.3: A plot of the maximum axial amplitude to check the mesh convergence

A small difference between the maximum values of the solvers can be found. Due to the BDF2 solver being an implicit solver allows to set the time step as an extra variable. In Figure 3.3 a time step of $\Delta t = 0.1$ ms is chosen which results in 1000 time steps to reach the final result when having a total simulation time of 0.1 s. In the figure below it can be seen that a time step of $\Delta t = 1e-5$ ms results in accurate data.

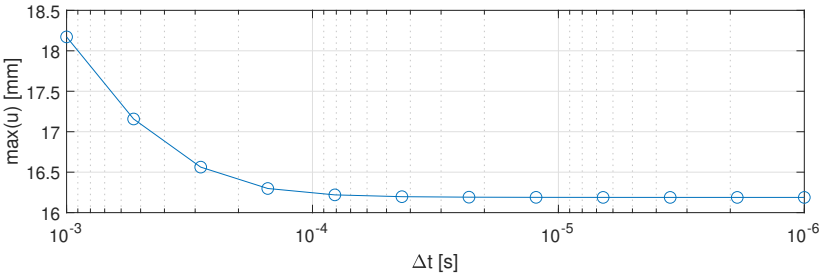

Figure 3.4: A plot of the maximum axial amplitude to check the time convergence of the BDF2 method

3.1.3. Monopile model results

With the mesh size and time step being considered accurate, the total results of the MP model can be computed. Since the difference between the ode45 and BDF2 solver are thus small, it is chosen to proceed with the BDF2 solver. In Figure 3.5a & 3.5b the axial and radial displacement of the MP is given. The behavior of the axial displacement is as expected where the hammer impact compresses the MP by approximately 16 mm. Once the wave has propagated through the entire pile, reaching the fixed bottom of the pile, seems to disappear due to the displacement being zero. This effect can be explained by means of a "image" pulse and is described in Metrikine and Vrouwenvelder (2018). The image pulse represents an imaginary pulse that move in the opposite direction of the incident wave. This image wave is, similarly to the incident wave, a compressional wave in case of a fixed end. On the other side, when the wave has propagated towards the top end of the pile, a free end is reached. The theory of this image pulse is also valid here, however, the image wave of a free end is in opposite direction. This results in a tensional wave which explains why the MP stretches out at the top at $t \approx 42$ ms.

[1]The simulation highly depends on the specifications of the used computer and could differ on other computers.

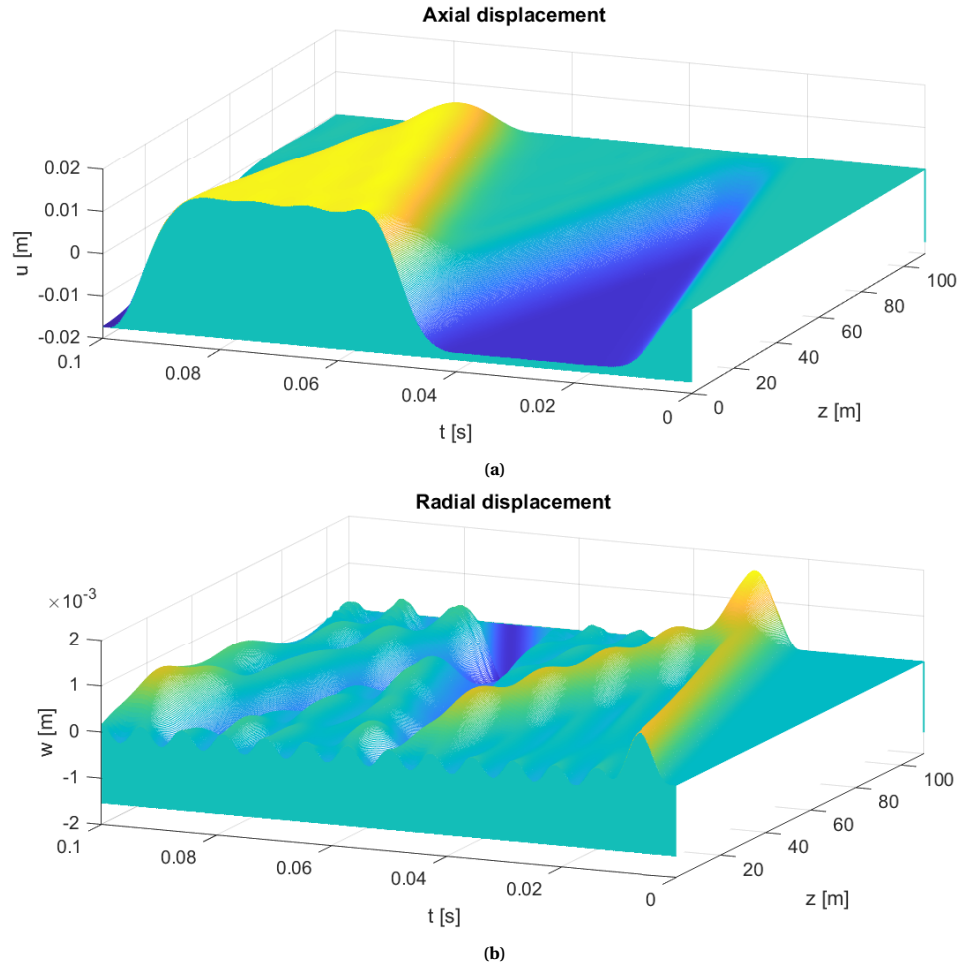

Figure 3.5: Axial (a) and radial (b) displacement in time and space for a large diameter MP

Furthermore, the effect of the trapped wave is also showcased in Figure 3.5b where it can be seen that even when the input of the hammer force has passed ($t \approx 0.017$ s), the top part of the MP start to vibrate at its eigenfrequency (ring frequency) of 139 Hz. The current used shell theory is able to show this wave dispersion effect. The radial expansion phenomenon, known as the "breathing" of the MP, results in extra, smaller propagating waves as well. Consequently, after the initial wave reaches the bottom of the MP, it encounters interference from this breathing effect, leading to fluctuations in the initial propagation from the point of reflection onwards. The overall behavior of the vibrations is also captured in a study by MacGillivray (2015).

Despite the fact that these graphs contain numerous amounts information, it is more convenient to showcase 2D plots as these are less complex to interpret than the preceding 3D images in space and time. In Figure 3.6 the axial and radial displacements of the MP model at different moments in time before reaching the bottom part of the MP are shown ($t < 20.3$ ms. Comparing these graphs with the force input from Figure 3.2a it can be observed that the most of the energy of the input has a time span ($\Delta t_F \approx 13$ ms), which results in a spatial wave length of approximately 70 m. From both the axial and radial displacement this could be confirmed which is expected due to $c_p \cdot \Delta t_F = 70.5$ m.

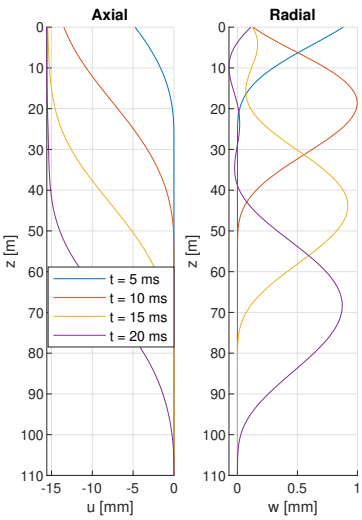

Figure 3.6: Axial and radial displacements for different time stamps

Shell vs. membrane theory
This paragraph highlights the distinctions between the current shell theory, which includes the added DM term, and the rod equation. It is obvious that there is no radial displacement computed with the rod equation, hence not given in the figure below. First, it can be seen from both graphs that the shell theory resembles the output of a membrane model. The radial displacement fluctuates consistently between -0.2 and 0.2 mm after the initial wave has passed.

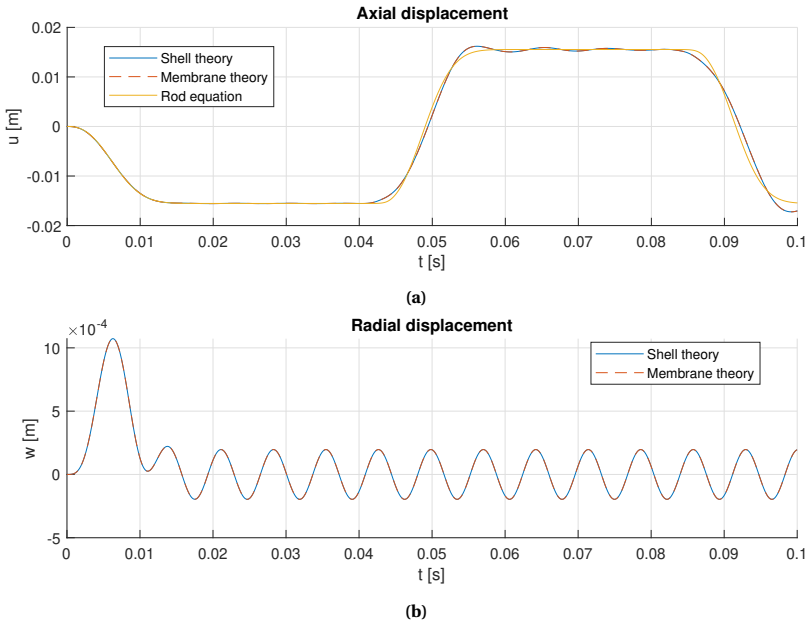

Figure 3.7: Different theories for axial (a) and radial (b) displacement of first node MP model

It is observed that radial vibrations rebound back into axial vibrations, causing the axial vibrations to oscillate around the equilibrium. This effect is also evident in Figure 3.5b, where the initial wave appears to propagate smoothly. However, for $t > 0.03$ s where the wave reflects on the bottom of the pile, the waves become a superposition of the reflected, initial and the opposing propagating breathing waves.

3.1.4. Monopile model compared to FEM data

To validate the aforementioned MP results, FEM analyses are performed in order to compare the results. Throughout this research, the FEM package Dassault systems SIMULIA Abaqus FEA 2021, henceforth referred to as Abaqus, is utilized. This program allows to solve the problem implicitly and explicitly. Within Abaqus, the implicit solvers are based on Backward Euler method, whereas the explicit solvers are based on Forward Euler. The type of FEM models that are used to compared are:

- Shell model (implicit/explicit);
- Membrane (implicit);
- $1/8^{\text{th}}$ of circumference of the MP (explicit);
- Solid (explicit).

In this context, the $1/8^{\text{th}}$ represents a section of the MP where the edges are rigidly connected by adding BCs such that these represent the neighboring parts of the MP. This model is also modelled as a shell. Ultimately, the axisymmetric conditions are still met via the BCs. The three other models are axisymmetric models. A more detailed description of all models are given in Appendix B.

When comparing displacements of the models in Figure 3.8 at the position of the RB ($z = z_{RB}$), it is illustrated that the axial displacement are completely in line for all models. When considering the radial displacement, it is shown that the maximum amplitude of the FDM Matlab model is similar to those of the FEM models. However, after the initial wave has passed, the Matlab shows higher frequencies in the radial direction. As the amplitude is small compared to its maximum, this effect is not of interest.

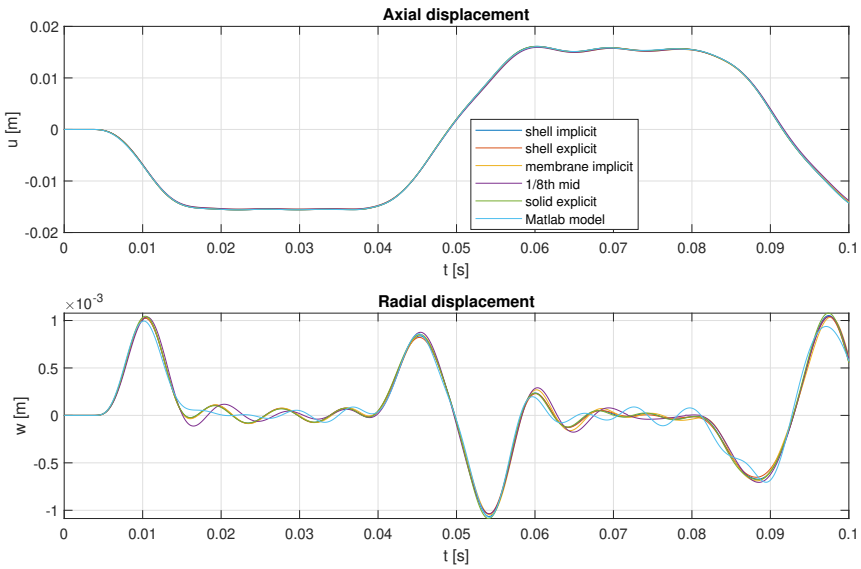

Figure 3.8: Comparison MP FEM models in Abaqus in axial and radial direction at RB position ($z = z_{RB}$)

3.1.5. Monopile model with a fixed roller

The investigate the influence of the roller on the output of the MP model, a fixed spring-dashpot system is added to represent the contact of the roller. The values of the spring stiffness and damping coefficient are based on internal estimations by HMC. The value of k_R is estimated to be approximately 200 kN/mm. The damping ,however, is not given and it is assumed for this base case to be $1e^{-5}$ times the spring stiffness. These values represent the base case which will ultimately be changed in a more detailed study in the next chapter.

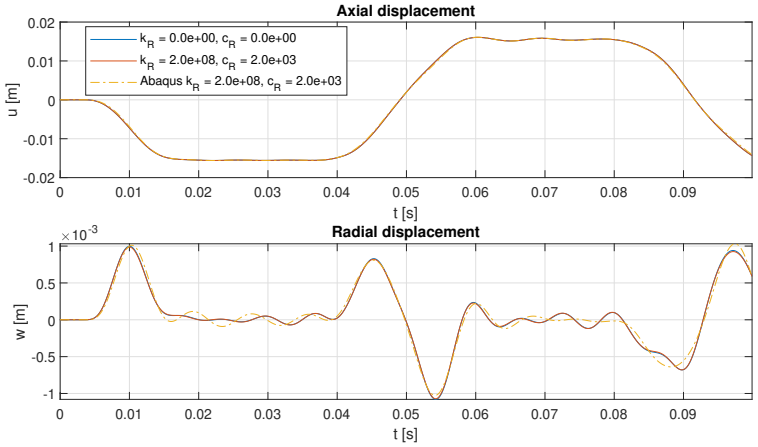

Figure 3.9: Axial and radial output of MP model at RB position comparing the system with and without the influence of a fixed roller

From these graphs it can be concluded from the FDM Matlab and Abaqus models that the current spring stiffness of k_R = 200kN/mm does not influence the behavior of the vibrations in axial direction. In radial direction, after the initial has passed ($t > 16$ ms) the radial expansion starts to vibrate in its own eigenfrequency of 139 Hz. Between both MATLAB models there is no difference in behavior noticeable, whereas the Abaqus model shows a small phase shift that changes this frequency to ≈ 110 Hz. The amplitudes of the models appear similar for the initial peak. Upon closer examination of the MATLAB models, a minor difference of 1.1% is dampened out by the rollers whereas the Abaqus model shows an increase of 1.4% in amplitude. With the current configuration, little to no effect of the rollers is shown by the model. However, in this model the other end of the spring-dashpot system is assumed to be a fixed point. In reality, this point, attached to the end of the RB, will move independently which could show a different influence of the attached spring.

3.2. Rollerbox model

In this section the RB is separately modelled to investigate what the influence of a spring is to the deflection of the beam. It is important to note that only the transverse deflection is modelled as it is expected that the highest deflections and thereby the highest accelerations will be calculated. Additionally, analyzing the longitudinal deflection would involve addressing the nonlinear behavior of a beam, which would require a different approach when formulating the EOM. The simplified beam EOM, also known as the Euler-Lagrange beam equation, can be described by:

$$\rho A \frac{\partial^2 w_{RB}}{\partial t^2} + EI \frac{\partial^4 w_{RB}}{\partial x^4} = 0 \tag{3.4}$$

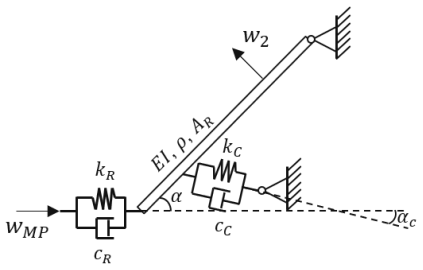

Figure 3.10: Overview of the RB model

The right end of the beam represents the connection of the beam with the gripper ring. The gripper ring is for the purpose of this study to be infinitely stiff. The left side of the beam is again a free end which is loaded by a forced displacement (w_{MP}). This displacement is the output of the MP model at the height of the RB without effect of a spring attached to the MP ($k_R = 0$).
The same methodology for solving this system of equations and its BCs is used as for the previous section. A more detailed explanation on the implementation of the BCs and ICs can be found in Appendix A. The BCs can be described as:

$$EI \left.\frac{\partial^3 w_{RB}}{\partial x^3}\right|_{x=0} = -k_R \left(w_{RB,1} - w_{MP}\right) - c_R \left(\frac{\partial w_{RB,1}}{\partial t} - \frac{\partial w_{MP}}{\partial t}\right) \tag{3.5a}$$

$$\left.\frac{\partial^2 w_{RB}}{\partial x^2}\right|_{x=0} = 0 \tag{3.5b}$$

The RB is pressed against the MP by hydraulic cylinders which is modelled as a spring-dashpot system. The values of the spring and dashpot are denoted as k_{hc} and c_{hc} respectively. These cylinders prestress the MP to keep its position within the allowed misalignment tolerances. In this study, the effect of the rollers are assumed to be linear. Therefore, it can be assumed that the prestress of these cylinders do not influence the dynamic behavior of the rollers. The prestress induces an initial deformation, which maintains the same dynamic behavior around this new equilibrium position.

The shape of the RB is similar to that of a hollow rectangle, where in reality stiffeners are used to strengthen the structure. However, for the purposes of this thesis, the RB's shape is simplified to that of a hollow rectangle, assuming it to be free from imperfections or any other factors that might changes its geometry.

Parameter	Symbol	Value	Unit
Rollerbox dimensions			
Height	h_{RB}	0.5	m
Width	b_{RB}	2.881	m
Length	L_{RB}	6	m
Thickness sides	$t_{RB,side}$	120	mm
Thickness top and bottom	$t_{RB,tb}$	20	mm
Angle of RB w.r.t. MP	α	90	°
Angle of hydr. cyl. w.r.t. RB	α_c	80	°
Hydraulic cylinder parameters			
Oil bulk modulus	κ_{oil}	1000	MPa
Stroke	l_{hc}	2650	mm
Bore diameter	D_{bore}	430	mm

Table 3.2: Rollerbox dimensions

The angle of the RB is assumed to be 90° with respect to the MP for the validation of the model. This value in reality ranges from 51-81°, depending on the diameter of the MP. Due to the direction of the forces of the radial expansion of the MP being the only transferred loads onto the RB, the angle of the RB is simply a multiplication of $\sin(\alpha)$ times the amplitude. The angle of the hydraulic cylinder (α_c) varies with the angle of the RB with a range of 58-80°, with the largest angle occurring when dealing with a 12.5 m diameter MP.

3.2.1. Rollerbox model configuration

Similar methods to those used in the MP model are employed to determine the appropriate mesh size and time step. For the purpose of analysing the mesh size, the influence of the hydraulic cylinder is discarded ($k_c = c_c = 0$). Furthermore, the gripper ring end is now treated as a clamped end, as in reality, the beam would rotate around the hinge when not clamped. The RB model appears to become slow when using the ode45 solver. In case of a value of $\Delta x = 0.019$ a simulation time of 80 minutes is required, whereas the BDF2 solver instantly (<< 1 s) computes the results with the same mesh size.

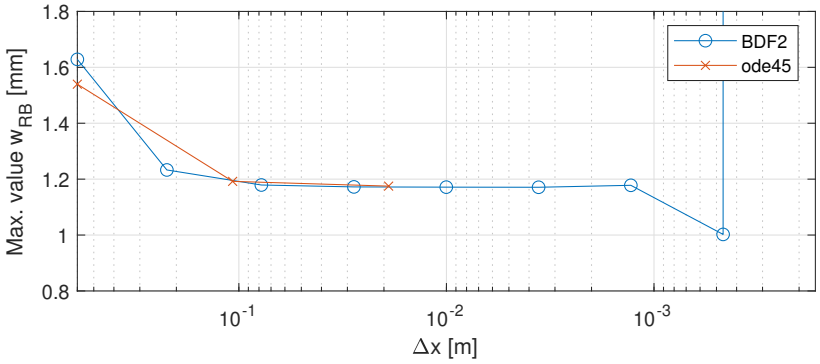

Figure 3.11: A plot of the maximum transverse displacement to check the mesh convergence

When the mesh size reaches below $\Delta x < 0.001$ m the system becomes unstable. This phenomenon, numerical instability, can be explained by the fact that this problem can be considered as a stiff problem and has therefore to be solved by means of the BDF2 solver since this solver is unconditionally stable. The numerical stability of a system is explained in further detail in chapter 2. As can be seen in the graph above, a converged amplitude is reached at $\Delta x = 0.08$ m with a time step of $\Delta t = 0.1$ ms as this value deviates 0.6% from the asymptotic value. Choosing a larger time step could make the system stable but less accurate. Therefore, this combination of mesh size and time step is considered accurate enough to proceed with further calculations. Because the required mesh size is relatively large (100 elements), the ode45 solver can still be used.

3.2.2. Rollerbox model compared to FEM data

In order to visualize the effect of the roller to the deflection of the beam, the hydraulic cylinder is still discarded. Later on, this effect will be included to see what the differences are. The FEM model is adjusted accordingly to match the BCs. In the figure below the displacement and accelerations of the left end of the beam are shown together with the forced displacement on a spring (w_{MP}) to this model. The input is better shown in Figure 3.8.

In the graphs below it can be seen that the ode45 and BDF2 solvers show similar output. The amplitude of the output seem to increase to higher levels than the maximum output of the input in the numerical models as well as the FEM simulation. At first the Matlab and FEM models seem to have the same behavior, with a similar phase difference between the output and input up to approximately $t = 0.035$ s. After this point the FEM simulation seems to react 'slower'. This phase difference might be caused by the assumption of the beam being modelled by the uncoupled Euler-Lagrange beam equation, whereas the FEM model is considered as a 3D-beam. A similar phenomena is demonstrated when comparing the wave speed in a rod (c_0) with that of the axisymmetric shell (c_p), where the rod exhibits a lower wave speed. However, with a beam of 6 m in length, the reflected waves are expected after $t \approx 2.3$ ms, considering a wave speed of 5.4 km/s.

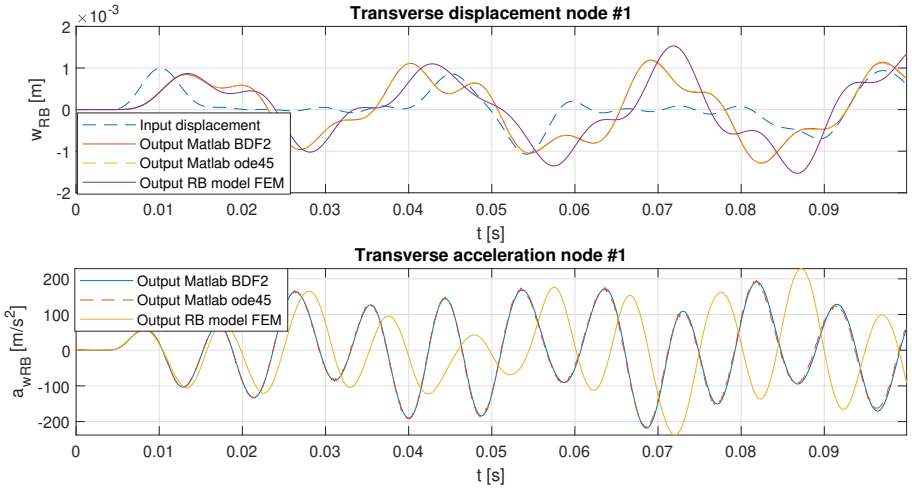

Figure 3.12: The transverse displacement and acceleration of the first node (MP side) of the RB comparing the input displacement versus the numerical results by Matlab and Abaqus

In order to get a better understanding of the propagating waves in this model, the reflecting waves should be discarded. To eliminate this effect, the length of the beam can be extended to over 271 meters to ensure that reflections do not significantly impact the results. This is employed to the model which result in the following:

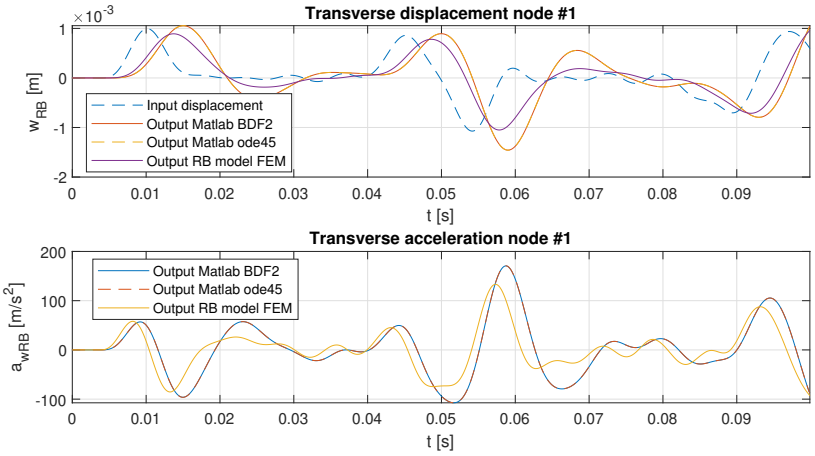

Figure 3.13: The transverse displacement and acceleration of the first node (MP side) of an extended RB ($L > 271$ m)

With the RB extended up to 271 m, the phase difference is still visualized by the output. The amplitude of the transverse displacement of the RB does not seem to significantly increase over time, albeit show an increase of 1.5 times the input for the minimum amplitude. From Figure 3.12 & 3.13 it can be concluded that the behavior of the vibrations can be accurately showcased by the current model. In section 3.1 it is shown that a fixed spring does not significantly influence the radial expansion of the MP. Hence, the current amplitude of the RB model should be in the range of approximately ± 200 ms^{-2} in case of the normal length RB of 6 m.

Influence of hinged BC and hydraulic cylinder

In this part the hydraulic cylinder is added to the system, which allows to change the BC of the RB on the gripper ring end to be hinged instead of clamped. The change in BC changes the K-matrix which is explained in further detail in Appendix A. The spring stiffness of the hydraulic cylinder are based on the following calculation (Khalil, 2009):

$$k_{hc} = \kappa_{oil}\left(\frac{A_1^2}{V_1 + V_{L1}} + \frac{A_2^2}{V_2 + V_{L2}}\right) \tag{3.6}$$

in which κ is the oil bulk modulus, l_{hc} is the stroke of the cylinder, V_{L1}, V_{L2} are the fluid line volumes and A_1, A_2 and V_1, V_2 are the area and volume before and after the piston, respectively. The stiffness is at its lowest when the piston reaches the middle of the cylinder stroke ($l_{hc}/2$). When assumed that the fluid line are small compared to the contained oil volumes V_1, V_2 it can be assumed the equation can be simplified:

$$k_{hc} \approx 4\kappa_{oil}\left(\frac{A_1}{l_{hc}}\right) \tag{3.7}$$

Using the values from Table 3.2 the hydraulic stiffness is estimated to be 223 kN/mm. The damping value is again assumed to be a factor of $1e^{-5}$ lower. In the figure below, the results of the RB including hinged BC and hydraulic cylinder are computed by the FDM model. It can be seen that the hydraulic cylinder reflects part of the energy of the waves, resulting in lower displacements between the attachment point of the cylinder and the gripper ring.

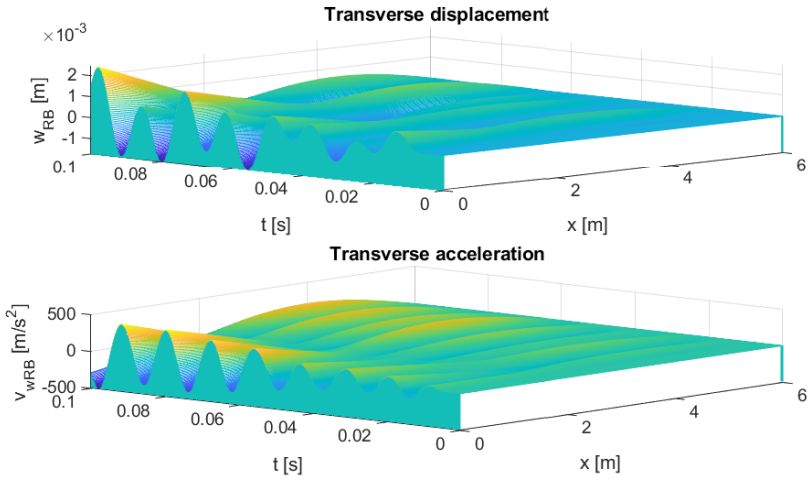

Figure 3.14: The transverse displacement and acceleration of the RB including hinged BC and hydraulic cylinder

However, the results seem to increase in amplitude, which is caused by these reflected waves. First, the different numerical methods with the FEM of the first node should be compared in order to validate this behavior by FEM:

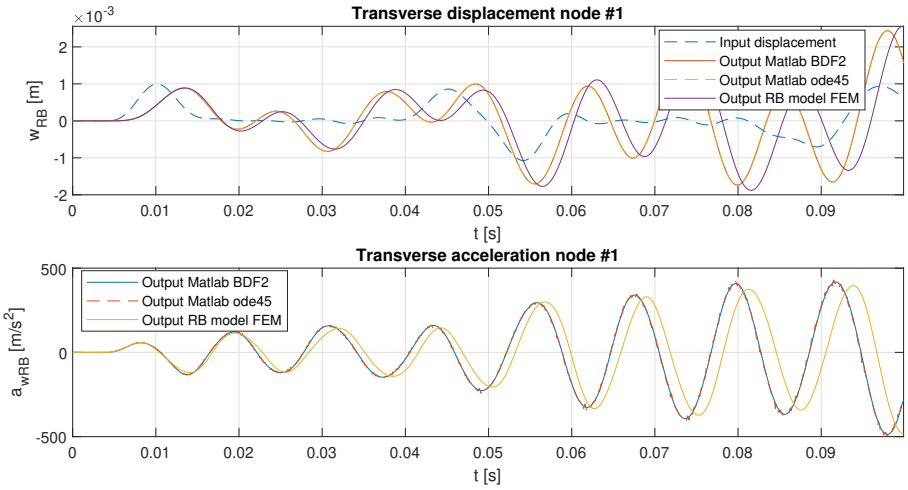

Figure 3.15: The transverse displacement at node #1 of the RB including hinged BC and hydraulic cylinder

Figure 3.15 shows that the numerical FDM methods are in agreement with the behavior of the FEM simulation. The amplitude increases, reaching values up to 500 m/s^2. This effect indicates that the system is

marginally stable. In this case, it is not numerical stability that plays the main role, but structural stability. In the figure below, a longer time frame is given where it can be seen that the vibrations can go up to even 600 m/s^2.

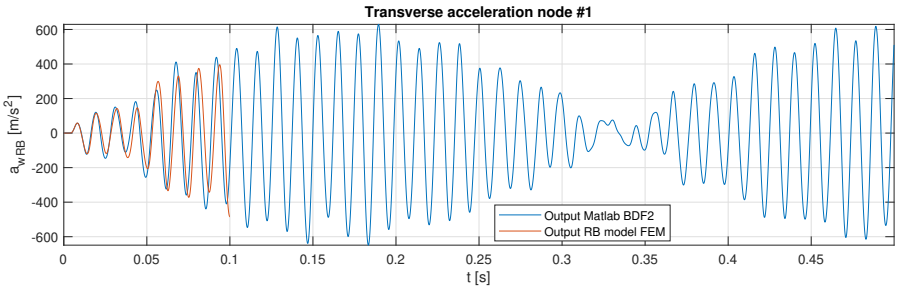

Figure 3.16: The transverse acceleration showcasing the close-to-instability of RB system

This effect occurs when two (or more) frequencies are close in range to one another. The next step is to consider that this might be close to that of the eigenfrequency of the beam. The eigenfrequency of a cantilever beam with the other end being supported by a spring can be given by (Metrikine and Vrouwenvelder, 2018):

$$\omega_n = \frac{n}{2L_{RB}}\sqrt{\frac{k_R}{\rho A_{RB}}} \tag{3.8}$$

where n represents the mode of vibration, with the first eigenfrequency being 80.4 Hz. From the figure above it can be derived that the frequency of these vibrations are at 80 Hz, which is indeed the eigenfrequency of the beam with its current dimensions. The dimensions of the beam, such as the length, area and area moment of inertia, will be altered in the next chapter 4 to investigate the effect and how to mitigate these vibrations.

3.3. Coupled model

The total, coupled model, as depicted in Figure 1.2, is where the preceding models are combined such that the MP and RB interact with one another through the effect of the rollers. In the previous sections the models were individually investigated to gather the information such as assumed correct mesh size and time step in case of the BDF2 solver. In this section, the same methodology is utilized as explained in Appendix A. The outcome of this model is compared to different FEM simulations.

First, to combine the models, coupling terms are to be added to the stiffness matrix of the system. The term w_{MP} in Equation 3.5a is now replaced with w_{RB} which is the radial displacement of the MP at $n = N_{RB}$. A new K-matrix and its state space vector form of the total system can be defined as:

$$K = \begin{bmatrix} K_{uu} & K_{uw} & 0 \\ K_{wu} & K_{ww} & K_{ww,RB} \\ 0 & K_{RB,ww} & K_{RB} \end{bmatrix} \tag{3.9a}$$

$$\begin{bmatrix} \boldsymbol{u} \\ \dot{\boldsymbol{u}} \end{bmatrix} = \begin{bmatrix} u \\ w \\ w_{RB} \\ \dot{u} \\ \dot{w} \\ \dot{w_{RB}} \end{bmatrix} \tag{3.9b}$$

in which $K_{RB,ww}, K_{ww,RB}$ are the coupling matrices which only contain one non-zero entry at $K_{RB,ww}(N_RB, 1)$ and $K_{ww,RB}(1, N_{RB})$, respectively. The subscripts should be interpreted as follows, for example, $K_{RB,ww}$ represents the coupling term of the radial MP displacement (w) within the EOM of the RB. The damping matrix C is computed in a similar manner, but its specific formulation is not provided here.

The maximum diameter MP is used in the base case, meaning that the maximum angle of 81° with respect to the MP is used. In previous sections, the mesh size for both the MP and RB model are established at $\Delta z = 1$ m and $\Delta x = 0.08$ m.

3.3.1. FEM models

Axisymmetric conditions of the coupled model cannot be met in Abaqus when modeling an axisymmetric shell, membrane or solid. Modelling the RB as an axisymmetric beam results in a cone surrounding the MP. This cone-shaped structures does not exhibit behavior similar to a simple beam. It has been shown in subsection 3.1.4 that the $1/8^{th}$ section modelling of the MP demonstrates output as accurate as the other models. Therefore, this model is utilized and expanded by adding the RB model. In the current assumptions for the Matlab model, where the axisymmetric MP is coupled to the 1D RB model, it is assumed that the RB is somewhat axisymmetric. This implies that there are infinitely many RBs in the circumferential direction of the MP, although uncoupled, with all forces translated into the bending of the RB. In the FEM model it has been chosen to model the 3D coupled model with two different methods: (1) a single RB that acts as a point load on each $1/8^{th}$ MP section and (2) a model where on every node in circumferential direction a RB is added to artificially meet the axisymmetric conditions. An illustration of these models are given in Figure 3.17. For a more detailed explanation of these models, refer to Appendix B.

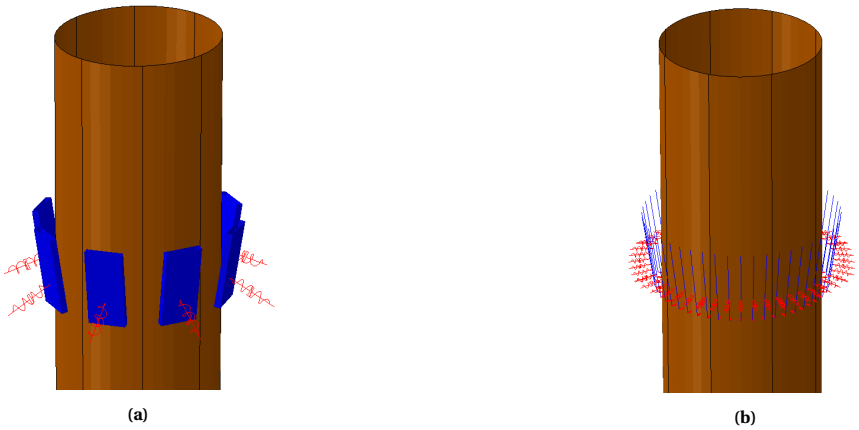

Figure 3.17: Overview of FEM models representing (a) single and (b) axisymmetric RB conditions

3.3.2. Results coupled model

In the MP model it was demonstrated that the radial obstruction by the rollers has a negligible effect on the axial vibrations, which also holds true for this model. In addition, from these 3D images, it can be seen that a similar effect can be spotted in the transverse acceleration as for the RB model.

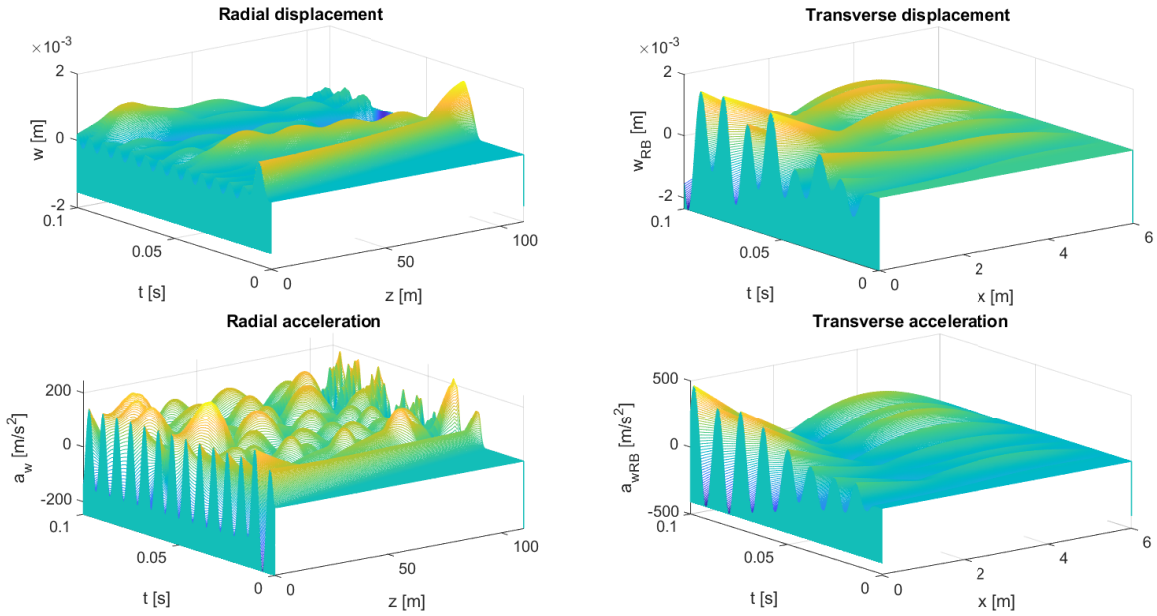

Figure 3.18: Overview of radial and transverse vibrations of MP and RB for the coupled model base case

Considering the first node of the RB once again, it can be shown that the coupled model has the same behavior as the RB model, albeit 2.4% lower in amplitude. This outcome is as expected, given that the MP model demonstrated minimal influence of the rollers on radial displacements. Consequently, the inputs to the roller in both the RB model and coupled model are practically identical. The Matlab model seems to overestimate the maximum displacements and, consequently, the accelerations when compared to the results from FEM simulations. However, as learned from the RB model, it seems that the beam starts vibrating in the frequency of approximately 80 Hz, which is the eigenfrequency of the beam.

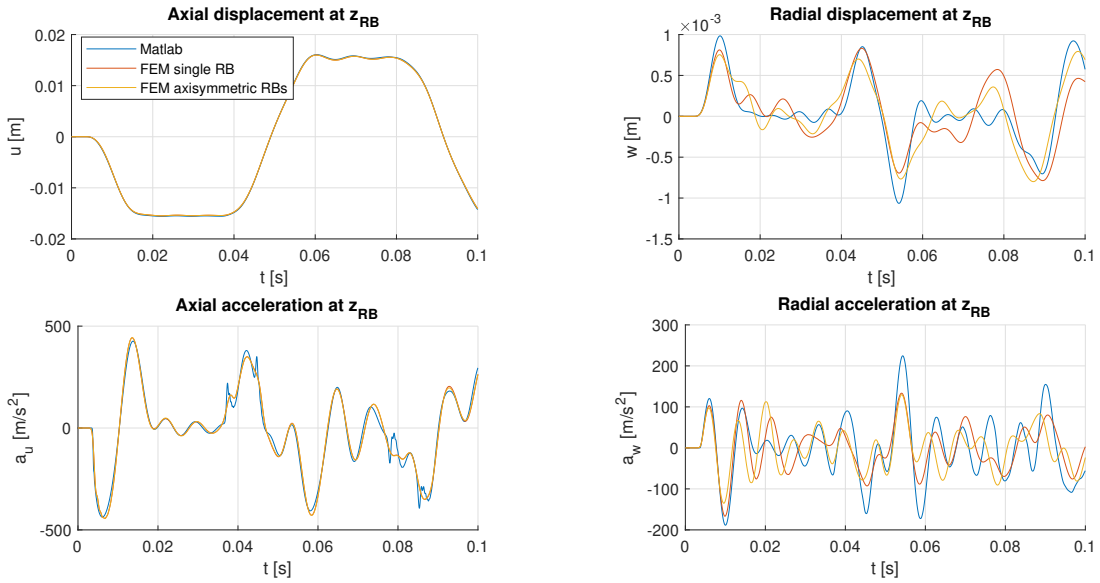

Figure 3.19: The displacements and accelerations of the Matlab FDM coupled model compared to the Abaqus simulations of the base case

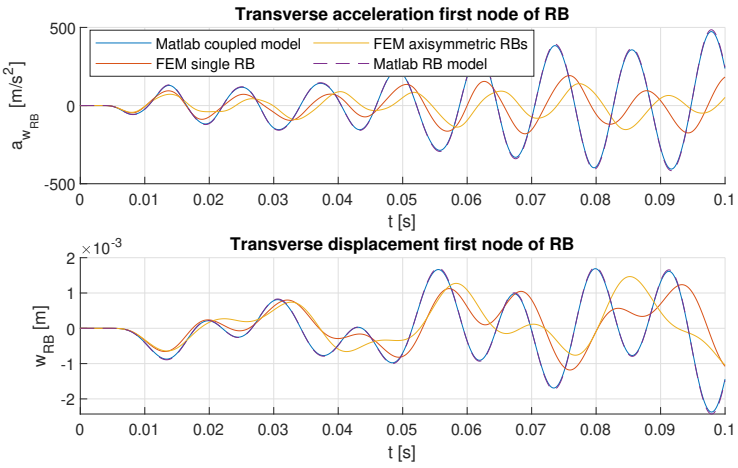

Figure 3.20: The displacements and accelerations of the Matlab FDM coupled model and FDM RB model compared to the Abaqus simulations of the base case

As for this model as well as the RB model, it is hard to draw conclusions as the reflections in the RB become present when $t > 0.037$ s. Therefore, for both the Matlab models and the FEM simulations, the length of the MP is such that the reflections do not appear ($L_{MP} > 271$ m) within the current time frame of 0.1 s. From this simulation it is evident that the eigenfrequency of the beam is not reached, resulting in lower acceleration, which now are only 165 m/s^2.

The single RB and multiple (axisymmetric) RBs FEM simulation models demonstrate a good agreement with one another. This implies that the accelerations within the RB can be effectively modeled by incorporating a single RB into the MP model in FEM to reduce computational time. The slightly higher values calculated in the single RB FEM model, compared to its axisymmetric counterpart, are as expected, given that the overall stiffness is lower when considering a single RB. Moreover, the FDM model in Matlab predicts higher displacements and accelerations than their FEM counterparts. As mentioned previously, the RB is modeled in only one direction in the FDM model, while in FEM, the displacements and accelerations are calculated in every direction, resulting in lower values due to coupling.

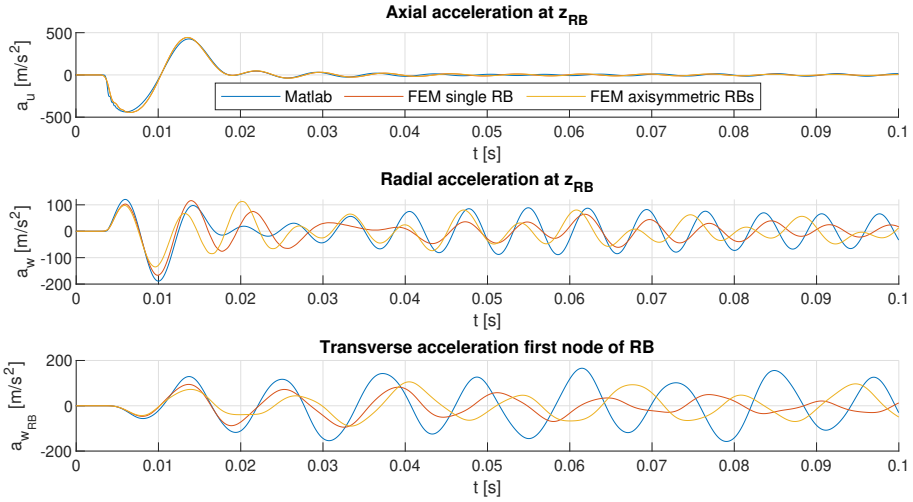

Figure 3.21: Matlab numerical coupled model and RB model versus Abaqus simulations where $L_{MP} > 271$

3.4. Conclusions

In this chapter three consecutive models are extensively studied assessing the vibrations for the base case. Each of these models are validated by means of a FEM simulation. In this section, a brief overview of the most important conclusions are given:

- Both the MP and coupled model demonstrate the breathing of the MP, with the top of the MP vibrating at the ring frequency, resulting in a tail of waves behind the initial waves at this frequency;
- The ode45 solver becomes slow when solving the RB model or coupled model, making BDF2 the preferred solver due to its consistent output compared to the ode45 solver;
- Reflecting waves in the MP causes the RB to resonate at its eigenfrequency. The stiffness of the rollers influences the eigenfrequencies of the RB. Using a length of $L_{MP} > 271$ m eliminates reflected waves within a simulation time of $t = 0.1$ s. Further details about this effect will be discussed in the next chapter;
- A spring stiffness of 200 kN/mm seems to have a negligible effect (<1.4%) on the maximum radial displacement of the MP. The energy of the axial vibrations are dominant for this behavior. When increasing the roller stiffness to $k_R > 1930$ kN/mm, the maximum radial amplitude is reduced by 10%;
- Matlab consistently slightly predicts higher maximum displacements and accelerations of the RB compared to FEM simulations. This is most likely the result of the simplified 1D beam equation, where coupling with transverse and longitudinal vibrations are not considered;
- The RB model exhibits similar output to that of the coupled model, ultimately showing that the beam could be modelled separately without direct coupling to the MP, which reduces the computational time.

4

Parameter sensitivity analysis

This chapter provides a more comprehensive exploration of the roller properties which have been identified as uncertain. In order to assess potential scenarios where a combination of roller properties might result in high accelerations and stresses, further research is essential. Furthermore, the validation of the force input will be discussed to explore the effects of changes in input on the behavior and overall output of the RB.

4.1. Roller properties

Currently, the material specific properties are unknown and ballpark values are given by preliminary calculations. During the model evaluation in the previous chapter, the base case, a spring stiffness of 200 kN/mm is assumed where the damping value is a factor $1e^{-5}$ lower. However, due to the uncertainty of these values it is of high importance to further investigate the effect of the values to the behavior and ultimately maximum accelerations of the rollerbox. The properties of the material are to be experimentally determined. In this section the verified model is used such that combinations of k_R and c_R are implemented and calculated. It is expected that the estimated material properties would be relatively in range of the actual values.

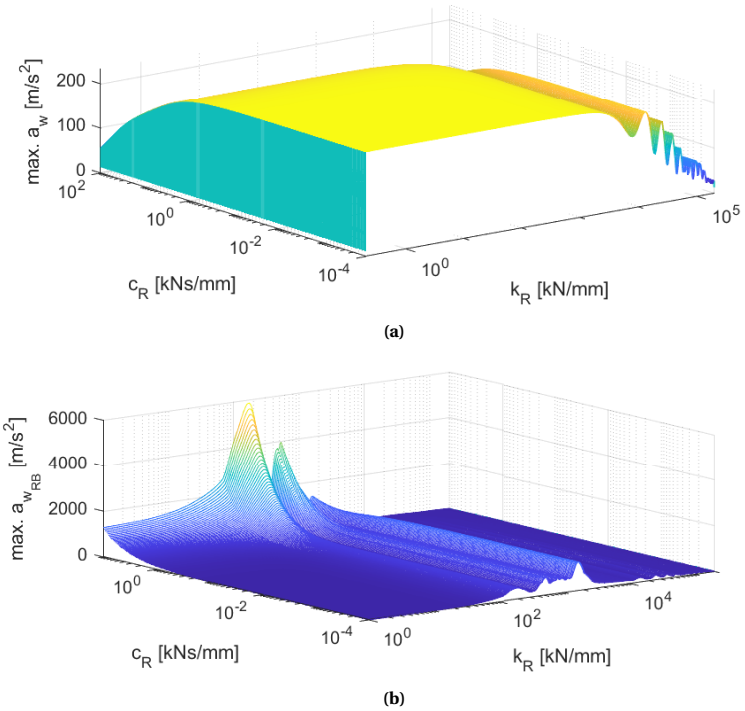

Figure 4.1: Influence of k_R and c_R to the maximum accelerations in radial direction (w) at the RB attachment point and transverse deflection (w_{RB}) of the left end of the rollerbox in a 0.1s time frame

In Figure 4.1, an overview is provided of the maximum accelerations within a 0.1 s time frame computed by the FDM model for different combinations of k_R and c_R. This graph illustrates that very high values for the spring stiffness result in a decrease in radial acceleration of the MP. This behavior is expected, as the beam is a much stiffer object, preventing the MP from expanding in the radial direction. High damping values ($c_R > 1$ kNs/mm) result in an significant increase in the accelerations of the rollerbox. Lower damping values seem to not affect the accelerations of the RB, regardless of the spring stiffness of the rollers. It is currently assumed that the damping value is a factor 10^{-5} lower than k_R. With k_R estimated to be in the order of 200 kN/mm, this implies that the damping coefficient c_R should be in the order of 0.002 kNs/mm. Given that k_R is unlikely to reach a value of $100{\cdot}10^3$ kN/mm, it is assumed that the value of c_R does not significantly alter the accelerations in the RB. Hence, the governing feature for transferring displacement from the MP to the RB is presumed to be the spring stiffness of the roller.

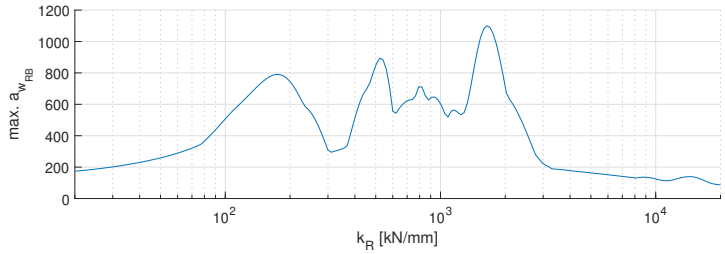

Figure 4.2: Spring stiffness versus the maximum acceleration of the RB for $c_R < 1$ kNs/mm

From Figure 4.2, it is clear that the RB system exhibits high accelerations for a spring stiffness of 1650 kN/mm. The three preceding peaks, to the left of this value, can be observed at accelerations of 790, 890 and 720 m/s^2 corresponding to a spring stiffness of 172, 533 and 807 kN/mm, respectively. Note that these maximum values are observed within a time frame of 0.1 seconds, a deliberate choice to minimize computational time requirements. The vibrations within the MP in radial as well as the axial direction are essentially unaffected by the increased stiffness. In Figure 4.3, it can be seen that these roller stiffness values result in different frequencies when considering the vibrations of the RB especially. It is important to note that the time span of this simulation is set at $t = 1$ s, which means that the maximum acceleration given in the figure above is not fully representative as the vibration have not yet fully developed to its highest amplitude as can be seen in the figure below. Table 4.1 summarises the vibration frequencies for varying spring stiffness that are extracted from the time traces presented in Figure 4.3.

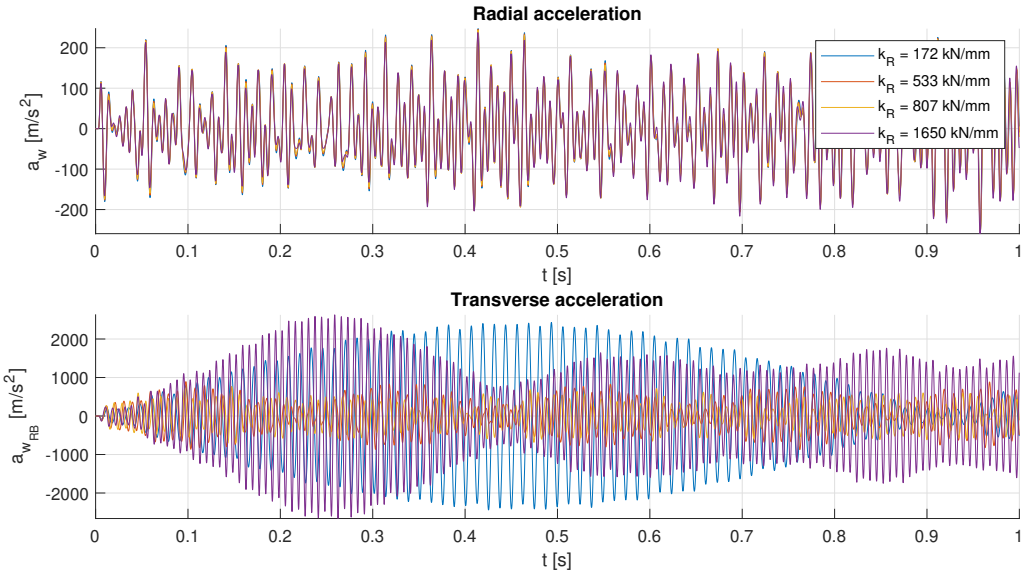

Figure 4.3: Accelerations of the MP at RB height and the first node of the RB for different values for the spring stiffness showing the vibrations within eigenfrequency range of the beam within a time frame of 1s

k_R [kN/mm]	Vibration Freq. [Hz]
172	80
533	100
807	122
1650	139

Table 4.1: Frequencies of transverse vibrations in Figure 4.3

Figure 4.4 illustrates the radial displacement of the MP at the RB height. When considering a pile with a length of 110 m, reflections occur. The frequency spectrum represents the energy density of the frequencies of the radial displacement. In this figure, the peak values of the frequencies in this spectrum correspond to those listed in Table 4.1. The other preceding peak values at frequencies 12, 35, and 58 Hz are part of the propagating wave, although they do not excite the RB to the extent that the RB exhibits excessive vibrations.

When assuming that no reflected waves occur, i.e. $L_{MP} > 259$ m, the radial displacement is continually vibrating at the ring frequency after the initial wave has passed. In contrast to the ring frequency, where the energy density is maintained, the lower frequencies now have a lower energy density.

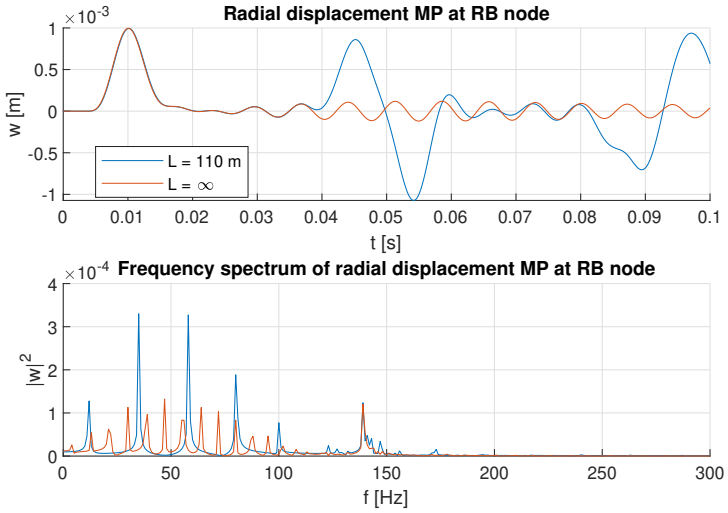

Figure 4.4: Frequency spectrum of radial displacement of the MP

Given that these vibrations exclusively occur for reflected waves, combined with the knowledge from subsection 2.3.2 where it is assumed that the majority of the energy dissipates into the soil and do not reflect, it can be concluded that the RB is primarily excited by the radial frequency within the current time frame. The RB exhibits the most significant interaction with the ring frequency of the MP at a value of $k_R = 1930$ kN/mm, as depicted in Figure 4.5. It is important to note that within the current time frame, the lower frequencies have a higher energy density which decrease when performing the FFT over a longer period of time. Additionally, in case of a simulation of infinite time, the RB will continue to vibrate at its lower eigenfrequencies since these exist in the input force and no damping is considered in the system.

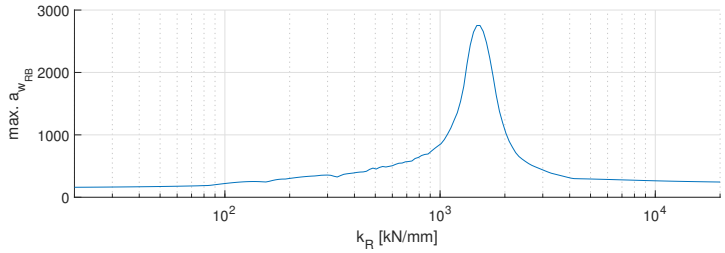

Figure 4.5: Spring stiffness versus the maximum acceleration of the RB for $c_R < 10^6$ Ns/m when $L_{MP} \to \infty$ within a time frame of 1 s

4.1.1. Interaction and stiffness of the systems

It has been shown that the RB is excited at certain frequencies for different spring values of the rollers. In order to gain a better understanding, one could compare the dynamic stiffness of the two coupled systems. First, the dynamic stiffness can be determined by using the following expression, using the K matrix from Equation 3.9a:

$$K_{dyn} = K - M\omega_r^2 \tag{4.1}$$

where, ω are the eigenfrequencies of the system and the M-matrix is an identity matrix. When considering the stiffness of the rollerbox separately, it can be said that the influence of the attached spring results in an intermediate stiffness between that of a hinged-free and hinged-hinged beam, i.e. $k_R = 0$ and $k_R = \infty$, respectively. In Table 4.2 the frequencies of the both the MP and RB are given. Furthermore, the eigenfrequencies of the MP with a length of $L_{MP} = 110$ are given in axial direction. Note that the hydraulic cylinder is present in the RB model which adds stiffness to this system.

	Axial f_u [Hz]	Radial f_w [Hz]	Transverse $f_{w_{RB}}$ [Hz]	
			$k_R = 0$	$k_R = \infty$
ω_1	11.8	139.2	26.6	51.7
ω_2	35.2		69.3	178.6
ω_3	58.2		224.8	360.0
ω_4	80.3			
ω_5	100.1			
ω_6	115.0			
ω_7	123.2			

Table 4.2: Example overview of eigenfrequencies coupled model for a 12.5 m diameter MP of length $L_{MP} = 110$ m

It can be concluded that the axial stiffness of the MP is lower than that of the RB as the resulting eigenfrequencies are lower. However, in the radial direction, the eigenfrequency is higher, indicating that the radial stiffness surpasses the transverse stiffness of the RB. By comparing the eigenmodes of the coupled system, the interaction between the different systems at these frequencies can be shown. In Figure 4.6, it can be seen that at frequencies of 42 and 80 Hz the RB starts vibrating at its natural frequency when $k_R = 200$ kN/mm.

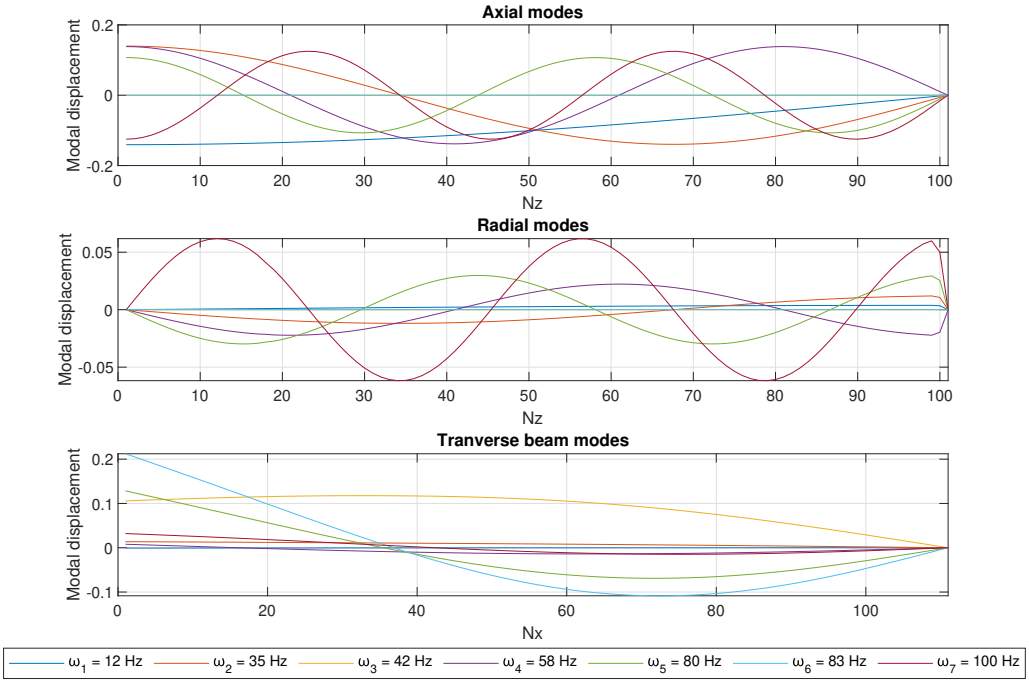

Figure 4.6: First seven eigenmodes of the coupled model for $k_R = 200$ kN/mm

Now, in order to visualize the interaction between the eigenmodes for different values of k_R, the maximum value of these modal amplitude is gathered for each mode. Figure 4.7 shows these maximum amplitudes of these modal shapes. In this graph, the effect of the increasing total dynamic stiffness of the RB is visualized, e.g. the first eigenfrequency ranges from 26.6-51.7 Hz. Furthermore, it can be seen that all the energy in axial direction in the vicinity of the ring frequency fully directs in radial direction. This is explained by the effect of the wave dispersion where the ring frequency is not able to propagate through the MP. In addition, it is demonstrated that some of the axial eigenfrequencies do interfere with that of the RB. Due to current system being numerically approximated, the ring frequency is here showed as a small range of values.

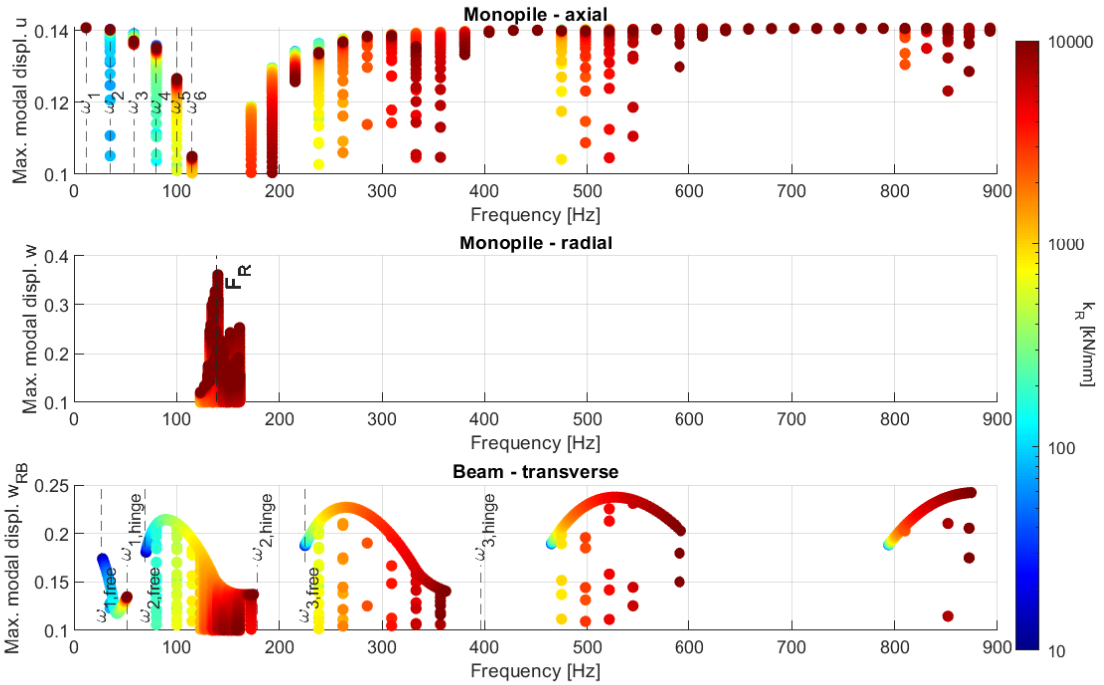

Figure 4.7: A plot of all maximum modal displacements for different values of k_R to illustrate the interaction between a 12.5m MP and the RB

Figure 4.4 and Table 4.1 in the previous section have demonstrated that the hammer impact results in a radial displacement that contains frequencies leading to excessive vibrations of the RB for specific values of k_R. In the figure above, it can be seen that coupling effects between the MP and RB at these frequencies are present. Among these frequencies, it can be noticed that, other than the ring frequency of 139 Hz, all other frequencies represent the coupling with the axial modes of the MP. In the current study, it is assumed that the wave fully reflects on the bottom of the MP; hence, these frequencies would result in excessive vibrations in the RB. In practise, however, with the knowledge that the propagating wave is not fully reflected at the bottom of the MP, the axial resonance is considered to have a minimal influence, as the energy density of these lower frequencies is low, as shown in Figure 4.4.

In the current computations, a 12.5m diameter MP is used whereas the diameter varies per project down to 7 m in diameter. A smaller diameter MP results in a higher ring frequency, which shifts the phenomenon in axial and radial direction in Figure 4.7 to the right. From this data, it can be seen that the second mode of the RB intersect with MP of 9.7-12.5 m, the category of larger diameter MPs. In contrast, the ring frequencies of the smaller MPs fall within the range of the third mode, intersecting with the 7-7.7 m diameter MP category. An overview of these frequency ranges are given in Table 4.3.

Component		Frequency range [Hz]
Eigenfrequency RB	second mode	69 - 178
	third mode	224 - 396
Ring frequency MP	7-7.7 m	224 - 246
	9.7-12.5 m	139 - 178
Input frequency		0 - 300

Table 4.3: Overview frequency ranges of the interacting components and the input force

Under the current assumption that the RB has a uniform cross-section, meaning no stiffeners are present, and without considering the connection material of the BCs and IC, the actual stiffness of the system will deviate from the current values. Consequently, the overlapping eigenfrequency range of the MP with the eigenfrequency of the RB would be altered. However, the behavior of the RB to the roller stiffness as explained in this section remains consistent and should be avoided to prevent excessive vibrations in the system. Incorporating local material details, such as modeling the roller, introduces a higher local mass to the structure, subsequently altering the dynamic stiffness of the RB. This alteration could be advantageous. By introducing local reinforcement or by adjusting the stiffness of the rollers, the eigenfrequency of the RB can intentionally be designed to be further from the ring frequency.

4.2. Force input

This section will elaborate and discuss the origin of the $F(t)$-diagram. In the computations for the base case in chapter 3, a smooth Weibull-diagram is employed, utilizing internal data for a large-diameter MP. Since such large MPs have not yet been installed, this data is sourced from simulations conducted within HMC for calculating the force necessary to drive the pile into the ground.

When referring to impact piling hammers, the input energy is often used. The amount of energy required for pile driving depends on the dimensions of the MP and the soil conditions. As the diameter of the MP increases, the soil shaft resistance also increases. The thickness of the MP does, in terms of shaft resistance, not influence the required input energy. The energy is related to the force-time-diagram by the following relation (Flynn and Mccabe, 2019):

$$E(t) = \int F(t)\, v(t)\, dt \tag{4.2}$$

where $F(t)$ is the force-time-diagram and $v(t)$ is the velocity magnitude at time t after hammer impact. The peak value of the $F(t)$-diagram is depending on the amount of force required for pile driving, i.e. to overcome the shaft and tip resistance of the soil. Intuitively, as the diameter increases, both these resistances increase as the areas related to these resistances increases. The heightened peak force contributes to an increased energy density of the frequencies, although it does not affect the amount of frequencies themselves. In order to achieve a higher maximum input force, the velocity of the hammer is increased, resulting in higher energy.

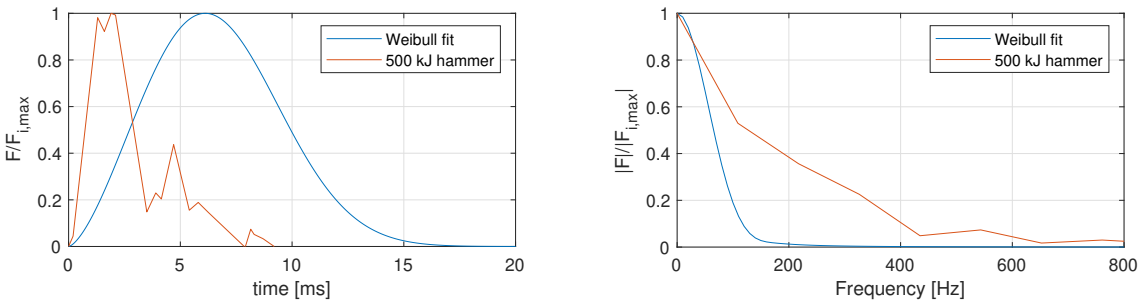

(a) (b)

Figure 4.8: $F(t)$-diagram and corresponding frequency spectrum of different hammers

As illustrated in preceding chapters, the input frequency is of high importance to the behavior of the RB. The Weibull-diagram hammer input is based on predictions for a 5500 kJ hammer for the large-diameter MPs. However, there might be scenarios where a smaller hammer is required, for example, when installing

the small-diameter category. For the sake of comparison, available data from a 500 kJ hammer, measured during a past project, is used. A comparison is made in Figure 4.8, where both hammer forces and their corresponding frequency spectra are normalized for clearer comparison. It is important to note that this hammer is used for pile driving a 1.8 m diameter pile at an energy of 98 kJ, which is 20% of its maximum. This pile is much smaller than the MPs suitable for the MCGF. However, comparing these inputs provides insight into two important factors that will be discussed in this section: the effect of the duration of the impact (Δt) and the additional frequencies when dealing with non-smooth F_t-diagrams.

The value of Δt depends on the size of the hammer. The heavier and larger the hammer, the longer the impulse, leading to a higher Δt and, consequently, lower input frequencies. By combining the understanding of the eigenfrequencies of the RB and these input frequencies, it becomes apparent that larger hammers are preferable over smaller hammers. The use of larger hammers results in a lower energy density at higher frequencies, including the ring frequency, which ultimately drives excessive vibrations.

Throughout this research, a smooth Weibull-shaped impulse is employed, while in practice, this impulse contains higher frequencies. In Figure 4.8, it is illustrated that the hammer exhibits a second peak at approximately 5 ms. This peak occurs due to internal wave reflections within the hammer itself. This additional peak results in a higher energy density at higher frequencies, which is currently overlooked when using the Weibull fit. Since these frequencies fall within the range of the ring frequencies of the MP, it is crucial for future research to employ a more detailed F_t-diagram.

4.3. Conclusions

In this chapter, the impact of roller properties has been examined, revealing that the RB is susceptible to high accelerations when its eigenfrequencies intersect with those of the MP. The interaction between the RB and MP can be differentiated by their interaction with the axial and radial eigenmodes. In the current assumptions of this research, reflections are considered due to the fully reflected waves in an MP of finite length. Hence, excessive vibrations occur for values of k_R = 172, 533 and 807 kN/mm with the axial modes of the MP. Future research should focus on these reflected waves, as part of these vibrations reflects, whereas the majority dissipates into the soil.

It has been discussed that vibrations in the RB are primarily vulnerable to the interaction with the ring frequency of the MP. Figure 4.9 summarizes that the small diameter MP category is within range of the eigenfrequency of the RB for values in the vicinity of k_R = 200 kN/mm. In practice, the eigenfrequency range of the RB may vary from the values calculated in this research. Factors such as stiffeners or the added mass due to the roller mechanism can modify the stiffness of the RB, either increasing or decreasing its eigenfrequencies. Design considerations could include configuring the RB in a manner that ensures the third eigenfrequency range does not intersect with the ring frequency region of the MPs.

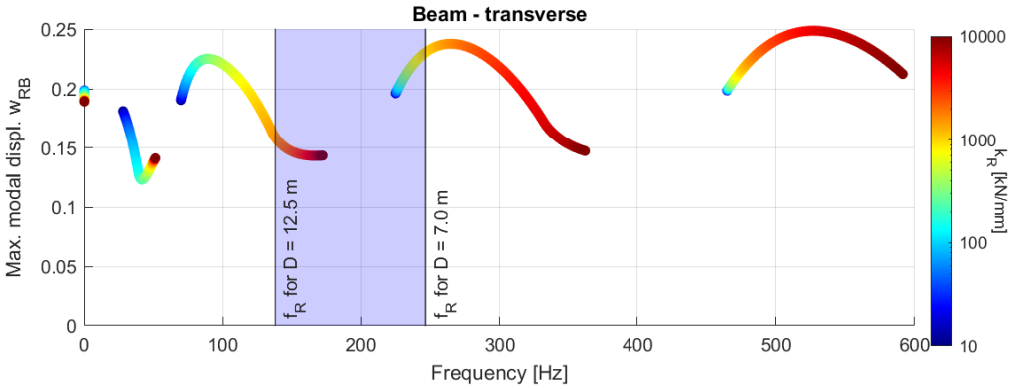

Figure 4.9: Eigenfrequencies of the RB with simplified dimensions versus the roller stiffness compared to the region of ring frequencies of 7-12.5m diameter MPs

5

Measuring

In this chapter, the focus will be put on using the model to retrieve the stresses in the RB. Using this, a comparison can be made with the current method of determining the stresses in the beam. During the calculations of the accelerations within the RB, the assumptions was made where the prestress could be neglected when considering the dynamic behavior of the system. However, in order to get the stresses in the beam, the prestress will be taken into account as the position of the maximum stress is depending on both the dynamic behavior and the prestress combined. During these calculations, the accelerations used for the stress calculations are based on the interaction between the MP and the RB, with a spring stiffness for the roller of k_R = 200 kN/mm. In addition, due to the assumption that most of the energy will dissipate into the soil resulting the RB to not be excited within the range of its eigenfrequencies. The prestress ranges from 0-250 tonnes, depending of the positioning of the MP.

5.1. Static beam mechanics

The industry practice of calculating the stresses is by using beam statics to determine the stresses throughout the RB. An extra acceleration is applied to the structure, which results in an added stress in the beam. This acceleration is considered as a distributed force over the length of the beam. In this paragraph, this method will be evaluated and compared by using the knowledge gained from previous chapters where the acceleration along the length is determined using the interaction between the MP and RB.

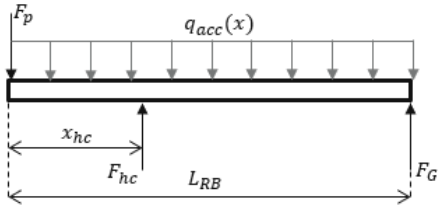

Figure 5.1: FBD of the RB including a distributed load representing the added acceleration

In order to calculate the stresses in the beam, the resulting vertical forces of the hydraulic cylinder (F_{hc}) and the gripper ring (F_G) are required. Beam mechanics are used as depicted in Figure 5.1 to set up the balance of forces ($\sum F = 0$) and moments ($\sum M_G = 0$) within the beam the forces read:

$$F_{hc} = \frac{LF_p + \frac{L}{2}F_{acc}(x)}{L - x_{hc}} \tag{5.1a}$$

$$F_G = F_p + F_{acc}(x) - F_{hc} \tag{5.1b}$$

where F_{acc} is determined by $F_{acc} = \Delta x q_{acc}(x) = \Delta x \rho A_{RB} a_{w_{RB}}(x)$. In Figure 5.2, an overview of the applied constant acceleration of 100 m/s^2 is demonstrated in blue next to the accelerations throughout the RB determined by the FDM model in orange. In reality, the accelerations throughout the RB would resemble the

acceleration distribution of the FDM model, as depicted in Figure 3.15. With the calculated forces, the stresses can be calculated by:

$$\sigma_b(x) = -\frac{c_{RB}M(x)}{I_{RB}} = -\frac{c_{RB}}{I_{RB}}\frac{\partial^2 w_{RB}}{\partial x^2} \tag{5.2}$$

where c_{RB} represents distance from the neutral axis to the outer fiber of the cross section of the RB. In contrast to the industry practice, with the current FDM model, the stresses can be determined directly from the dynamic simulation. It is important to note that the resulting forces F_{hc} and F_G strongly depend on the prestress (F_P) and the angle of the RB (α). The highest stresses occur when dealing with the largest diameter MPs of 12.5 m when the angle of the RB is at 81° combined with a prestress of 250 tonnes.

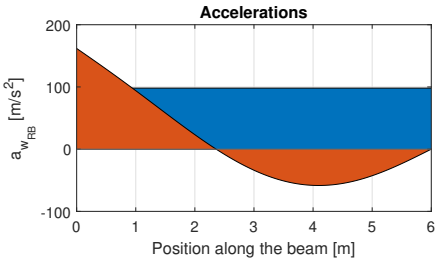

Figure 5.2: The applied even (blue) and uneven (orange) distributed accelerations over the length of the RB

Using these accelerations as input, the shear and moment diagrams over the length of the RB can be plotted. The maximum bending moment occurs at the attachment point of the hydraulic cylinder, which is expected as the hydraulic cylinder bears the highest load.

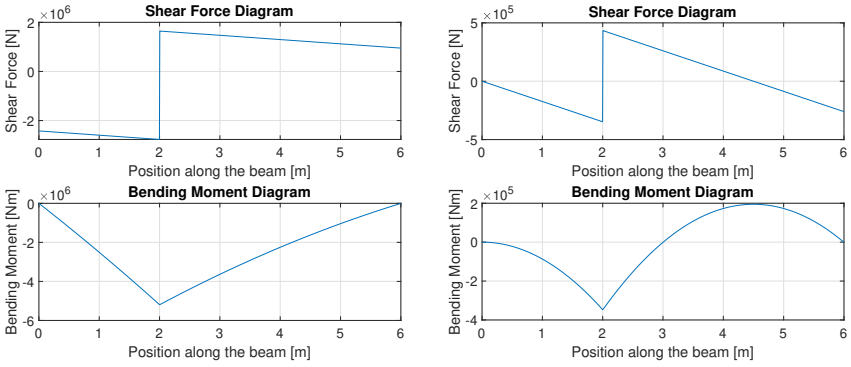

(a) Maximum prestress + added acceleration

(b) Contribution of added acceleration

Figure 5.3: The shear and moment diagrams of the RB for the static distributed acceleration load

The dynamic stresses can be obtained from the coupled model, as illustrated in the figure below. Similarly to the static method, the highest stresses are located at the attachment of the hydraulic cylinder. An important disparity between the two methods lies in the dynamic aspect of the hydraulic cylinder, where the force increases as the spring is being compressed. In contrast, the static part assumes that the hydraulic cylinder is a rigid point, effectively functioning as a hinge, ultimately resulting in higher stresses.

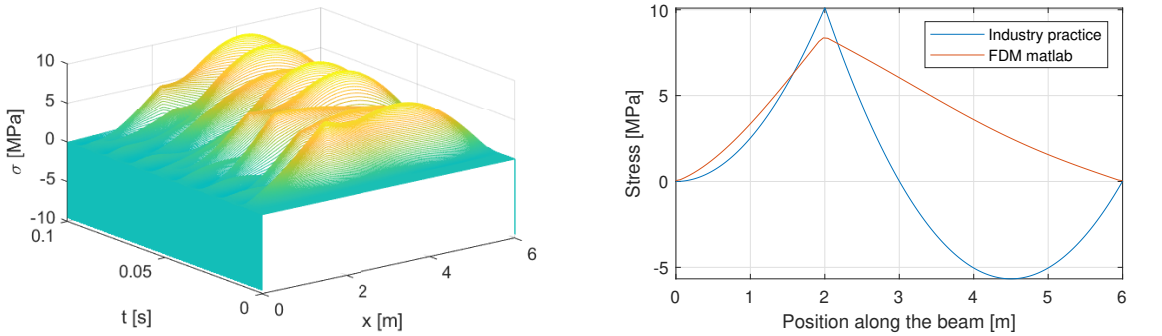

(a) 3D image of stresses along the length of the RB over time

(b) Scenario of maximum resulting stresses along the length of the RB

Figure 5.4: Stresses obtained from the FDM model compared to the static stresses in the beam

	Prestress [MPa]	Acceleration [MPa]	Total stress [MPa]	Part of total stress [%]
Static	141.0	10.1	151.1	7%
Dynamic	141.0	8.1	149.1	5%

Table 5.1: Contribution of the prestress and acceleration to the total stress in the RB

Although the dynamic case introduces extra stresses from vibrations within the RB, the overall contribution to the total stress is minimal. It is crucial to note that this is valid for a scenario where no resonance occurs and the maximum accelerations remain relatively low at the MP end of the RB (160 m/s^2). In this comparison, both methods contain uncertainty regarding the maximum stress due to the transverse and axial stresses being neglected and assuming that all forces translate into bending of the beam. Both the angle of the hydraulic cylinder and the angle of the RB with respect to the MP cause an axial force within the beam. These stresses are likely to increase the total stress in the system. However, it can be assumed that the added stresses due to the vibrations will remain low relative to those of the prestress.

Furthermore, while the added stresses do not significantly increase the static stresses, they might play a more prominent role in determining the lifetime of the RB due to fatigue damage. An estimate of the number of cycles can be provided by assuming each blow of the hammer dampens out after, for instance, 2 seconds. The radial expansion of the MP would vibrate at the ring frequency of 139-246 Hz, implying that 278-492 cycles are expected at the RB per blow. Each installed MP could endure thousands of blows for the entire pile to be driven into the ground. Although these stresses are low compared to the prestress, they might become a more significant factor for fatigue damage in the structure. Since this aspect has not been explored in this research, it could be an important topic for future investigations where the value of k_R and the damping of these vibrations should be taken into consideration.

6

Conclusions and recommendations

The main objective of this report is to describe and quantify the behavior of vibrations on a MCGF due to pile driving. The research is based on several fundamental elements:

1. Literature study
2. Numerical model validation
3. Parameter study

These elements are thoroughly discussed to address the main research question of this thesis:

What is the effect of the vibrations on a MCGF caused by driving XXL monopiles?

6.1. Conclusions

At the starting phase of this research a literature study is performed in chapter 2 where the 3D wave equations are derived for a cylindrical membrane shell. Axisymmetric conditions are assumed which includes that hammer impact on the top of the MP is perfectly vertical. In addition, no imperfections in tangential direction allows to assume that all terms containing $\frac{\partial}{\partial\theta} = 0$. This assumption majorly simplifies the EOM turning the 3D wave equations into a 2D, axisymmetric system of PDEs. Two solving methods are described: implicit (BDF2) and explicit (ode45).

The PU rollers have hyper-viscoelastic properties and is a rubber-like polymer. The visco-elastic and hyperelastic material properties are separately treated, describing the effect of temperature and frequency to the moduli (stiffness) and damping of the material. In case of high frequency loads, such as vibrations in the MP and MCGF, material stiffness increases, behaving similarly to a rigid glass. In order to obtain accurate properties for this material, experiments are to be performed on a test specimen within the expected frequency range up to 200-300 Hz. In this thesis, the influence of the roller material is linearized. Implementing non-linear effects can be more complex and may not necessarily provide a more accurate understanding of the actual behavior. In fact, it could potentially lead to under- or overestimation of vibrations in the system.

In chapter 3, three models were introduced to identify the effects of the rollers to the MP and RB separately, ultimately combining these models to study the interaction of these models. During the validation process, a base case was considered with a spring stiffness of k_R = 200 kN/mm and a 12.5m diameter MP. In these models, water and soil conditions are not considered which result in a full reflected wave on the bottom of the MP.

It has been found that the presence of the rollers reduce the amplitude by 1.4% when considering the base case. A reduction of 10% is reached when the rollers take a value of 1930 kN/mm. The axial displacement however, is not influenced (<<1%) which is expected as most of the energy propagates in axial direction.

For the RB model the numerical Matlab model shows similarities in behavior as its FEM counterpart. However, the FEM model predicts a lower amplitude than the Matlab model. This disparity can be attributed to the fact that the Matlab model, based on the Euler-Lagrange beam equation, is a 1D system. In such a system, all energy is directed toward bending the beam. In contrast, the FEM model accommodates axial and lateral vibrations, resulting in lower accelerations and displacements.

The third model, the coupled model, exhibits similar behavior as the RB model with sinusoidal vibrations in the RB displaying an increase in amplitudes over time. A more in-depth exploration of this phenomenon is presented in chapter 4. Importantly, all numerical models demonstrate a good agreement with their FEM model.

In chapter 4, a more comprehensive study is performed on the effect of the rollers. Here it has been shown that the damping of the material starts to play a role when reaching the range of c_R>1 MNs/m, allowing to neglect the effects of the damping for further calculations. In addition, it has showed that due to the undamped vibrations, the RB will start to vibrate in its eigenfrequency as these frequencies will always be present in the propagating wave, albeit of low energy density.

In the current simulations, a simplified Weibull-fitted curve is used to represent the hammer impact force on the MP, where frequencies up to 200 Hz occur. However, in practice this impulse is not as smooth as a Weibull-fit. Hammer reflections induce higher frequencies, thereby increasing the energy density within these frequency ranges. In addition, smaller diameter MPs might utilize smaller hammer, ultimately resulting in the frequency range up to 300 Hz to become more prominently involved in the system as the impulse is shorter.

The dynamic stiffnesses of the systems are considered in order to examine the interaction between their modal shapes. It has been demonstrated that frequencies in the vicinity of the ring frequency excite the 2$^{\text{nd}}$ or 3$^{\text{rd}}$ eigenfrequency of the RB, of which the latter is depending on value of k_R. When the stiffness of the spring increased, so do the eigenfrequencies of the RB. It was found that for large diameter MPs in combination with high values of k_R>1650 kN/mm results in the RB to vibrate in its eigenfrequency. In contrast, for small diameter MPs it has been found that for values close to the expected k_R of 200 kN/mm, the RB will start vibrating in its eigenfrequency. Considering the input frequencies, it can be concluded that excessive vibrations within MCGF are most susceptible for the smaller diameter MPs category.

Lastly, the industry practice of calculating the stresses in the beam are compared to the stresses that are gathered from the numerical model. Currently, stresses in structures such as the RB are determined by a superposition of the acceleration of the entire system and the static prestress. This load is an evenly distributed load of 100 m/s^2 (≈10g). However, it is shown that, in reality, the accelerations within the RB are non-uniformly distributed. Moreover, the acceleration at the free end is higher ($a_{w_{RB}}$=160 m/s^2). It has been illustrated that the prestress results in a maximum static stress of 141.0 MPa at the position of the hydraulic cylinder. This static stress is the highest for the largest diameter MP as the RB angle is 81°.

Stresses attributed to the added acceleration indicate that the numerical model produces a stress of 8.1 MPa at the hydraulic cylinder position, representing a 19% reduction compared to stresses calculated using the conventional method. This suggests that the industry practice might overestimate these stresses. However, considering that the this superposition of the accelerations only accounts for 7% of the total stress in the beam, these stresses could be neglected.

6.2. Recommendations

In this study, the rollers appear to exert a substantial influence on the behavior of the vibrations in the MCGF. Due to uncertainties regarding the material properties of the PU material are estimated for the base case and the stress calculations. For more accurate predictions concerning the vibrations, it is essential to determine these properties through experimental methods.

Furthermore, in order to include the nonlinearity of the material, several hyperelastic models are listed which are based on the principle of Helmholtz free energy. Depending on the complexity of the model, the more material properties are required. In case of a model where two properties are required, such as the Neo-Hookean model, the shear and bulk modulus are used in order to compute the material specific nonlinear stress-strain relation. Furthermore, the effect of compression of the PU rollers is neglected in the current model. Compressed material, due to its nonlinearities, could show different behavior and result in a higher or lower spring stiffness.

The damping properties of the roller are estimated using the assumption that the damping value is simply calculated by $c_R = k_R \cdot 10^{-5}$. While this value is presumed to have low influence, higher values exceeding $c_R > 1$ kNs/mm result in high accelerations in the system. This research did not include further investigation into whether this behavior is the result of numerical instability or if the dashpot is acting like a spring. In either case, this behavior might lead to high stresses in the system due to these elevated accelerations.

The presence of reflected waves affects the frequencies that induce vibrations in the MCGF. In further study, the effect of the water and soil conditions regarding their damping should be considered. Energy losses will occur due to these factors. More importantly, the majority of the energy will be directed into the ground to facilitate the driving of the pile into the soil, which remains the primary objective of the entire process. A higher reflections energy density is expected when pile refusal occurs, often happening as the MP embeds deeper into the ground. However, beyond a certain embedment depth, dependent on the MP diameter, the pile is considered stable enough, and the MCGF is no longer needed.

Axisymmetry is assumed when deriving the EoMs, resulting in the circumferential mode consistently being 0. However, in practice, due to non-verticality of the force or other imperfections within the system could introduce these circumferential modes. This mode might have certain frequencies in the range of that of the beam, which ultimately could cause higher accelerations in the RB. Unfortunately, the current model lacks the capacity to describe this phenomenon. To incorporate it, the circumferential mode should be expanded, making the spatial derivatives of the central difference method more complicated.

All calculations conducted in this thesis are based on the Weibull-fit of a 12.5 m diameter MP. These large diameter MPs require newly build hammers for which data is currently unavailable. It has been demonstrated that the hammer input is a significant factor in determining the vibrations and stresses in the MCGF. Moreover, smaller diameter MPs (7-7.7 m) might be subjected to smaller hammers, therefore having a distinct F(t)-diagram with higher energy density toward higher frequencies. For these MPs it has been illustrated that lower values of k_R could lead to the RB having an eigenfrequency close or equal to the ring frequency.

When considering the stresses in the beam it was demonstrated that the added acceleration is a small portion of the total stress. However, it is essential to note that the current model assumes a constant cross-sectional area for the RB along its length. In reality, the roller at the end of the beam introduces a local added mass, particularly where the highest accelerations occur. This local added mass could potentially result in higher stresses.

The beam stiffness in this research is based on a constant cross-section, but in reality, the attachment pin of the hydraulic cylinder and the mechanical parts of the roller can alter the stiffness of the system. Particularly, the roller mechanism, with its locally higher mass, tends to lower the stiffness of the RB. Modifying the RB by introducing local reinforcement, for example, could prevent the eigenfrequency of the RB from intersecting with the ring frequency region.

Additionally, the stiffness of the hydraulic cylinder influences the dynamic stiffness of the RB. With the current assumptions, the minimum value of k_{hc} = 223 kN/mm is employed in the model. However, this is the minimum value this spring could have. In reality, when the RB has a large-diameter MP inside the gripper, the hydraulic cylinders are almost fully retracted, resulting in a higher stiffness. Similar to the roller stiffness, a higher hydraulic stiffness would lead to a stiffer beam, ultimately resulting in higher eigenfrequencies.

References

Argyroulis, K. (2022). Performance of steel open ended pile driveability prediction methods in dense sand: Evaluating pile driveability models and improving driveability predictions of a recent static axial capacity approach.

Bergström, J. (2015). Mechanics of Solid Polymers: Theory and Computational Modeling. *Mechanics of Solid Polymers: Theory and Computational Modeling*, pages 1–509.

Brinson, H. F. and Brinson, L. C. (2015). Nonlinear Viscoelasticity. *Polymer Engineering Science and Viscoelasticity*, pages 339–377.

BVG Associates (2019). Guide to an offshore wind farm Updated and extended Published on behalf of The Crown Estate and the Offshore Renewable Energy Catapult The Crown Estate Offshore Renewable Energy Catapult.

Celaya, E. A., Aguirrezabala, J. J., and Chatzipantelidis, P. (2014). Implementation of an Adaptive BDF2 Formula and Comparison with the MATLAB Ode15s. *Procedia Computer Science*, 29:1014–1026.

Flügge, W. (1960). Bending of Circular Cylindrical Shells. *Stresses in Shells*, pages 208–312.

Flynn, K. N. and Mccabe, B. A. (2019). Driven cast-in-situ piles installed using hydraulic hammers: Installation energy transfer and driveability assessment.

Gent, A. N. and Scott, K. W. (2012). Dynamic Mechanical Properties. *Engineering with Rubber*, pages 89–118.

Graff, K. F. (1975). *Wave Motion in Elastic Solids*. Oxford University Press, London, first edition.

Groenewoud, W. (2001). *Characterisation of Polymers by Thermal Analysis*. Elsevier Science B.V., second edition.

Hairer, E. and Wanner, G. (1996). *Solving Ordinary Differential Equations II: Stiff and Differential-Algebraic Problems*. Springer series in computational mathematics. Springer-Verlag, second edition.

Hairer, E. and Wanner, G. (2000). *Solving Ordinary Differential Equations I: Nonstiff Problems*. Springer series in computational mathematics. Springer-Verlag, second edition.

Hajikarimi, P. and Nejad, F. M. (2021). *Applications of Viscoelasticity: Bituminous Materials Characterization and Modeling*. Elsevier.

Hutchinson, M. and Zhao, F. (2023). Global Wind Report 2023.

ISO 7743:2011(E) (2011). Rubber, vulcanized or thermoplastic Determination of compression stress-strain properties. Standard, International Organization for Standardization, Geneva, CH.

Kaplunov, J., Kossovich, L., and Nolde, E. (1998). *Dynamics of Thin Walled Elastic Bodies*. Academic Press.

Khalil, M. K. B. (2009). Interactive Analysis of Closed Loop Electro-hydraulic Control Systems. *International Conference on Aerospace Sciences and Aviation Technology*, 13(AEROSPACE SCIENCES & AVIATION TECHNOLOGY, ASAT- 13, May 26 28, 2009):1–10.

Leissa, A. W. (1973). Vibration of Shells.

MacGillivray, A. (2015). Finite difference computational modelling of marine impact pile driving. *Euronoise 2015*, pages 623–628.

Marsick, A., Shankar Sharma, G., Eggler, D., Maxit, L., Meyer, V., and Kessissoglou, N. (2021). On the vibroacoustic response of a cylindrical shell submerged near a free sea surface. *Journal of Sound and Vibration*, 511:116359.

Meijers, P. (2021). Non-collocated methods to infer deformation in steel structures: The magnetomechanical effect in cylindrical structures subjected to impact loads.

Metrikine, A. V. and Vrouwenvelder, A. C. W. M. (2018). Dynamics of Structures - CT4140 Part 2 Wave Dynamics. Technical report.

Parola, J. F. (1970). *Mechanics of Impact Pile Driving*. PhD thesis, University of Illinois, Illinois.

PerkinElmer Inc (2013). Dynamic Mechanical Analysis (DMA) A Beginner's Guide. Technical report.

Qi, H. J. and Boyce, M. C. (2005). Stressstrain behavior of thermoplastic polyurethanes. *Mechanics of Materials*, 37(8):817–839.

Ramli, H., Zainal, N. F. A., Hess, M., and Chan, C. H. (2022). Basic principle and good practices of rheology for polymers for teachers and beginners. *Chemistry Teacher International*, 4(4):307–326.

Rausche, F., Liang, L., Allin, R. C., and Rancman, D. (2004). Applications And Correlations Of The Wave Equation Analysis Program GRLWEAP.

Reyff, J. (2012). Underwater sounds from unattenuated and attenuated marine pile driving. *Advances in experimental medicine and biology*, 730:439–444.

Shampine, L. F. (1986). Some Practical Runge-Kutta Formulas. *Mathematics of Computation*, 46(173):135.

Shampine, L. F., Reichelt, M. W., and Sci Comput, S. J. (1997). THE MATLAB ODE SUITE *. *Society for Industrial and Applied Mathematics*, 18(1):1–22.

Smith, E. A. L. (1962). Pile-driving analysys by the wave equation. *Journal of the Soil Mechanics and Foundation Division*, 127(1):26.

Somarathna, H. M., Raman, S. N., Mohotti, D., Mutalib, A. A., and Badri, K. H. (2020). Hyper-viscoelastic constitutive models for predicting the material behavior of polyurethane under varying strain rates and uniaxial tensile loading. *Construction and Building Materials*, 236:117417.

Süli, E. and Mayers, D. F. (2003). *An Introduction to Numerical Analysis*. Cambridge University Press, New York.

Tsetas, A. (2023). A unified modelling framework for vibratory pile driving methods.

Tsouvalas, A. and Metrikine, A. V. (2014). A three-dimensional vibroacoustic model for the prediction of underwater noise from offshore pile driving. *Journal of Sound and Vibration*, 333(8):2283–2311.

Ucar, H. and Basdogan, I. (2018). Dynamic characterization and modeling of rubber shock absorbers: A comprehensive case study. *Journal of Low Frequency Noise, Vibrations and Acrtive Control*, 37(3):509–518.

Vuik, K., Vermolen, F., Gijzen, M. v., and Vuik, T. (2023). Numerical Methods for Ordinary Differential Equations. *TU Delft OPEN Textbooks*.

Wang, J., Sun, D., Liu, S., and Zhang, X. (2017). Damping Characteristics of Viscoelastic Damping Structure under Coupled Condition. *Mathematical and Computational Applications 2017, Vol. 22, Page 27*, 22(1):27.

Zwartveld, J. (2016). Structural vibrations induced by pile driving.

A

Applying the finite difference method

In this appendix an extensive overview is given on how to use the finite difference method (FDM). The 3D vibrations theory, derived in chapter 2, is used to describe the vibrations of a cylindrical shell in axial and radial direction. In this appendix it is shown how the PDE is transformed into a ODE by using spatial derivative approximations, which is numerically solvable for MATLAB in this form. This method offers a straightforward method to incorporate boundary conditions (BC) and interface conditions (IC) to the ODE.
First, the model is split into N amount of nodes with $N-1$ amount of elements along the length of the object, in this case the MP. Note that the upcoming section only includes the MP model and do not include the beam, thus coupled model. In this appendix, a generalisation of MP model is given where:

$$\boldsymbol{u} = \begin{bmatrix} u & w \end{bmatrix}^T \tag{A.1}$$

Now, the spatial derivative approximation of the central difference can be given by:

$$\frac{\partial \boldsymbol{u}}{\partial z} \approx \frac{-\boldsymbol{u}(z-h)+\boldsymbol{u}(z+h)}{2h} \tag{A.2a}$$

$$\frac{\partial^2 \boldsymbol{u}}{\partial z^2} \approx \frac{\boldsymbol{u}(z-h)-2\boldsymbol{u}(z)+\boldsymbol{u}(z+h)}{h^2} \tag{A.2b}$$

$$\frac{\partial^3 \boldsymbol{u}}{\partial z^3} \approx \frac{-\boldsymbol{u}(z-2h)+2\boldsymbol{u}(z-h)-2\boldsymbol{u}(z+h)+\boldsymbol{u}(z+2h)}{2h^3} \tag{A.2c}$$

$$\frac{\partial^4 \boldsymbol{u}}{\partial z^4} \approx \frac{\boldsymbol{u}(z-2h)-4\boldsymbol{u}(z-h)+6\boldsymbol{u}(z)-4\boldsymbol{u}(z+h)+\boldsymbol{u}(z+2h)}{h^4} \tag{A.2d}$$

in which h is the mesh size.

Using the spatial derivatives, the EOMs, given in Equation 2.15, can be rewritten in their discretized form:

$$\sum_{n=1}^{N} \left\{ \frac{\partial^2 u_n}{\partial t^2} + \frac{c_p^2}{\Delta z^2}\left(-u_{n-1}+2u_n-u_{n+1}\right) + \frac{c_p^2 \nu}{2\Delta z\, R}\left(w_{n-1}-w_{n+1}\right) \right\} = 0 \tag{A.3a}$$

$$\sum_{n=1}^{N} \left\{ \frac{\partial^2 w_n}{\partial t^2} + \frac{c_p^2}{R^2} w_n + \frac{\nu c_p^2}{2\Delta z\, R}\left(-u_{n-1}+u_{n+1}\right) + \frac{c_p^2\, h_{MP}^2}{12\Delta z^4}\left(w_{n-2}-4w_{n-1}+6w_n-4w_{n+1}+w_{n+2}\right) \right\} = 0 \tag{A.3b}$$

A.1. Solving ordinary differential equations

The current state of the equations of motion is in the second order time derivative. In order to solve these equations with the MATLAB solvers, the equations have to be written in state space form to isolate the second order time derivatives. First, the system of equations can be written in the following form:

$$M\ddot{\boldsymbol{u}} + C\dot{\boldsymbol{u}} + K\boldsymbol{u} = 0 \tag{A.4}$$

in which $\boldsymbol{u}$ represents the vector containing all the u and w per node within the domain $n \in [1, N]$. M, C and K are $2N \times 2N$ matrices and respectively the mass, damping and stiffness matrix of the system. The matrices consist out of:

$$M = \begin{pmatrix} 1 & & 0 \\ & \ddots & \\ 0 & & 1 \end{pmatrix} \tag{A.5a}$$

$$C = \begin{pmatrix} 0 & \cdots & 0 \\ \vdots & \ddots & \vdots \\ 0 & \cdots & 0 \end{pmatrix} \tag{A.5b}$$

$$K = \begin{pmatrix} K_{uu} & K_{uw} \\ K_{wu} & K_{ww} \end{pmatrix} \tag{A.5c}$$

in which K_{uu}, K_{uw}, K_{wu} and K_{ww} are the stiffness matrices of size $N \times N$ where K_{uu} are the stiffness coupling terms of u with respect to u in the time domain, K_{uw} are the stiffness coupling terms of w with respect to u in the time domain. Same as for K_{wu} and K_{ww} but for the time domain of w.

The matrix for C is full equal to zero. However, in future steps when ICs are included, this matrix will become non-zero. For computational purposes, the matrix will be displayed in its current form. The K-matrices can be defined from Equation A.3 such that:

$$K_{uu} = \begin{pmatrix} k_{u,1} & k_{u,2} & 0 & \cdots & 0 \\ k_{u,2} & k_{u,1} & k_{u,2} & 0 & \vdots \\ 0 & \ddots & \ddots & \ddots & 0 \\ \vdots & 0 & k_{u,2} & k_{u,1} & k_{u,2} \\ 0 & \cdots & 0 & k_{u,2} & k_{u,1} \end{pmatrix} \tag{A.6a}$$

$$K_{uw} = \begin{pmatrix} 0 & -k_{uw} & 0 & \cdots & 0 \\ k_{uw} & 0 & -k_{uw} & 0 & \vdots \\ 0 & \ddots & \ddots & \ddots & 0 \\ \vdots & 0 & k_{uw} & 0 & -k_{uw} \\ 0 & \cdots & 0 & k_{uw} & 0 \end{pmatrix} \tag{A.6b}$$

$$K_{wu} = \begin{pmatrix} 0 & k_{wu} & 0 & \cdots & 0 \\ -k_{wu} & 0 & k_{wu} & 0 & \vdots \\ 0 & \ddots & \ddots & \ddots & 0 \\ \vdots & 0 & -k_{wu} & 0 & k_{wu} \\ 0 & \cdots & 0 & -k_{wu} & 0 \end{pmatrix} \tag{A.6c}$$

$$K_{ww} = \begin{pmatrix} k_{w,1} & k_{w,2} & k_{w,3} & 0 & \cdots & 0 \\ k_{w,2} & k_{w,1} & k_{w,2} & k_{w,3} & 0 & \vdots \\ 0 & \ddots & \ddots & \ddots & \ddots & 0 \\ \vdots & 0 & k_{w,3} & k_{w,2} & k_{w,1} & k_{w,2} \\ 0 & \cdots & 0 & k_{w,3} & k_{w,2} & k_{w,1} \end{pmatrix} \tag{A.6d}$$

Note that $K_{uw} = -K_{wu}$.

The acceleration term $\ddot{\boldsymbol{u}}$ can be isolated such that the following equality holds:

$$\ddot{\boldsymbol{u}} = -M^{-1}\left(C\dot{\boldsymbol{u}} + K\boldsymbol{u}\right) \tag{A.7}$$

The final step which is required for the MATLAB solvers is to rewrite these equation into their state space form, which can be denoted as:

$$\begin{bmatrix}\dot{\boldsymbol{u}}\\ \ddot{\boldsymbol{u}}\end{bmatrix} = \begin{pmatrix}0 & 1\\ -M^{-1}K & -M^{-1}C\end{pmatrix}\begin{bmatrix}\boldsymbol{u}\\ \dot{\boldsymbol{u}}\end{bmatrix} \tag{A.8}$$

A.2. Implementing boundary and interface conditions

To correctly solve the system of equations, BCs an ICs are required. In case of the BCs it can be seen for the top part of the MP ($n = 0$) the nodes u_0, w_{-1}, w_0 are non-existent. These nodes, shown in Figure A.1, are considered "ghosts nodes" and need to be eliminated for the equation at $n = 0$ as well as at $n = N$. This is also valid for ICs, which will be treated later.

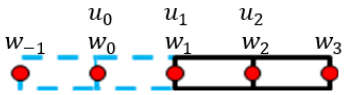

Figure A.1: Discretized BC at $n = 1$

A.2.1. Implementing BC

First the boundary conditions have to be defined such that the bottom part of the MP is fixed with the top being a free end under a load. The BCs can for a MP under axisymmetric axial load ($F(t)$) can be given by:

$$\left.\frac{\partial^3 w_1}{\partial z^3}\right|_{z=0} = \left.\frac{\partial^4 w_1}{\partial z^4}\right|_{z=0} = 0 \tag{A.9a}$$

$$\left.\frac{\partial u_1}{\partial z}\right|_{z=0} = \frac{F(t)}{EA} \tag{A.9b}$$

$$u_1|_{z=L} = w_1|_{z=L} = \left.\frac{\partial w_1}{\partial z}\right|_{z=L} = 0 \tag{A.9c}$$

These BCs can be written in discrete form using Equation A.2, in order to solve for the ghost nodes. The top BCs in discrete form are:

$$\begin{pmatrix}0 & -1 & 2\\ 0 & 1 & -4\\ -1 & 0 & 0\end{pmatrix}\begin{bmatrix}u_0\\ w_{-1}\\ w_0\end{bmatrix} + \begin{pmatrix}0 & 0 & 0 & -2 & 1 & 0\\ 0 & 0 & 6 & -4 & 1 & 0\\ 0 & 1 & 0 & 0 & 0 & -\frac{2\Delta z}{EA}\end{pmatrix}\begin{bmatrix}u_1\\ u_2\\ w_1\\ w_2\\ w_3\\ F(t)\end{bmatrix} = 0 \tag{A.10}$$

Solving the system of equations for the ghost nodes give:

$$\begin{bmatrix}u_0\\ w_{-1}\\ w_0\end{bmatrix} = \begin{pmatrix}0 & 1 & 0 & 0 & 0 & -\frac{2\Delta z}{EA}\\ 0 & 0 & 6 & -8 & 3 & 0\\ 0 & 0 & 3 & -3 & 1 & 0\end{pmatrix}\begin{bmatrix}u_1\\ u_2\\ w_1\\ w_2\\ w_3\\ F(t)\end{bmatrix} \tag{A.11}$$

Substituting these ghosts nodes back into Equation A.3 changes the entries of the K matrices for node $n = 1$:

$$\frac{\partial^2 u_1}{\partial t^2} + \frac{c_p^2}{\Delta z^2}\left(2u_1 - 2u_2\right) + \frac{c_p^2 \nu}{2\Delta z R}\left(3w_1 - 4w_2 + w_3\right) = -\frac{2c_p^2}{EA\Delta z}F(t) \tag{A.12a}$$

$$\frac{\partial^2 w_1}{\partial t^2} + \frac{c_p^2}{R^2} w_1 = -\frac{\nu c_p^2}{EAR} F(t) \tag{A.12b}$$

In the case of $n = 2$, one ghost node (w_0) will be encountered and should also be eliminated, resulting in the following equation for that node:

$$\frac{\partial^2 w_2}{\partial t^2} + \frac{c_p^2}{\Delta z^2} w_n^+ + \frac{c_p^2 \nu}{2\Delta z R} \left(-u_1 + u_3\right) + \frac{c_p^2\, h_{MP}^2}{12\Delta z^4} \left(w_0 - 4w_1 + 6w_2 - 4w_3 + w_4\right) = 0 \tag{A.13}$$

The same method can be applied for the bottom BCs. However, the EOM for $n = L$ is fully described by the BC $w_L = 0$. In that specific case all terms in the EOM are 0 except for the entry of w_L in the K-matrix, which should be 1. However, similarly to the 2nd node of the MP, the second to last node $N = L - 1$, thus the other BC should only be applied to the EOM for $N = L - 1$:

$$\frac{\partial^2 w_{L-1}}{\partial t^2} + \frac{c_p^2}{\Delta z^2} w_n^+ + \frac{c_p^2 \nu}{2\Delta z R} \left(-u_{n-1}^+ + u_{n+1}^+\right) + \frac{c_p^2\, h_{MP}^2}{12\Delta z^4} \left(w_{L-3} - 4w_{L-2} + 7w_{L-1} - 4w_L\right) = 0 \tag{A.14}$$

A.2.2. Implementing IC

The ICs are implemented in a similar manner than that of BCs. The difference with a BC is that the IC could be seen as two separate ends where the left (−) and right (+) side should have the properties of being a continuity at the specified node $n = R$, see the figure below.

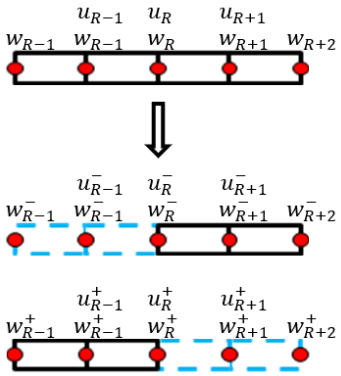

Figure A.2: Discretized IC at $n = R$

In chapter 3 it has been discussed that the rollers do not exert axial forces on the MP. This would result in the assumption that no force balance is required when setting up the ICs for the roller interface. In the following equations, it is assumed that this term is non-zero to allow us to visualize the influence on the computations for the EOMs. The given ICs are as follows:

$$[0] \quad w_R^+ = w_R^- \tag{A.15a}$$

$$[1] \quad \frac{\partial w_R^+}{\partial z} = \frac{\partial w_R^-}{\partial z} \tag{A.15b}$$

$$[2] \quad \frac{\partial^2 w_R^+}{\partial z^2} = \frac{\partial^2 w_R^-}{\partial z^2} \tag{A.15c}$$

$$[3]\; EI \left(\frac{\partial^3 w_R^+}{\partial z^3} - \frac{\partial^3 w_R^-}{\partial z^3} \right) = k_R (w_{1,RB} - w_R^+) + c_R \left(\frac{\partial w_{1,RB}}{\partial t} - \frac{\partial w_R^+}{\partial t} \right) \tag{A.15d}$$

$$[4] \; \frac{\partial u_R^+}{\partial z} = \frac{\partial u_R^-}{\partial z} \tag{A.15e}$$

Note that the first IC is denoted as the 0^{th} since this IC does not contain any ghosts nodes. It is evident that there are six unknown variables present in the system, while only four equations are provided. Consequently, this system of equations appears to be unsolvable based on the given information. However, by incorporating the requirement of continuity at w_R and the fact that the subtracting the negative side from of the positive side of the EOM should equal zero, it is possible to introduce two additional equations to ensure a solvable system. This extension of equations is applicable to both the axial and radial directions. This gives the following two extra ICs:

$$[5] \quad \frac{c_p^2}{\Delta z^2} \left(-u_{R-1}^+ - u_{R+1}^+\right) + \frac{c_p^2 \nu}{2\Delta z R} \left(w_{R-1}^+ - w_{R+1}^+\right) = \frac{c_p^2}{\Delta z^2} \left(-u_{R-1}^- - u_{R+1}^-\right) + \frac{c_p^2 \nu}{2\Delta z R} \left(w_{R-1}^- - w_{R+1}^-\right) \tag{A.16a}$$

$$\begin{aligned} [6] \quad & \frac{\nu c_p^2}{2\Delta z R} \left(-u_{R-1}^+ + u_{R+1}^+\right) + \frac{c_p^2\, h_{MP}^2}{12\Delta z^4} \left(w_{R-2}^+ - 4w_{R-1}^+ - 4w_{R+1}^+ + w_{R+2}^+\right) = \\ & \frac{\nu c_p^2}{2\Delta z R} \left(-u_{R-1}^- + u_{R+1}^-\right) + \frac{c_p^2\, h_{MP}^2}{12\Delta z^4} \left(w_{R-2}^- - 4w_{R-1}^- - 4w_{R+1}^- + w_{R+2}^-\right) \end{aligned} \tag{A.16b}$$

Note that due to IC[0] the w_R^+ and w_R^- cancel each other out. Applying the same methodology used for the BCs, the ghost nodes can be solved:

$$\begin{bmatrix} u_{n+1}^- \\ u_{n-1}^+ \\ w_{n+2}^- \\ w_{n+1}^- \\ w_{n-1}^+ \\ w_{n-2}^+ \end{bmatrix} = \begin{pmatrix} 1 & 0 & 0 & 0 & 0 & 0 & 0 & 0 \\ 0 & 1 & 0 & 0 & 0 & 0 & 0 & 0 \\ 0 & 0 & 1 & 0 & \frac{D}{2} & 0 & 0 & \frac{-D\sin(\alpha)}{2} \\ 0 & 0 & 0 & 1 & 0 & 0 & 0 & 0 \\ 0 & 0 & 0 & 0 & 0 & 1 & 0 & 0 \\ 0 & 0 & 0 & 0 & \frac{D}{2} & 0 & 1 & \frac{-D\sin(\alpha)}{2} \end{pmatrix} \begin{bmatrix} u_{n+1}^+ \\ u_{n-1}^- \\ w_{n+2}^+ \\ w_{n+1}^+ \\ w_n^- \\ w_{n-1}^- \\ w_{n-2}^- \\ w_{1,RB} \end{bmatrix} \tag{A.17}$$

where $B = \frac{c_p^2 \nu}{2\Delta z R}$, $C = \frac{c_p^2 \, h_{MP}^2}{12\Delta z^4}$ and $D = \frac{2\Delta z^3 k_R}{EI}$.
The EOM for both the axial and radial at $n = R$ now become:

$$\frac{\partial^2 u}{\partial t^2} + \frac{c_p^2}{\Delta z^2}\left(-u_{n-1}^- + 2u_n^+ - u_{n+1}^+\right) = 0 \tag{A.18a}$$

$$\frac{\partial^2 w_n^+}{\partial t^2} + Aw_n^+ + B\left(-u_{n-1}^- + u_{n+1}^+\right) + C\left(w_{n-2}^- - 4w_{n-1}^- + \left(6 + \frac{D}{2}\right)w_n^+ - 4w_{n+1}^+ + w_{n+2}^+\right) = \frac{CD\sin(\alpha)}{2} w_{1,RB} \tag{A.18b}$$

It is worth noting that the additional conditions introduced, such as spring stiffness or damping, in both the radial and axial directions exclusively affect their respective directions.

A.3. Discretized beam model

In this paragraph the RB is modelled as a beam. In the base case the beam is excited by the radial expansion of the MP which is retrieved from the MP model. This output has the condition where in the MP model there is no influence of a spring ($k_R = 0$). In reality, both the MP and beam should influence one another. This will be treated in the coupled model.

In this section the BCs of the beam will be considered. First the free end, the MP end of the beam, is implemented, followed up by the gripper ring side of the beam. This side will be modelled in two ways: (1) as a clamped beam and (2) as a hinged beam. In the final step, the hydraulic cylinder will be added. The EoM used for this beam is based on the Euler-Lagrange beam equation, which reads:

$$\rho A \frac{\partial^2 w}{\partial t^2} + EI \frac{\partial^4 w}{\partial x^4} = 0 \tag{A.19}$$

Which in discretized form reads:

$$\frac{\partial^2 w_n}{\partial t^2} + \frac{\beta}{\Delta x^4}\left(w_{n-2} - 4w_{n-1} + 6w_n - 4w_{n+1} + w_{n+2}\right) = 0, \qquad \beta = \frac{EI}{\rho A} \tag{A.20}$$

A.3.1. MP end of beam

At the MP end of the beam it is assumed that the beam has 'free end' beam conditions. This results in the following BCs:

$$EI \left.\frac{\partial^3 w}{\partial x^3}\right|_{x=0} = -k_R\left(w_1 - y_{MP}\right) \tag{A.21a}$$

$$\left.\frac{\partial^2 w}{\partial x^2}\right|_{x=0} = 0 \tag{A.21b}$$

For $n = 0$, the nodes w_{-1} and w_0 are ghosts nodes and need to be eliminated from the EoM in order to have a solvable system. In matrix form these BCs can be written as:

$$\begin{pmatrix} -1 & 2 \\ 0 & 1 \end{pmatrix}\begin{bmatrix} w_{-1} \\ w_0 \end{bmatrix} + \begin{pmatrix} \frac{2\Delta x^3 k_R}{EI} & -2 & 1 & -\frac{2\Delta x^3 k_R}{EI} \\ -2 & 1 & 0 & 0 \end{pmatrix}\begin{bmatrix} w_1 \\ w_2 \\ w_3 \\ y_{MP} \end{bmatrix} = 0 \tag{A.22}$$

Ultimately, the ghost nodes can be substituted in the EoM for the first node, which results in the following:

$$\frac{\partial^2 w_1}{\partial t^2} + \frac{\beta}{\Delta x^4}\left(\left(2 + \frac{2\Delta x^3 k_R}{EI}\right) w_1 - 4w_2 + 2w_3\right) = \frac{2k_R}{\rho A \Delta x} y_{MP} \tag{A.23}$$

A.3.2. Clamped vs. hinged beam end

In this section a comparison will be made regarding the clamped and hinged condition of the beam.

Clamped end

When dealing with a clamped end, the following BCs hold:

$$w_L = 0 \tag{A.24a}$$

$$\left.\frac{\partial w}{\partial x}\right|_{x=L} = 0 \tag{A.24b}$$

There is no longer an EoM for the node at $n = L$, as this is now fully prescribed by the first BC resulting in the EoM for the solver in the form:

$$\frac{\partial^2 w_L}{\partial t^2} + w_L = 0 \tag{A.25}$$

Now, there is only 1 ghost node left, which is valid at $n = L - 1$. Substituting the BC results in:

$$\frac{\partial^2 w_{L-1}}{\partial t^2} + \frac{\beta}{\Delta z^4}\left(w_{L-3} - 4w_{L-2} + 7w_{L-1} - 4w_L\right) = 0 \tag{A.26}$$

Hinged end

When dealing with a hinged end, a similar method is used where the first BC fully describes the EoM of the last node. However, the second BCs is now of 2^{nd} order, which reads:

$$\frac{\partial^2 w_L}{\partial x^2} = 0 \tag{A.27}$$

With the EoM now becoming:

$$\frac{\partial^2 w_{L-1}}{\partial t^2} + \frac{\beta}{\Delta z^4}\left(w_{L-3} - 4w_{L-2} + 5w_{L-1} - 2w_L\right) = 0 \tag{A.28}$$

A.4. Hydraulic cylinder

When dealing with the hydraulic cylinder, the same method applies where the ICs are to be met as represented in subsection A.2.2. IC [3] as presented in Equation A.15d now becomes:

$$EI\left(\frac{\partial^3 w^+}{\partial x^3} - \frac{\partial^3 w^-}{\partial x^3}\right) = -k_{c,y} w_n^+ - c_{c,y}\frac{\partial w_n^+}{\partial t} \tag{A.29}$$

Resulting in the final missing EoM to fully describe the beam:

$$\frac{\partial^2 w_c^+}{\partial t^2} + \frac{\beta}{\Delta x^4}\left(w_{c-2}^- - 4w_{c-1}^- + \left(6 + \frac{2\Delta x^3 k_{c,y}}{2EI}\right) w_c^+ - 4w_{c+1}^+ + w_{c+2}^+\right) = 0 \tag{A.30}$$

B

Finite element method models

Throughout this research, several models were constructed to describe the vibrations of the RB under the impact of a MP load from an impact hammer. This appendix provides details on the FEM simulations of these models and how they are set up in Abaqus. Similar to the main portion of this thesis, this appendix is divided into three parts, each focusing on individual models. The base case considered in this appendix involves the use of a 12.5 m diameter MP for the calculations. The properties of the MP and RB are detailed in Table 3.1 & 3.2. The material properties used for all models are: $\nu = 0.3$, $E = 210$ GPa and $\rho = 7850$ kg/m^3. In Abaqus, two types of numerical solvers can be distinguished: implicit and explicit. The advantages of these solvers are discussed in chapter 2. Implicit solvers are known to be based on the Backward Euler method, while explicit solvers are based on the Forward Euler method.

B.1. Monopile model

The MP is modeled using the Donnell-Mushtari shell theory, which allows the inclusion of the spring to be added in this model, as no other terms would adequately represent the shear forces in the radial direction. In FEM, this effect is also considered, though it is unknown which theory serves as the baseline. Four main different methods are employed for solving the MP model:

Shell model
Here, the shell model represents an axisymmetric thin-walled structure, with properties set to ensure that stresses and displacements remain constant in the wall thickness direction. This assumption is also applied in the FDM numerical model, given the relatively high radius-to-thickness ratio. The shell model is solved both explicitly and implicitly to observe differences in accuracy and computational time.

Membrane model
The membrane model is designed to exclude the local bending term in the radial direction, as membranes lack the structural resistance to counteract these shear forces. In the FEM simulation, the element type is set to SAX1, employing a 2-node linear shell where the output is linearly calculated between these two nodes. The alternative option, SAX2, would involve a quadratic approach, computing the average of three nodes in the through-thickness direction.

Solid model
The main distinction from the aforementioned models lies in the flexibility to define the number of nodes in the through-thickness direction. In this case, the mesh size in through-thickness has been set to 0.033 m, which results in a 4-node mesh size in the model.

B.1.1. General settings MP

In general, the same boundary conditions (BCs) apply to all models, where the bottom of the MP is clamped. However, when dealing with the $1/8^{\text{th}}$ model, a new 'datum axis' must be defined to incorporate the BCs in polar coordinates. These coordinates do not need to be defined for the other models, as they are already incorporated in the axisymmetric conditions of the model.

B.2. Mesh convergence

Choosing a mesh size is a critical thing to do when trying to get accurate results for a within a short amount of time as possible. For the mesh convergence test, only one model is considered and will be used as base case for the other MP models. It is expected that the difference in displacements with different mesh sizes is negligible for different solvers. It has been determined that a mesh size of 1 meter is sufficiently accurate to model the MP.

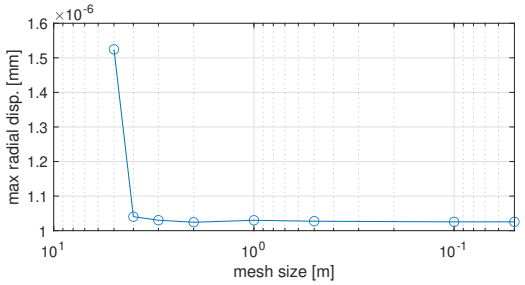

Figure B.1: Mesh convergence of FEM MP shell explicit model of length $L_{MP} = 110$ m

B.3. Rollerbox model

The RB is modeled as a simple beam with constant cross-sectional properties. Similar to the MP, a mesh convergence test is conducted, as depicted in the figure below. Through this analysis, it has been determined that a mesh size of 0.6 m is considered accurate, resulting in the beam being divided into 10 elements. It is important to realize that the RB in Abaqus is calculated in all directions, whereas the FDM model assumes that only bending occur, which decouples the non-linear beam equation to a simple 1D beam equation.

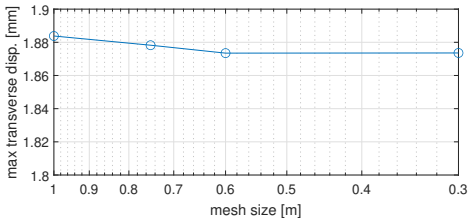

Figure B.2: Mesh convergence of FEM RB model

B.4. Coupled model

A fully axisymmetric model in Abaqus cannot be modelled due to the limitations of Abaqus. When combining the MP model with the RB in a axisymmetric manner, the RB would be modelled as a cone, which is not representative for the real life scenario. Therefore, two models were proposed in order to simulate the total system:

- ➢ Single RB;
- ➢ artificial axisymmetric RBs.

In both these models, the $1/8^{\text{th}}$ MP model is employed. When considering the single RB, the middle node of the MP in circumferential direction is connected to the RB. Consequently, the adjacent nodes in the θ-plane are not restricted by the movement and can freely move. The second model is modelled such that every node in the θ-plane is connected to a RB. This would simulate the effect of the RB being of axisymmetric properties. It is important to note that for the nodes at the edge of the pile, the RB and roller properties are halved. This has to be done in order to account for the symmetry, where the adjacent next 1/8th pile has the same properties. Otherwise, the stiffness would be double at this point. In both of these models, the $1/8^{\text{th}}$ MP model is utilized. In the case of the single RB, the middle node of the MP in the circumferential direction is connected to the RB. As a result, the adjacent nodes in the θ-plane are not restricted by the movement and can move freely. The second model is designed such that every node in the θ-plane is connected to a RB. This setup simulates the effect of the RB having axisymmetric properties. It is essential to note that for the nodes at the edge of the pile, the RB and roller properties are halved. This adjustment is made to account for symmetry, where the adjacent $1/8^{\text{th}}$ pile has the same properties. Without this adjustment, the stiffness would be doubled at this point.